

2014-09-30

# Developing a semi/automated protocol to post-process large volume, High-resolution airborne thermal infrared (TIR) imagery for urban waste heat mapping

Rahman, Mir Mustafizur

---

Rahman, M. M. (2014). Developing a semi/automated protocol to post-process large volume, High-resolution airborne thermal infrared (TIR) imagery for urban waste heat mapping (Doctoral thesis, University of Calgary, Calgary, Canada). Retrieved from <https://prism.ucalgary.ca>. doi:10.11575/PRISM/25617  
<http://hdl.handle.net/11023/1865>

*Downloaded from PRISM Repository, University of Calgary*

UNIVERSITY OF CALGARY

Developing a semi/automated protocol to post-process large volume,  
High-resolution airborne thermal infrared (TIR) imagery for urban waste heat mapping

by

Mir Mustafizur Rahman

A THESIS

SUBMITTED TO THE FACULTY OF GRADUATE STUDIES  
IN PARTIAL FULFILMENT OF THE REQUIREMENTS FOR THE  
DEGREE OF DOCTOR OF PHILOSOPHY

GRADUATE PROGRAM IN GEOGRAPHY

CALGARY, ALBERTA

SEPTEMBER, 2014

© Mir Mustafizur Rahman 2014

## Abstract

In collaboration with The City of Calgary 2011 Sustainability Direction and as part of the HEAT (Heat Energy Assessment Technologies) project, the focus of this research is to develop a semi/automated 'protocol' to post-process large volumes of high-resolution (H-res) airborne thermal infrared (TIR) imagery to enable accurate urban waste heat mapping. HEAT is a free GeoWeb service, designed to help Calgary residents improve their home energy efficiency by visualizing the amount and location of waste heat leaving their homes and communities, as easily as clicking on their house in Google Maps. HEAT metrics are derived from 43 flight lines of TABI-1800 (Thermal Airborne Broadband Imager) data acquired on May 13-14, 2012 at night (11:00 pm - 5:00 am) over The City of Calgary, Alberta (~825 km<sup>2</sup>) at a 50 cm spatial resolution and 0.05°C thermal resolution. At present, the only way to generate a large area, high-spatial resolution TIR scene is to acquire separate airborne flight lines and mosaic them together. However, the ambient sensed temperature within, and between flight lines naturally changes during acquisition (due to varying atmospheric and local micro-climate conditions), resulting in mosaicked images with different temperatures for the same scene components (e.g. roads, buildings), and mosaic join-lines arbitrarily bisect many thousands of homes. In combination these effects result in reduced utility and classification accuracy including, poorly defined HEAT Metrics, inaccurate hotspot detection and raw imagery that are difficult to interpret.

In an effort to minimize these effects, three new semi/automated post-processing algorithms (the protocol) are described, which are then used to generate a 43 flight line mosaic of TABI-1800 data from which accurate Calgary waste heat maps and HEAT metrics can be generated. These algorithms (presented as four peer-reviewed papers) - are: (a) Thermal Urban Road Normalization (TURN) - used to mitigate the microclimatic variability within a thermal

flight line based on varying road temperatures; (b) Automated Polynomial Relative Radiometric Normalization (RRN) - which mitigates the between flight line radiometric variability; and (c) Object Based Mosaicking (OBM) - which minimizes the geometric distortion along the mosaic edge between each flight line. A modified Emissivity Modulation technique is also described to correct H-res TIR images for emissivity. This combined radiometric and geometric post-processing protocol (i) increases the visual agreement between TABI-1800 flight lines, (ii) improves radiometric agreement within/between flight lines, (iii) produces a visually seamless mosaic, (iv) improves hot-spot detection and landcover classification accuracy, and (v) provides accurate data for thermal-based HEAT energy models.

**Keywords:** Thermal Infrared, Post-Processing, High Spatial Resolution, Airborne, Thermal Urban Road Normalization (TURN), Relative Radiometric Normalization (RRN), Object Based Mosaicking (OBM), TABI-1800, HEAT, and Automation.

## Preface

This is a manuscript-based thesis. Chapters 3 and 4 are accepted, Chapter 5 is submitted, and Chapter 6 is published in peer-reviewed journals. I am intellectually responsible for all the works presented in this thesis.

Chapter 3: “*Transforming image-objects into multiscale fields: a GEOBIA approach to mitigate microclimatic variability within a H-res thermal infrared urban scene*” is co-authored by **Rahman, M. M.**, Hay, G. J., Couloigner, I., and Hemachandaran, B. and has recently been accepted to a Special Issue (ISSN 2072-4292) titled *Advances in Geographic Object-Based Image Analysis (GEOBIA)* of the open-source Journal ‘Remote Sensing’, – (Manuscript ID: remotesensing-60154) Journal Impact Factor<sup>1</sup>: 2.623 (2013); 5-Year Impact Factor: 2.729.

Chapter 4 is titled “*A comparison of four relative radiometric normalization (RRN) techniques for mosaicking H-res multi-temporal thermal infrared (TIR) flight lines of a complex urban scene*” (PHOTO-D-14-00266). It is co-authored by **Rahman, M. M.**, Hay, G. J., Couloigner, I., Hemachandaran, B., and Bailin, J. and has recently been accepted with corrections in ‘The ISPRS Journal of Photogrammetry and Remote Sensing’ - Journal Impact Factor<sup>2</sup>: 2.902 (2013); 5-Year Impact Factor: 4.202.

Chapter 5 is titled “*An assessment of polynomial regression techniques for the relative radiometric normalization (RRN) of high-resolution multi-temporal airborne thermal infrared (TIR) imagery*”. It is co-authored by **Rahman, M. M.**, Hay, G. J., Couloigner, I., Hemachandaran, B., and Bailin, J. and is submitted (Sept 09, 2014) to a Special Issue (ISSN 2072-4292) titled

---

<sup>1</sup> <http://www.mdpi.com/journal/remotesensing> - Last accessed Sept 02, 2014

<sup>2</sup> <http://www.journals.elsevier.com/isprs-journal-of-photogrammetry-and-remote-sensing/> - Last accessed Sept 02, 2014

“*Recent Advances in Thermal Infrared Remote Sensing*”<sup>3</sup> of the open-source journal ‘Remote Sensing’, – (Manuscript ID: remotesensing-65309) Journal Impact Factor<sup>4</sup>: 2.623 (2013); 5-Year Impact Factor: 2.729.

Chapter 6 is titled “*Geographic Object-Based Mosaicking (OBM) of High-Resolution Thermal Airborne Imagery (TABI-1800) to improve the Interpretation of Urban Image-Objects*”.

This work is co-authored by **Rahman, M.M.**, Hay, G.J., Couloigner, I., Hemachandran, B., Bailin, J., Zhang Y., and Tam, A. and was published (2013) in *Geoscience and Remote Sensing Letters*, IEEE, 10:4, 918-922 - Journal Impact factor<sup>5</sup>: 1.809 (2013); 5-year impact 1.98.

---

<sup>3</sup> [http://www.mdpi.com/journal/remotesensing/special\\_issues/thermal-infrared](http://www.mdpi.com/journal/remotesensing/special_issues/thermal-infrared) - Last accessed Sept 02, 2014.

<sup>4</sup> <http://www.mdpi.com/journal/remotesensing> - Last accessed Sept 02, 2014

<sup>5</sup> <http://ieeexplore.ieee.org/xpl/RecentIssue.jsp?punumber=8859> – Last accessed Sept 02, 2014

## **Acknowledgements**

I would like to express my sincere gratitude to my supervisor Dr. Geoffrey J. Hay for his significant contribution to my academic career. I also would like to acknowledge his generous financial support, continuous guidance, advice and constructive criticism throughout the period of my PhD program - without his support it wouldn't have been possible for me to finish my thesis.

I would like to thank my committee members Dr. John Yackel, and Dr. Mryka Hall-Beyer for their valuable inputs and support. I also would like to thank Dr. Tak Fung for his guidance in the statistical aspects of my thesis.

I am in debt to several members of the HEAT team who were always friendly, helpful, and cooperative, particularly Bharanidharan Hemachandran, Bilal Karim, Dr. Isabelle Couloigner, Gang Chen, Christopher D. Kyle, Rustam Kamberov and Fai Wu.

I would like acknowledge the Department of Geography for providing me funding to pursue my degree. I also would like to express my gratitude to ITRES research limited and The City of Calgary for providing datasets for my research.

I wish to express my sincere thanks to all my friends inside and outside Calgary whose advice and moral support contributed to the completion of my thesis. Lastly, I would like to mention my family, for whom words alone cannot express my gratitude.

## Table of Contents

Abstract.....	ii
Preface.....	iv
Acknowledgements.....	vi
Table of Contents.....	vii
List of Tables.....	x
List of Figures and Illustrations.....	xi
CHAPTER ONE: INTRODUCTION.....	1
1.1 What is energy efficiency and waste heat?.....	2
1.2 Contemporary methods of measuring a building’s energy efficiency.....	2
1.3 Thermal infrared remote sensing for measuring buildings’ energy.....	4
1.4 Thesis objective and overview.....	6
CHAPTER TWO: LITERATURE REVIEW.....	13
2.1 Thermography basics.....	13
2.1.1 Blackbody radiation.....	13
2.1.2 Kinetic energy and kinetic temperature.....	14
2.1.3 Emissivity.....	15
2.2 Thermal sensors and their applications.....	16
2.2.1 Satellite based thermal sensors– a brief history.....	16
2.2.2 Airborne thermal infrared sensors.....	21
2.2.3 Hand-held thermal infrared sensors.....	23
2.2.4 Thermal urban remote sensing applications.....	23
2.3 Challenges in thermal remote sensing.....	24
2.3.1 Complexity of urban surface and varied sun-surface-sensor geometry.....	25
2.3.2 Atmospheric and microclimatic influence on thermal response.....	26
2.3.2.1 Correction for atmospheric interactions.....	26
2.3.2.2 Problems of urban atmosphere: <i>microclimate</i> .....	28
2.3.3 Difference between radiant temperature and true kinetic temperature.....	30
2.4 An introduction to the study area.....	33
2.4.1 Microclimatic condition at the time of data collection.....	34
CHAPTER THREE: TRANSFORMING IMAGE-OBJECTS INTO MULTISCALE FIELDS: A GEOBIA APPROACH TO MITIGATE URBAN MICROCLIMATIC VARIABILITY WITHIN H-RES THERMAL INFRARED AIRBORNE FLIGHT LINES.....	50
3.1 Abstract.....	50
3.2 Introduction.....	51
3.3 Study area and dataset.....	54
3.4 Methods.....	56
3.4.1 Pseudo invariant features and mode road temperature.....	56
3.4.2 Road extraction.....	58
3.4.3 Multi interval sampling.....	61
3.4.4 Sampling optimization: borders and oversampling.....	62
3.4.5 Spatial interpolation of road temperature variations.....	63

3.4.6 Validation of the model .....	65
3.5 Results and discussions.....	66
3.5.1 Sample size vs. processing time .....	66
3.5.2 A comparison of radiometric normalization accuracy based on RMSE .....	68
3.5.3 Root mean square error (RMSE) vs. processing time .....	69
3.5.4 Visual assessment of the interpolated surface at different sampling intervals	70
3.5.5 Operational considerations, errors and uncertainties.....	74
3.5.5.1 Mitigating microclimate and surface effects .....	74
3.5.5.2 Road invariance .....	74
3.5.5.3 Emissivity correction .....	75
3.5.6 Transforming existing vector image-objects into multiscale fields .....	75
3.6 Conclusions.....	76

**CHAPTER FOUR: A COMPARISON OF FOUR RELATIVE RADIOMETRIC NORMALIZATION (RRN) TECHNIQUES FOR MOSAICKING H-RES MULTITEMPORAL THERMAL INFRARED (TIR) IMAGERY OF A COMPLEX URBAN SCENE.....**

4.1 Abstract.....	86
4.2 Introduction: radiometric normalization .....	87
4.3 Methods .....	91
4.3.1 Study area and dataset .....	92
4.3.2 Relative radiometric normalization (RRN) algorithms .....	93
4.3.2.1 Histogram matching.....	94
4.3.2.2 Pseudo invariant feature based radiometric normalization.....	95
4.3.2.3 No-change stratified random sample (NCSRS) based linear regression	98
4.3.3 Accuracy assessment .....	101
4.4 Results and discussions.....	102
4.4.1 Visual interpretation .....	102
4.4.2 Statistical analysis .....	108
4.4.3 Computation time .....	111
4.4.4 Ranking the evaluated methods.....	112
4.5 Conclusions.....	113

**CHAPTER FIVE: AN ASSESSMENT OF POLYNOMIAL REGRESSION TECHNIQUES FOR RELATIVE RADIOMETRIC NORMALIZATION (RRN) OF HIGH-RESOLUTION MULTITEMPORAL THERMAL INFRARED (TIR) IMAGERY**

5.1 Abstract.....	123
5.2 Introduction.....	124
5.3 Methods .....	127
5.3.1 Study area and dataset .....	127
5.3.2 Relative radiometric normalization .....	129
5.3.2.1 Histogram matching.....	129
5.3.2.2 Pseudo invariant feature (PIF) based polynomial regression .....	131
5.3.2.3 No-change stratified random sample (NCSRS) based regressions.....	132
5.3.2.4 Validation of the results using root mean square error (RMSE) .....	134
5.4 Results and discussions.....	135
5.4.1 Visual assessment.....	135

5.4.2 Statistical analysis .....	139
5.4.2.1 A comparison of automatic vs. manual methods .....	142
5.4.2.2 A comparison of linear vs. polynomial methods .....	142
5.4.2.3 An assessment of computation time .....	144
5.5 Conclusions.....	145
CHAPTER SIX: GEOGRAPHIC OBJECT BASED MOSAICKING (OBM) OF HIGH- RESOLUTION THERMAL AIRBORNE IMAGERY (TAB1-1800) TO IMPROVE THE INTERPRETATION OF URBAN IMAGE OBJECTS.....	152
6.1 Abstract.....	152
6.2 Introduction.....	152
6.3 Study area and dataset.....	154
6.4 Methods .....	155
6.5 Results and discussions.....	157
6.5.1 Reduced computation time .....	157
6.5.2 Improved visual interpretation .....	158
6.5.3 Reduced geometric distortion.....	158
6.5.4 Radiometric variations.....	160
6.6 Conclusions.....	162
CHAPTER SEVEN: A POST-PROCESSING PROTOCOL FOR HIGH-RESOLUTION AIRBORNE THERMAL INFRARED IMAGERY.....	166
7.1 Overview.....	166
7.2 The protocol.....	166
7.3 Operational considerations, errors and limitations .....	170
CHAPTER EIGHT: CONCLUSIONS AND FUTURE WORK.....	175
8.1 Conclusions.....	175
8.2 Future research.....	177

## List of Tables

Table 1-1: Typical NRCan EnerGuide Energy Efficiency Ratings .....	3
Table 2-1: Different types of roof material used in Calgary and their associated emissivity (@ 3.7-4.8 $\mu\text{m}$ ).....	15
Table 2-2: Summary features of thermal infrared sensors carried by satellite platforms .....	19
Table 2-3: Summary features of thermal infrared sensors carried by satellite platforms (continued) .....	20
Table 2-4: Summary features of thermal sensors carried by airborne platforms.....	22
Table 3-1: Training and test sample sizes of the evaluated flight lines for different sampling intervals.....	66
Table 4-1: Overall ranking of four RRN methods based on four different criteria (i-iv).....	113
Table 5-1: The overall RMSE of four different landcover types, for each of the four different relative radiometric normalization methods evaluated in this study. Bold values represent the lowest RMSE for each class and overall. ....	140
Table 5-2: Computation Time of four different RRN methods evaluated in this study. ....	145
Table 6-1: Feature extraction results based on traditional mosaicking vs. OBM (for 85 sample buildings). ....	159
Table 6-2: Thermal Statistics– Traditional Mosaicking VS. OBM (Results from the same 85 sample buildings at Table 6-1).....	162
Table 7-1: Emissivity value of different types of landcovers. ....	169

## List of Figures and Illustrations

Figure 2-1: Urban wind flow pattern from top and side .....	29
Figure 2-2: Map of annual mean total PM10 for Leicester. The spectrum ranges from blue (low concentration of PM10) to green, yellow, orange and red (High concentration of PM10) (Pierse et al., 2006). .....	30
Figure 2-3: An example of the Effect of Emissivity on Radiant Temperature. Each house has the same internal true temperature (22°C). However, the roof of each house is composed of materials with different emissivity. Consequently the sensor views a different radiant temperature for each roof.....	31
Figure 3-1: Map of The City of Calgary showing the location of the flight lines evaluated in this study. ....	55
Figure 3-2: This methodology flow chart describes the main steps for normalizing a thermal flight line using the TURN method. The italic numbers in parenthesis indicate the sections where details are provided. ....	57
Figure 3-3: An example of the road extraction technique. (A) The vector road layer (red). (B) The 1.5 m buffer created on both sides of the road center (road mask in white). (C) The TIR image showing dark tones as cool objects and bright tones as hot objects. Vegetation is delineated with black polygons (for illustration only) and the road center as a red line. (D) The dilated vegetation mask created from an NDVI image where black areas represent vegetation. (E) A ‘vegetation-free’ 3.0 m wide TIR road mask filled with thermal DNs. ....	59
Figure 3-4: (A) Histogram of flight line 1 showing a bimodal distribution, where the left distribution represents noise (i.e. road construction and vehicles) and the right distribution represents the road class. (B) A portion of the raw TIR image displaying roads, rooftops, trees, grass, parked vehicles and back alleys. Dark areas are cool, bright areas are warm. ....	60
Figure 3-5: An example of road training and test samples. (A) An example of a 3.0 m wide road mask. (B) An example of the test pixels derived from the road shown in 3-5A. (C) An example of the extracted training pixels (one sample per 10m*10m grid).....	62
Figure 3-6: An example of selecting sample points from the image border, then cleaning of these points to reduce oversampling. (A) A portion of the thermal flight line (grayscale) showing the acquisition border (black) and road center line (red). (B) A corresponding portion of the borderline detected using edge detection. (C) Sample points taken along the border at a 10 m interval. (D) Road samples (white) with the road center (red). (E) Border samples from (3-6C) combined with the road samples. The blue square (lower center) represents a sample location to be cleaned. (F) Final sample points after cleaning. ....	63

Figure 3-7: A comparison of CPU processing time for four different sampling intervals (10, 20, 50, and 100 m) for each of the three different flight lines. Time differences between flight lines are due to differences in data volumes/flight line. Time differences within flight lines are due to the size of the sample to be processed. ....	67
Figure 3-8: The percent (%) decrease in RMSE of three evaluated flight lines after radiometric normalization at four different sampling intervals (larger RMSE values are better). ....	69
Figure 3-9: A comparison of average radiometric accuracy vs. average processing time for 3 flight lines at four different sample intervals. ....	70
Figure 3-10: In this figure (A) shows a portion of the original TIR flight line displaying typical landcover (buildings, roads, grass). (B-E) illustrates four interpolated TURN surfaces that represent continuous urban microclimate temperature variability surfaces (°C), derived from local TIR road-objects, at four different sampling intervals: (B) 10 m, (C) 20 m, (D) 50 m, and (E) 100 m. Roads are in white, and isotherms are dark lines representing 0.5 °C intervals. ....	72
Figure 3-11: An example of radiometric normalization using TURN. (A) A portion of the raw TABI-1800 image. (B) A TURN-surface (i.e. an interpolated road temperature deviation surface) of the same area. (C) An image of the same area after applying the TURN-surface. ....	73
Figure 4-1: A map showing the approximate location of the flight lines used in this study. ....	93
Figure 4-2: A hypothetical example of the Histogram Matching technique ....	94
Figure 4-3: Histogram of three classes of Pseudo Invariant Features (grass, water, and road) selected for Relative Radiometric Normalization (RRN) showing both the intra-class variability and inter-class separability of the selected PIFs. ....	96
Figure 4-4: A scatterplot of Pseudo Invariant Features (PIFs) selected from three landcover classes (grass, water, and road) with a linear trend line showing the linear relationship between the master and the slave images. ....	97
Figure 4-5: A scatterplot of the PIFs modeled with the Theil-Sen trend line (solid black) and with a linear trendline (dotted black). ....	98
Figure 4-6: A histogram showing the absolute difference between the master and the raw slave image with associated basic statistics. The range shown by the blue square bracket (Mean $\pm$ 3SD) represents no change areas. ....	100
Figure 4-7: A scatterplot displaying NCSRS-Based Linear Regression trendline derived from 28,033 samples. ....	101

Figure 4-8: A comparison of four different radiometric normalizations of a river sample. (A) The raw image, (B) Histogram Matching, (C) PIF-Based Linear Regression, (D) PIF-Based TS Regression, (E) NCSRS-Based Linear Regression. .... 103

Figure 4-9: A comparison of four different radiometric normalizations of a road sample. (A) The raw image, (B) Histogram Matching, (C) PIF-Based Linear Regression, (D) PIF-Based TS Regression, (E) NCSRS-Based Linear Regression. .... 104

Figure 4-10: A comparison of four different radiometric normalizations of a grassy field sample. (A) The raw image, (B) Histogram Matching, (C) PIF-Based Linear Regression, (D) PIF-Based TS Regression, (E) NCSRS-Based Linear Regression..... 105

Figure 4-11: A comparison of different radiometric normalizations of a single rooftop. (A) The raw image, (B) Histogram Matching, (C) PIF-Based Linear Regression, (D) PIF-Based TS Regression, (E) NCSRS-Based linear regression. .... 106

Figure 4-12: Error maps of a sample location showing roads, rooftops and vegetation. (A) The sample area in the master image (dark areas are cold, bright areas are hot). (B) The corresponding area in the slave image. Error maps of (C) The raw slave image, (D) Histogram Matching (overall RMSE decreased by 52.4%), (E) PIF-Based Linear Regression (overall RMSE decrease by 39.1%), (F) PIF-Based TS Regression (overall RMSE increase by 24.5%), and (G) NCSRS-Based Linear Regression (overall RMSE decrease by 53.3%). .... 107

Figure 4-13: RMSE results of water test samples derived from four RRN methods. .... 108

Figure 4-14: RMSE results of road test samples derived from four RRN methods. .... 109

Figure 4-15: RMSE results of grass test samples derived from four RRN methods. .... 109

Figure 4-16: RMSE results of roof-top test samples derived from four RRN methods. .... 110

Figure 4-17: Comparison of overall mean RMSE for four different relative radiometric normalization techniques and the original raw TIR image, based on 2000 test samples - representing four different landcover classes..... 111

Figure 5-1: (A) A map of The City of Calgary, displaying the study area, and the location of the two TABI-1800 flight lines used in this study. (B) An example of TABI-1800 imagery within the study area, detailing the urban complexity resulting from roads, buildings, trees, green space, etc. Bright locations are warm, dark locations are cool..... 128

Figure 5-2: A hypothetical example of radiometric normalization using Histogram Matching technique. .... 130

Figure 5-3: Scatterplot of Pseudo Invariant Features (PIFs) selected within the overlap of the master and the slave images. These PIFS represent a combination of four landcover classes (grass, rooftop, water, and road), which are shown modeled with a 6<sup>th</sup> order polynomial trend line (black). .... 132

Figure 5-4: Scatterplot of No-Change Stratified Random Samples (NCSRS) with a 6th order polynomial trend line (black) and a linear trend line (red dotted) between the master and the slave images .....	134
Figure 5-5: Visual examples of four different relative radiometric normalization methods applied along the mosaic join line of four different landcover types (grass, road, water and rooftop).....	136
Figure 5-6: A visual example of how relative radiometric normalization decreases the radiometric variability between flight lines. (A) A sample area from the master image. (B) The same area from the slave image. Absolute image difference (C) between the master and the uncorrected slave image, and between the master and the normalized slave images resulting from (D) HM, (E) PIF_Poly, (F) NCSRS_Lin, and (G) NCSRS_Poly.....	139
Figure 5-7: (A) A comparison of the scatterplot between the original master and the slave images, and after applying four normalization methods: (B) HM, (C) PIF_Poly, (D) NCSRS_LIN, and (E) NCSRS_Poly. The blue lines describe the data trend line, while the red dashed lines show the expected trend(s) at perfect radiometric agreement.....	141
Figure 5-8: A comparison of linear (LIN) and polynomial (Poly) regression-based radiometric normalization using the same no-change stratified random samples (NCSRS). .....	143
Figure 6-1: Location map of the study area. ....	155
Figure 6-2: A graphic of three flight lines, with a 30% overlap are shown along with an example of the resulting object-based mosaic line (cyan) derived from a joining of the initial mosaic line (red dashed) and the buffered roof-top objects. ....	156
Figure 6-3: Figure (A) shows a sub-section of a TABI-1800 thermal mosaic, where the dashed line represents the mosaic boundary (dark tones are cold, bright tones are hot). The grey inset box represents the zoomed area illustrated in the adjacent figures. Figure (B) shows a house that is bifurcated as a result of joining flight lines using a traditional pixel-based mosaicking algorithm. Figure (C) shows the same building resulting from OBM. ....	158
Figure 6-4: A scale example of rooftop shape distortion resulting from a traditional mosaicking method vs. OBM. (A) Shows a rectangular GIS reference roof polygon. (B) Shows the same roof extracted from a traditional mosaic using ENVI FX. (C) Shows the same building extracted from an OBM mosaic using ENVI FX. The rectangle fit of figure A is 0.98, figure B is 0.77 and figure C is 0.89 (1.0 represents a perfect fit).....	160
Figure 6-5: An example of building change detection (image differencing) shown along the mosaic join. (A) shows a building (rectangular object) joined by OBM mosaicking, where the entire building is assessed from a single flight line and time, while (B) shows the same building joined with traditional mosaicking, thus half of the building is from one flight line and the other half is from an adjacent flight line. (C) Displays the change	

between the OBM and Traditional mosaicked building. The uniform light grey tone indicates no change, dark grey illustrates areas of moderate change, and black indicates high change. .... 161

Figure 6-6: This example illustrates how hot spot location (for the same house) can change, depending on which mosaicking technique is used. 6(A) shows an OBM joined house (from a single acquisition time) with the hottest spot centrally located. 6(B) shows a traditional mosaic that bisects the building and incorrectly identifies the hottest location based on temperature differences between the joined scenes (dashed line). .... 162

Figure 7-1: A flowchart displaying steps of post processing TIR imagery. .... 170

## **Chapter One: Introduction**

Seven billion people live on this planet and ~51% of them live in urban areas that occupy only ~1% of the world's arable land surface (PRB, 2009). With urban population growth rates (1.91%) higher than that of rural populations (0.22%) (United Nations, 2010), proper management of scarce urban resources is essential. While energy is necessary to ensure enhanced living standards, energy efficiency, i.e. doing the same with less energy, can further help to (i) save money, (ii) reduce pollution, and (iii) conserve limited energy resources. It is estimated that in Canada, the energy consumption of urban buildings accounts for ~30% of the total national energy production and ~35% of the total greenhouse gas (GHG) emissions, the majority of which is used for space and water heating (CUI, 2008). Thus, energy efficient space/water heating systems combined with efficient buildings that lower space heating requirements and reduce (wasted) heat leaving building envelopes, provide excellent opportunities for energy savings and pollution reduction at the local and national scale. However, to ensure efficient use of residential energy, it is necessary to understand: (i) whether a building is energy efficient or not, (ii) where the problems (zones) in a building are located that reduce energy efficiency, and (iii) how can the energy efficiency of residential buildings be compared at the house, neighbourhood and city levels, in order to promote meaningful energy efficiency feedback and engagement among citizens.

To more fully understand these questions, in this chapter, we briefly define energy efficiency and waste heat, and discuss contemporary methods and models used to measure residential waste heat. Then, we discuss a number of challenges associated with contemporary energy efficiency models/methods, and introduce the utility of thermal infrared (TIR) remote sensing in mitigating these problems with real world examples. This is followed by a brief

description of the complexity of TIR imagery, then a statement of the thesis objectives – to develop a ‘protocol’ to post-process thermal infrared (TIR) imagery for urban waste heat mapping.

### **1.1 What is energy efficiency and waste heat?**

In general terms, *energy efficiency* is understood as using less energy to perform the same amount of work. More specifically, a system can be called energy efficient when a minimum amount of energy is used to produce a work/service (Patterson, 1996). If the actual amount (to produce the work/service) is larger than the minimum amount, the user starts wasting energy. In our case, waste energy (waste heat) can be defined as the difference between the actual energy/cost required to provide a service and the minimum amount of energy/cost required to produce the same service. The term ‘energy efficiency’ is sometimes mixed up with ‘energy conservation’, which is not the same: energy conservation is defined as reducing, or going without a service to reduce the use of energy (Steg, 2008).

### **1.2 Contemporary methods of measuring a building’s energy efficiency**

Hand-held thermal infrared (TIR) sensors have commonly been used for decades to locate ‘faulty’ areas within a building envelope that are leaking heat/energy (Stockton and Lucas, 2011, Vidas and Moghadam, 2013). TIR sensors measure thermal infrared radiation, enabling the user to understand the (quantitative or qualitative) temperature pattern of the target. As a result, ‘faulty’ areas typically appear hotter than other portions of the building in TIR camera displays (Balaras and Argiriou, 2002). In Canada, there are a number of commercial service providers whom offer thermal inspection services for residential buildings. The cost for this service typically ranges from \$500-1500 per building, which is very expensive, especially when the user is typically not sure about the condition of their building. That is, they may have just paid for an energy efficient building to be assessed – which likely represents a very limited return on their investment. In

addition, individual building surveys using hand-held sensors do not provide a means to compare the condition of a building to its neighbors.

To provide a mechanism so that an individual building’s energy efficiency can be compared to others all over Canada, Natural Resources Canada (NRCan) developed the EnerGuide Rating System (ERS), a standard approach for measuring the energy efficiency of a building (Blais et al., 2005). This rating system allows for a comparison of a building’s energy efficiency to other buildings in neighborhoods and across Canada. The EnerGuide value of a typical residential dwelling is calculated by a model (HOT 2000), which considers building structural characteristics (e.g. construction material, building type, living area) and a household’s yearly energy consumption as inputs. This results in an EnerGuide rank (between 0 and 100) for the building, where 0 represents a home with major air leakage, no insulation and extremely high energy consumption, and 100 represents a perfectly insulated building with minimum energy consumption (NRCan, 2014).

**Table 1-1: Typical NRCan EnerGuide Energy Efficiency Ratings<sup>6</sup>**

Type of House	Rating
New house built to building code standards	65-72
New house with some energy-efficiency improvements	73-79
Energy-efficient new house	80-90
House requiring little or no purchased energy	91-100

The following standard operating conditions are assumed when calculating the EnerGuide rating:

- four occupants in each house,
- a thermostat setting of 21°C (70°F) on the main floors and 19°C (66°F) in the basement,

---

<sup>6</sup> Obtained from <http://www.nrcan.gc.ca/energy/efficiency/housing/new-homes/5075>

- a total domestic hot water consumption of 225 litres per day,
- lighting and appliance electricity consumption of 24 kilowatt hours per day,
- a minimum monthly average ventilation rate of 0.35 air change per hour during the heating season.

Although, this model provides a means to understand the energy efficiency of a building and to compare its condition to similar building across Canada, it has a number of limitations: (i) it can only be provided by a certified energy advisor (thus a typical homeowner cannot conduct it), (ii) it is not easy to understand, (iii) it does not identify where the waste heat problems are located and in what quantity, and (iv) it is reasonably expensive to obtain (Hemachandaran, 2013).

### **1.3 Thermal infrared remote sensing for measuring buildings' energy**

Thermal infrared (TIR) remote sensing<sup>7</sup> technologies offer useful information on landcover characteristics, including temperature and surface energy flux, which are commonly used for studying: (i) rural urban temperature variations (Kidder and Wu, 1987, Gallo and Owen 1998), (ii) the relationships between urban surface temperature and landuse (Lougeay et al., 1996; Weng, 2001; Weng et al., 2004), (iii) urban heat islands (Voogt and Oke, 1997, Weng et al., 2004, Rigo et al., 2006), and (iv) building heat loss/waste heat mapping (Allison, 2007, Hay et al., 2011).

Currently available satellite based TIR sensors provide moderate to low-resolution imagery (60 m - 1000 m), which are not sufficient for detailed mapping of urban buildings. Consequently, over the last three decades, a number of airborne TIR projects have been undertaken to measure residential heat-loss. For example, Brown et al. (1981) were pioneers in attempting to predict residential ceiling insulation levels using airborne TIR imagery. Although, their results were not

---

<sup>7</sup> See Section 2.1 for more detail on thermal infrared (TIR) remote sensing.

impressive (due to the technical limitations of the TIR data at that time), they explicitly noted the influence of surface color, emissivity, roof pitch, ventilation and surrounding temperatures on TIR based roof temperature measures. Seven years later, the National Swedish Institute for Building Research and the Swedish Space Corporation conducted an extensive study evaluating the operational advantages of airborne TIR imagery for heat loss mapping (Ljungberg and Rosengren, 1988). They claimed a 90% correlation between airborne TIR imagery and field measurements. However, their evaluation was based on only two sample buildings. In 2000 and 2007, Haringey Council (London, UK) developed classified residential heat-loss maps based on several TIR airborne acquisitions (Haringey Council, 2007); which (in theory) allowed for heat-loss comparisons between different buildings over time. Unfortunately, the 2007 heat loss survey suffered from serious calibration problems due in part to (i) the TIR data being captured on film then being scanned, digitized, geo-corrected and mosaicked; and (ii) the scene being acquired over multiple dates, with ambient temperatures changing within and between flights lines. This resulted in the City Council claiming a refund for their project costs, as the resulting heat maps were essentially unusable (Hay et al., 2011).

Similar heat-loss mapping studies were performed by (i) the City of Aberdeen, Scotland in 2000 and 2013, (ii) the City of Worcestershire, England in 2009, (iii) the City of Exeter, England in 2010, (iv) the City of Paris, France in 2010, and (v) Jersey City (New Jersey, USA) in 2011 (Hemachandran, 2013). While interesting, all these studies included important limitations: (i) their simple temperature class maps representing each building with a single color/class had limited capability for in depth visual, statistical and locational analysis, (ii) they did not remove the radiometric noise inherent to TIR data, and (iii) there is limited user interaction, or access to any of the data. More recently, the web-enabled Heat Energy Assessment Technologies (HEAT)

project (Hay et al., 2011) was developed for 368 homes using TABI-320 (Thermal Airborne Broadband Imager) data to help residents to (i) improve their home energy efficiency, (ii) save their money, and (iii) reduce their greenhouse gas (GHG) emissions by finding their hot-spots and visualizing the amount and location of waste heat leaving their homes and communities, as easily as clicking on their house in Google Maps. This project used high-spatial resolution (H-res 1.0 m) airborne TIR imagery to display detailed pseudo-coloured rooftop temperatures. Hay et al. (2011) also provided a HEAT Score for each home; which is a measure of how a particular building is wasting heat, allowing for comparison with its neighbours and other buildings in the community and city. Most importantly, they explicitly noted the geometric (mosaicking and co-registration) and radiometric (atmospheric, microclimatic and emissivity) issues that needed to be taken into account to accurately estimate residential roof temperatures from airborne TIR imagery over an entire city.

#### **1.4 Thesis objective and overview**

The previous sections briefly described the potential of TIR imagery for urban waste heat mapping along with its inherent geometric and radiometric limitations. Several studies have attempted to develop methods, or models to further mitigate these radiometric problems (Friedl and Davis, 1994; Voogt and Oak 2003; Weng, 2009), but they are neither complete, nor adequate (see section 2.3 for details). Considering these issues and the current state-of-the-art in airborne TIR residential waste heat mapping, the primary objective of this research is *to develop a comprehensive protocol to post process TIR airborne imagery for accurate urban waste heat mapping*. To achieve this, we describe three new normalization algorithms: (i) Thermal Urban Road Normalization (TURN) - used to standardize the variability within a TIR flight line, (ii) Automated Non-Linear Relative Radiometric Normalization (RRN) - used to mitigate the between

scene radiometric variability of a TIR flight line, and (iii) Object Based Mosaicking (OBM) – used to minimize the geometric distortion along the mosaic edge (between each flight line) - by mosaicking around rooftops rather than arbitrarily bisecting them. When systematically combined, these algorithms represent a complete method of post-processing H-res airborne TIR imagery. This protocol is evaluated over a (2012) TABI-1800 dataset composed of 43 TIR flight lines covering The City of Calgary (~825 km<sup>2</sup>) at a 50 cm spatial resolution and 0.05°C thermal resolution.

To achieve these objectives, Chapter 2 more fully describes (i) the theoretical basics of thermal remote sensing, (ii) the different thermal remote sensing platforms, sensors, and (iii) their applications, (iv) the complexity of H-res thermal imaging, (v) the existing methods and models to handle their complexity, and (vi) their applicability to the urban environment.

Chapter 3 is titled “*Transforming image-objects into multiscale fields: a GEOBIA approach to mitigate microclimatic variability within a H-res thermal infrared urban scene*”. This Chapter introduces and describes Thermal Urban Road Normalization (TURN), a new normalization algorithm, which mitigates the radiometric noise within a thermal flight line, primarily caused by microclimatic variability.

Chapter 4 is titled “*A comparison of four relative radiometric normalization (RRN) techniques for mosaicking H-res multi-temporal thermal infrared (TIR) flight lines of a complex urban scene*”. This paper evaluates four existing linear Relative Radiometric Normalization (RRN) techniques that are traditionally applied to optical satellite imagery, and examines their ability to normalize the radiometric variability between TIR flight lines.

Chapter 5 is titled “*An assessment of polynomial regression techniques for the relative radiometric normalization (RRN) of high-resolution multi-temporal airborne thermal infrared (TIR) imagery*”. This work tests the hypothesis that polynomial RRN techniques should

demonstrate increased radiometric agreement when compared to similar linear techniques. It does this by evaluating two new polynomial regression techniques, against the two best linear RRN techniques described in Chapter 4.

Chapter 6 is titled “*Geographic Object-Based Mosaicking (OBM) of High-resolution thermal airborne imagery (TABI-1800) to improve the interpretation of urban image-objects*”. This paper describes the new Object Based Mosaicking (OBM) algorithm, a novel automated method of mosaicking H-res airborne flight lines of TIR imagery that uses vector house objects to mosaic *around* 14,000+ houses, rather than arbitrarily bisecting those along the mosaic join line.

Chapter 7 is titled “A post-processing protocol for high-resolution airborne thermal infrared imagery”. It describes a process that brings the proposed algorithms (discussed in Chapters 3-6) together as a protocol for post-processing TIR airborne imagery.

Finally, Chapter 8 summarizes the models and methods developed and the lessons learned, along with a list of future work that can be pursued to improve the presented post processing protocol.

## References

- Allinson, David. 2007. Evaluation of aerial thermography to discriminate loft insulation in residential housing. PhD thesis, the University of Nottingham.
- Balaras, C.A., Argiriou, A.A. 2002. Infrared thermography for building diagnostics. *Energy and buildings*, 34:2, 171-183.
- Blais, S., Parekh, A., Roux, L. 2005. Energuides for houses database—an innovative approach to track residential energy evaluations and measure benefits. *Proceedings of Building Simulation*, Montreal, 71-78.
- Brown, R.J., Cihlar, J., Teillet, P.M. 1981. Quantitative residential heat loss study. *Photogrammetric Engineering and Remote Sensing*, 47:9, 1327-1333.
- CUI, 2008. Energy Mapping Study. Prepared by the Canadian Urban Institute. December 19, 2008. pp, 92.
- Friedl, M.A., Davis, F.W. 1994. Sources of Variation in radiometric surface temperature over a tallgrass prairie. *Remote Sensing of Environment*. 48, 1-17.
- Gallo, K.P., Owen, T.W. 1998. Assessment of urban heat island: A multi-sensor perspective for the Dallas-Ft. Worth, USA region. *Geocarto International*, 13:4, 35–41.
- Haringey Council, 2007. Home Heat Loss,  
[http://www.haringey.gov.uk/index/housing\\_and\\_planning/housing/housingadvice](http://www.haringey.gov.uk/index/housing_and_planning/housing/housingadvice). Last accessed: July 04, 2014.
- Hay G.J., Kyle C., Hemachandran B., Chen G., Rahman M.M., Fung T.S., Arvai J.L. 2011. Geospatial Technologies to Improve Urban Energy Efficiency. *Remote Sensing*. 3:7, 1380-1405.

- Hemachandran, B. 2013. Developing HEAT scores with H-res thermal imagery to support urban energy efficiency. MSc Thesis. Department of Geography, University of Calgary.
- Kidder, S.Q., Wu, H.T. 1987. A multispectral study of the St. Louis area under snow-covered conditions using NOAA-7 AVHRR data. *Remote Sensing of Environment*, 22, 159–172.
- Ljungberg, S.A., Rosengren, H. 1988. Aerial and Mobile Thermography to Assess Damages and Energy Losses from Buildings and District Heating Networks – Operational Advantages and Limitations. *ISPRS Archives*. XXVII: B7-VII, pp. 348.
- Lougeay, R., Brazel, A., Hubble, M. 1996. Monitoring intra-urban temperature patterns and associated landcover in Phoenix, Arizona using Landsat thermal data. *Geocarto International*, 11, 79– 89.
- NRCan. 2014. EnerGuide for Houses Database - Natural Resources Canada.  
<http://www.nrcan.gc.ca/energy/publications/efficiency/ee-products/lighting/6637>, last accessed July 04, 2014.
- Patterson, M.G. 1996. What is energy efficiency?: Concepts, indicators and methodological issues. *Energy policy*. 24:5, 377-390.
- PRB 2009. Population Reference Bureau. World Population Data Sheet. 1875 Connecticut Ave., NW, Washington, DC 20009 USA.
- Rigo, G., Parlow, E., Oesch, D. 2006. Validation of satellite observed thermal emission with in-situ measurements over an urban surface. *Remote Sensing of Environment*, 104, 201–210.
- Steg, L. 2008. Promoting household energy conservation. *Energy policy*. 36:12, 4449-4453.
- Stockton, G.R., Lucas, R.G. 2011. Using a combination of aerial infrared and handheld infrared cameras for measuring, analyzing, and prioritizing the thermal performance of big box

- buildings. SPIE Defense, Security, and Sensing, International Society for Optics and Photonics. 801308-801308.
- United Nations. 2010. Department of Economic and Social Affairs, Population Division, UN. 2 United Nations Plaza, NY 10017 USA.
- Vidas, S., Moghadam, P. 2013. HeatWave: a handheld 3D thermography system for energy auditing. *Energy and Buildings*, 66, 445-460.
- Weng, Q. 2001. A remote sensing-GIS evaluation of urban expansion and its impact on surface temperature in the Zhujiang Delta, China. *International Journal of Remote Sensing*, 22, 1999–2014.
- Weng, Q. 2009. Thermal infrared remote sensing for urban climate and environmental studies: Methods, applications, and trends. *ISPRS Journal of Photogrammetry and Remote Sensing*, 64:4, 335-344.
- Weng, Q., Lu, D., Schubring, J. 2004. Estimation of land surface temperature–vegetation abundance relationship for urban heat island studies. *Remote Sensing of Environment*, 89:4, 467–483.
- Voogt, J.A., Oke, T.R. 1997. Complete urban surface temperatures. *Journal of Applied Meteorology*, 36, 1117–1132.
- Voogt, J.A., Oke, T.R. 2003. Thermal remote sensing of urban climates. *Remote Sensing of Environment*, 86, 370–384.

## **Linking Chapters 1 and 2**

In Chapter 1, we discuss why energy efficiency is important, and how individual households can contribute to energy efficiency, thereby improving the national economy and environment. We also discuss different techniques of measuring buildings' energy efficiency and the role of thermal infrared (TIR) remote sensing in doing so. Then we state the complexity of processing TIR imagery, followed by the statement of the objective of this research – focusing on post-processing TIR imagery.

To more fully understand thermal infrared imagery and its underlying complexity, Chapter 2 performs a thorough review of the literature describing thermography basics, different thermal sensors and their applications, urban applications of thermal remote sensing, the complexity of thermal remote sensing in observing the urban environment, and methods and models developed to overcome this complexity, along with their advantages and limitations.

## Chapter Two: Literature review

### 2.1 Thermography basics

Planck discovered that all objects (including vegetation, soil, water bodies, buildings, roads etc.) above absolute zero temperature emit electromagnetic radiation (Planck, 1901). For a given temperature, the amount of radiation emitted by an object is different for different wavelengths. At its normal temperature (~300 K) earth emits maximum energy between 3.0-14.0  $\mu\text{m}$  wavelengths, which is named as the thermal infrared region in the electromagnetic spectrum (Sabins, 1997).

Thermal infrared remote sensing accounts for the acquisition, processing and analysis of remote sensing data primarily acquired in the thermal infrared (TIR) region of the electromagnetic spectrum (Prakash, 2000). In contrast to optical remote sensing that measures reflected energy (~ 0.4 – 2.5  $\mu\text{m}$ ), thermal remote sensing measures the radiant energy *emitted* from ground objects, which is a function of the surface temperature (Norman and Becker, 1995). To explore the potential of thermal infrared remote sensing, it is necessary to develop an understanding of the following components: (i) Blackbody Radiation, (ii) Kinetic Energy and Kinetic Temperature and (iii) Emissivity.

#### 2.1.1 Blackbody radiation

In 1860, Gustav Kirchhoff introduced the concept of a blackbody as an imaginary object that absorbs all electromagnetic energy falling on it and then emits the same amount of energy (Kirchhoff 1896). Thus, a blackbody is a perfect absorber and a perfect emitter. However, true blackbodies are not found in reality. To quantify the amount of energy radiated from a blackbody, Stefan developed a law in 1879, based on experimental observation (Equation 2-1).

$$E_b = \sigma T_b^4 \quad (\text{Equation 2-1})$$

Where,

$E$  = Energy radiated from 1 sq. m. of black surface (Unit: watt/m<sup>2</sup>)

$\sigma$  (Stefan-Boltzmann constant) =  $5.67 \times 10^{-8}$  (Unit: watts/m<sup>2</sup>/ K<sup>4</sup>)

$T_b$  = Blackbody temperature in °K

In 1900, Max Planck demonstrated the *blackbody radiation law* (Equation 2-2) which relates radiant energy to blackbody temperature.

$$R = \frac{2\pi^5 hc^2}{15\pi^3 \lambda^5} \left( e^{\frac{hc}{\lambda k T_b}} - 1 \right)^{-1} \quad (\text{Equation 2-2})$$

Where,

$R$  = radiance value of TIR band in  $Wm^{-2}sr^{-1}\mu m^{-1}$

$\lambda$  = wavelength of TIR band in  $\mu m$

$T_b$  = black body temperature in °K

$h$  is the Planck's constant =  $6.63 \times 10^{-34} WS^2$

$c$  is the speed of light =  $3 \times 10^8 ms^{-1}$

$k$  is the Boltzmann's constant =  $1.38 \times 10^{-23} WSK^{-1}$

### **2.1.2 Kinetic energy and kinetic temperature**

All objects above absolute zero temperature display random motion. The energy/heat produced by this random motion is called kinetic heat/energy (Prakash, 2000), and its unit of measure is the calorie. Kinetic temperature is the measure of the concentration of kinetic heat (Norman and Becker, 1995), which is typically measured in °K or °C.

As noted by Planck's law, an object emits a portion of its kinetic energy and there exists a strong correlation between an object's kinetic energy and radiant energy (Elachi and Van Zyl,

2006). Radiant energy is the energy emitted by a particular source and carried by electromagnetic waves. This is the energy (of objects) that thermal remote sensing measures.

### 2.1.3 Emissivity

Depending on the physical properties, an object emits only a portion of its absorbed energy. Emissivity expresses the ability of an object to emit energy. It can be defined (Equation 2.3) as the ratio between the actual radiance emitted by an object and the blackbody radiance at the same temperature (Jacob et al., 2004). The following Table (Table 2-1) shows the emissivity of common urban surfaces.

**Table 2-1: Different types of roof material used in Calgary and their associated emissivity (@ 3.7-4.8 μm).**

Roof Material	Emissivity *
<b>Asphalt Shingles</b>	0.90
<b>Clay Tile</b>	0.75
<b>Cedar Shakes</b>	0.86
<b>Tar &amp; Gravel</b>	0.97
<b>Wood Shingles</b>	0.85
<b>Concrete Tiles</b>	0.95
<b>Metal</b>	0.25
<b>Fiberglass</b>	0.88
<b>Vinyl Shingles</b>	0.90
<b>Pine Shakes</b>	0.85
<b>Roll Roofing</b>	0.90
<b>EPDM Membrane</b>	0.93

Source: Raytek, 2014

$$T_s = T_b \varepsilon^{\frac{1}{4}} \quad \text{(Equation 2-3)}$$

Where,

$T_s$  = Surface temperature in °K

$T_b$  = black body temperature in °K

$\varepsilon$  = Emissivity value

## **2.2 Thermal sensors and their applications**

Thermal imaging began its journey in the early 20th century as a tool for military applications. But soon, its advantages for earth observation were also recognized by the scientific community. In the 1960s, a number of private companies developed publicly available thermal remote sensing sensors that were primarily carried by aircraft (Jensen, 2007). To date, a variety of thermal sensors are available on different space -, air- and handheld-platforms for different applications. A brief description of such TIR imaging systems is provided in Sections 2.2.1 to 2.2.3, followed by their applications in urban environments (Section 2.2.4).

### **2.2.1 Satellite based thermal sensors– a brief history**

- The Television Infrared Operational Satellite (TIROS-1) was launched in 1960 as the first declassified satellite to collect thermal remote sensing data, and was designed to collect lower resolution (6 km) thermal infrared data for environmental monitoring (Jensen, 2007).
- In 1978, NASA launched the Heat Capacity Mapping Mission (HCMM) to observe temperatures of the earth's surface during the day and night time. This satellite operated in two major wavelengths and followed a near polar sun-synchronous orbit at an altitude of 620 km (was later decreased to 540 km). It covered parts of the US, Canada, Europe, Africa, and Australia (Short and Stuart, 1982).

- The TIROS-N was launched in 1978 with a new multispectral (four channel) thermal imager called Advanced Very High Resolution Radiometer (AVHRR). This imager was later improved by AVHRR/2 having five channels. The AVHRR/2 was first carried by NOAA-7, which was launched in 1981. AVHRR/3 is the latest of this series and has been used on board NOAA-15 for thermal imaging since 1998. It is expected to offer a better understanding of the clouds, and land and sea surface temperatures (Tucker, 1996).
- In the Landsat program, thermal bands were first added to Landsat 4 in 1982. Since then, Landsat has been collecting thermal data of the earth's surface in two spectral bands at a 120 meter spatial resolution. The thermal bands of Landsat 7 (Launched in 1999) have a spatial resolution of 60 meter. Recently launched (2013) Landsat 8 contains two thermal bands, collecting data at 100 meter spatial resolution. The Landsat thermal data is primarily used for mapping urban heat fluxes, cloud detection and screening, and forest fire assessments (Markham et al., 2004).
- As a part of NASA's Earth Observation System (EOS), the Advanced Spaceborne Thermal Emission Radiometer (ASTER) was placed on board the satellite platform Terra (launched in 1999). ASTER contains 3 subsystems; (i) Visible and Near Infrared (VNIR), (ii) Short Wave Infrared (SWIR) and (iii) Thermal Infrared (TIR). The TIR subsystem was designed to collect thermal data from 6 different bands at a 90 meter spatial resolution. The VNIR and SWIR bands have a spatial resolution of 15 meter. The moderate-resolution multiband imagery provided by ASTER-TIR is ideal for obtaining a detailed distribution of surface temperatures (Watanabe et al., 2011).
- The Moderate Resolution Imaging Spectroradiometer (MODIS) is an instrument on board Terra and Aqua satellites. MODIS collects thermal data of the earth's surface at a 1.09 km

spatial resolution twice a day (Terra: Daytime, Aqua: Nighttime). These relatively quick revisit period allow researchers to perform a near real time monitoring. In addition, day and night time data collection using the same instrument provides a great opportunity to analyze diurnal temperature patterns (Loveland and Hansen, 2012).

(Additional technical details including spatial/spectral resolution can be found in Tables 2-2 and 2-3).

**Table 2-2: Summary features of thermal infrared sensors carried by satellite platforms**

Satellite	Lifetime	Wavelength	Ground Resolution	Thermal Resolution	Swath Width	Altitude	Applications
HCMM	1978 – 1980	Thermal Infrared (0.55 – 1.1 $\mu\text{m}$ )	600 meter	0.4 ° C	715 Km	640 Km	<ul style="list-style-type: none"> <li>▪ Urban Heat Island study (Price, 1979; Carlson et al., 1981; Foster et al.; 1981; Vukovich, 1983; Henry et al. 1989)</li> </ul>
NOAA-AVHRR	1978 – Present	3.55 – 3.93 $\mu\text{m}$ 10.30 – 11.30 $\mu\text{m}$ 11.50 – 12.50 $\mu\text{m}$	1.09 Km	NA	2400 Km	850 Km	<ul style="list-style-type: none"> <li>▪ Urban Heat Island study (Carlson et al., 1977; Matson et al., 1978; Matson and Legeckis, 1980; Kidder and Wu, 1987; Casells et al., 1991; Gallo et al., 1993; Lee, 1993; Gallo and Tarpley, 1996; Hafner and Kidder, 1999;</li> <li>▪ Relation between urban surface temperature and air temperature (Dousset, 1989; Epperson et al., 1995)</li> <li>▪ Relation between urban surface temperature and land use/urbanization (Balling and Brazel, 1988; Owen et al., 1998; Carlson and Sanchez-Azofeifa, 1999;</li> <li>▪ Urban-rural temperature variability (Streutker, 2002)</li> </ul>
MODIS	1999 - present	10.78 – 11.28 $\mu\text{m}$ 11.77 – 12.27 $\mu\text{m}$	1 Km	NA	2330 Km	705 Km	<ul style="list-style-type: none"> <li>▪ Surface temperature study (Wan and Li, 1997; King et al., 2003)</li> <li>▪ Atmospheric temperature and moisture study (Seemann et al., 2003)</li> </ul>

**Table 2-3: Summary features of thermal infrared sensors carried by satellite platforms (continued)**

Satellite	Lifetime	Wavelength	Ground Resolution	Thermal Resolution	Swath Width	Altitude	Applications
Landsat TM/ETM+	1984 – Present	10.8 $\mu\text{m}$ 12.0 $\mu\text{m}$	120 m	0.35-0.4 K	185 Km	705 Km	<ul style="list-style-type: none"> <li>▪ Urban-rural temperature variability (Carnahan and Larson, 1990)</li> <li>▪ Urban surface temperature (Aniello et al., 1995; Nichol, 1996; Chen et al.; 2006; Gluch et al., 2006; Small, 2006)</li> <li>▪ Surface energy balance (Kim, 1992; Parlow 1999)</li> <li>▪ Relation between urban surface temperature and land use/urbanization (Lougeay et al., 1996; Weng, 2001; Weng et al., 2004)</li> <li>▪ Urban Heat Island study (Gallo and Owen, 1998)</li> <li>▪ 3-D representation of Urban temperature (Nichol 1998)</li> <li>▪ Air quality assessment (Wald and Baleynaud, 1999)</li> </ul>
ASTER	1999 – Present	8.12 – 8.47 $\mu\text{m}$ 8.47 – 8.82 $\mu\text{m}$ 8.92 – 9.27 $\mu\text{m}$ 10.25 – 10.9 $\mu\text{m}$ 10.95 – 11.6 $\mu\text{m}$	90 m	0.3 K	60 Km	900 Km	<ul style="list-style-type: none"> <li>▪ Urban surface temperature study (Jacob et al., 2004; Hartz et al., 2006; Lu and Weng, 2006)</li> <li>▪ Surface temperature anomaly (Coolbaugh et al., 2007)</li> <li>▪ Surface energy flux (French et al., 2005)</li> <li>▪ Forest fire detection (Giglio et al., 2008)</li> <li>▪ Surface temperature and emissivity study (Gillespie et al., 1998; Liang, 2001)</li> </ul>

### ***2.2.2 Airborne thermal infrared sensors***

Since most public satellites provide low (1-10 km) or moderate (60-250 m) spatial resolution thermal imagery, airborne thermal surveys are often performed to obtain more detailed results. Some commonly used thermal infrared airborne sensors are described below – with additional details provided in Table 2-4.

- Agema Infrared Systems is one of the pioneer companies in developing thermal infrared scanners. Their first TIR camera was developed in 1965 for power line inspections. The most popular Agema product is AGEMA 570 (FLIR, 2014).
- The Thermal infrared Multispectral Scanner (TIMS) was designed by NASA in the early 1980s, and is considered one of the earliest airborne sensors used to collect thermal data for scientific/research applications. ATLAS, another NASA designed sensor, is also widely used for airborne thermal surveys (Elachi and Van Zyl, 2006).
- ITRES, a Canadian commercial airborne remote sensing company, developed a series of thermal broadband imagers (TABI) to provide very high-spatial and temporal resolution imagery. The TABI-320 was the first thermal imager developed by ITRES in 2000 with a 0.1°C thermal resolution, and a nominal spatial resolution of 1.0 m at an 824 m altitude. The TABI-1800 developed in 2008 (commercially available in 2011) is the latest of this series, which provides a very fine thermal resolution (0.05 °C). It has a very high ground resolution of 50 cm at an altitude of 1.2 km, though airborne data as fine as 15 cm have also been collected (ITRES, 2014).

**Table 2-4: Summary features of thermal sensors carried by airborne platforms.**

Sensor	Wavelength	IFOV	Thermal Resolution	FOV	Applications
AGEMA	8 – 14 $\mu\text{m}$	90 m	2°C	20°x20°	<ul style="list-style-type: none"> <li>▪ Urban surface temperature study (Eliasson., 1992; Voogt and Oke, 1997; Voogt, 2000)</li> <li>▪ Heat flux modeling (Voogt and Grimmond, 2000)</li> </ul>
TIMS	8.2 – 8.6 $\mu\text{m}$ 8.6 – 9.0 $\mu\text{m}$ 9.0 – 9.4 $\mu\text{m}$ 9.4 – 10.2 $\mu\text{m}$ 10.2 – 11.2 $\mu\text{m}$ 11.2 – 12.2 $\mu\text{m}$	2.5 mrad	0.1-0.2K	76.56°	<ul style="list-style-type: none"> <li>▪ Surface temperature measurement (Kahle, 1987)</li> <li>▪ Validation of ASTER temperature emissivity separation algorithm (Gillespie et al., 1998)</li> <li>▪ Urban vegetation study (Quattrochi &amp; Ridd, 1998)</li> <li>▪ Calculation of emissivity (Hook et al., 1992, Hewison, 2001)</li> <li>▪ Spectral mixture analysis (Gillespie, 1992)</li> </ul>
ATLAS	3.35 – 4.20 $\mu\text{m}$ 8.20 – 8.60 $\mu\text{m}$ 8.60 – 9.00 $\mu\text{m}$ 9.00 – 9.40 $\mu\text{m}$ 9.60 – 10.2 $\mu\text{m}$ 10.2 – 11.2 $\mu\text{m}$ 11.2 – 12.2 $\mu\text{m}$	2 m	NA	30°	<ul style="list-style-type: none"> <li>▪ Thermal energy flux determination (Quattrochi and Luval, 1999; King et al., 2003)</li> <li>▪ Urban heat island study (Gonzalez et al., 2005; Gluch et al., 2006)</li> <li>▪ Study of urban thermal environment (Gluch, 2002)</li> <li>▪ Impervious surface mapping (McInerney and Lozar, 2007)</li> </ul>
TABI 320	8 – 12 $\mu\text{m}$	2.8 mrad	0.1 K	48°	<ul style="list-style-type: none"> <li>▪ Surface temperature study (Pu et al., 2006)</li> <li>▪ Urban waste heat mapping (Hay et al., 2011)</li> </ul>
TABI-1800	3.7 – 4.8 $\mu\text{m}$	0.7 m (0.023°)	0.001 K	40±2°	<ul style="list-style-type: none"> <li>▪ Urban waste heat mapping (Hay et al., 2014)</li> <li>▪ Relative Radiometric Normalization (Rahman, et al., 2014)</li> <li>▪ Microclimate Normalization (Rahman, et al., 2014)</li> <li>▪ Geo-Object Based Mosaicking (Rahman, et al., 2013)</li> </ul>

### ***2.2.3 Hand-held thermal infrared sensors***

Along with satellite and airborne thermal sensors, a number of hand held thermal sensors are also commercially available. While their applications range from home land-defense, policing, search and rescue, power line surveys, to automotive assessments and wild-life counts, many of these sensors are also used to collect field data to validate UAS<sup>8</sup>/airborne/satellite data and for in-home thermal energy assessments (Cooper and Asrar, 1989; Voogt and Oke, 1998; Soux et al., 2004). The most commonly used hand held thermal cameras/sensors include IRT (Manufactured by Everest Interscience) (Cooper and Asrar, 1989; Voogt and Oke, 1998; Soux et al., 2004), and MiniTemp-Automotive Handheld sensor (Manufactured by RayTek) (Savelyev and Sugumaran, 2008). Fusion technology (FLIR System) provides a series of hand held thermal sensors with varied technical properties (detection range, resolution etc.) and prices, ranging from \$5K to \$22K (FLIR, 2014).

### ***2.2.4 Thermal urban remote sensing applications***

The study of urban thermal patterns using remote sensing imagery was first performed by Rao (1972). Due to the very low-resolution (6 km) thermal imagery available at that time (1960-1984), early studies were limited to qualitative heat island analyses and rural/urban temperature comparisons (Kidder and Wu, 1987; Roth et al., 1989; Kim, 1992; Gallo and Owen, 1998; Streutker, 2002). A comparison between vegetation indices and surface temperatures was also performed by Gallo et al. (1993) at a coarse scale (1 km).

The public availability of moderate-resolution (120-100 m) thermal imagery from Landsat TM/ETM+, ASTER, and airborne ATLAS made it possible to study temperature variation within

---

<sup>8</sup> UAS – Unmanned Aerial Systems such are remote controlled planes and helicopters.

the urban environment. For example, Carnahan and Larson (1990) studied urban heat sinks using Landsat TM data. Nichol (1998) also used Landsat TM data to study the temperature variations within a high-rise housing estate in Singapore. She incorporated a 3D-GIS model in her study to estimate the wall temperature of high rise buildings. Several other studies were also performed to analyze the urban surface energy balance (Carlson et al., 1981; Kim, 1992; Parlow, 1999; French et al., 2005)

H-res (ATLAS, TIMS) airborne imagery have also been used for micro-scale (2-10 m) thermal mapping of urban areas (Eliasson, 1992; Voogt and Oke, 1997; Quattrochi and Ridd, 1998; King et al., 2003; Gonzalez et al., 2005; Pu et al., 2006; Gluch et al., 2006), with results amiable to validation from field observations (Voogt and Oke, 1997; Sugawara and Takamura, 2006; Savalvey and Sugumaran, 2008). Similarly, multiscale analysis has been performed to describe scale dependent urban thermal patterns (Weng et al., 2004; Pu et al., 2006; Rigo et al., 2006). Results show that the thermal response of similar ground objects can be different due to their location and orientation (Sugawara and Takamura, 2006).

### **2.3 Challenges in thermal remote sensing**

To apply thermal remote sensing for an accurate measurement of urban thermal characteristics, it is necessary to explore the limitations of thermal remote sensing. The major challenges for urban thermal remote sensing include: (i) complexity of the urban surface, (ii) atmospheric and microclimatic influence on thermal response, and (iii) the difference between *radiant* temperature and *true kinetic* temperature. These components are briefly described in sections 2.3.1 to 2.3.3.

### ***2.3.1 Complexity of urban surface and varied sun-surface-sensor geometry***

The influences of complex urban surfaces and anisotropic variations on the resulting urban thermal patterns were summarized by Roth et al. (1989). Fortunately, well established and verified models are also available to take into account the three dimensional distribution of vegetation cover (Goel et al., 1991; Qin and Gerstl, 2000). However, the complexity of urban surfaces makes it difficult to develop generally applicable models, especially at very fine scales. For example, Voogt and Oke (1997) attempted to model complex urban structure, by presenting buildings as blocks over a plane surface. Their model provided a generalized representation of urban structure but ignored the presence of vegetation and other permeable features within the urban space. Similarly, Soux et al., (2004) developed the Surface Sensor Sun (SUM) model to determine the anisotropic variations in the radiant temperature measurement caused by both the position of the sensor and the sun. In this case, the urban area was also represented as uniform blocks. In a later study, Sugawara and Takamura (2006) considered roads as urban canyons and developed a numerical model to represent these urban structures as a canyon aspect ratio<sup>9</sup>.

Soux et al., (2004) and Sugawara and Takamura, (2006) describe sensor view models, which work with anisotropic variations very well, but their results are limited by the fact that they only approximate actual urban structures. In an effort to improve this, Voogt (2008) presented a modified SUM model (Soux et al., 2004), where he replaced the uniform blocks of buildings with the actual 3-D building models. He concluded that the combination of 3-D GIS building data and the SUM model was able to produce improved accuracy over previous studies. Other studies show that a combination of GIS and remote sensing techniques produce a realistic 3-D model of urban

---

<sup>9</sup> The canyon aspect ratio is defined as the ratio between the structure height and the canyon (road) width.

areas (Kim and Mullet, 1998; Frueh and Zakhor, 2003; Dollner and Buchholz, 2005) and can be incorporated with the sensor view models.

### ***2.3.2 Atmospheric and microclimatic influence on thermal response***

While propagating through the earth's atmosphere, electromagnetic energy is influenced in many ways. The atmosphere and the surrounding environment alter wavelengths, intensities, and spectral distribution of the radiation (Elachi and Van Zyl, 2006: Page 16). Thus, the amount of energy leaving the surface is both attenuated and enhanced on its way to the sensor. In thermal infrared remote sensing, the sensor recorded radiance is dominated by four main thermal components including: (i) Emitted radiation from the pixel, (ii) Solar radiation emitted by the atmosphere upward to the sensor, (iii) Radiation emitted by the atmosphere downward and reflected by the pixel upward, and (iv) Radiation emitted by the surrounding terrain into the pixel (Scott, 2007). However, thermal remote sensing is interested in (i) the emitted radiation from the pixel; the rest of the components add noise. The majority of the noise is contributed by the atmosphere from (i) Solar radiation emitted by the atmosphere upward to the sensor, and (ii) Radiation emitted by the atmosphere downward and reflected by the pixel upward. A large amount of research has been conducted to model atmospheric attenuation in remote sensing processes (Du et al., 2002). Some commonly used methods of atmospheric correction are described below.

#### **2.3.2.1 Correction for atmospheric interactions**

Most commonly used absolute atmospheric correction models are the radiative transfer models. Based on certain user inputs (including location of the scene, date and time of data acquisition, altitude of the sensor, mean elevation of the study area, visibility at the study area, thickness of the atmosphere, surface roughness, amount of aerosol in the atmosphere and other weather parameters) radiative transfer models create a model atmosphere and calculate the

atmospheric parameters for the model atmosphere. Usually radiosonde balloons are used to collect required weather data (Jensen, 2005). Radiative transfer models that are commonly used for thermal infrared image processing include (i) LOW spectral resolution atmospheric TRANSMittance algorithm and computer model (LOWTRAN) (Kneizys et al., 1983), and (ii) MODerate spectral resolution atmospheric TRANSMittance algorithm and computer model (MODTRAN) (Berk et al., 1989).

LOWTRAN is a low-resolution propagation model that was originally developed by US Air Force Geophysical Laboratory to predict transmission losses and sky effects on remote measurement (Kneizys et al., 1983). The spectral range of LOWTRAN model is 0 to 50,000  $\text{cm}^{-1}$  at a resolution of 20  $\text{cm}^{-1}$  (Kneizys et al., 1983). The basic assumptions of the model include (i) horizontally homogeneous atmosphere, and (ii) small elevation variation within the scene. LOWTRAN calculates the effects of molecular and particulate absorption/emission and scattering, surface reflections and emission, solar/lunar illumination, and spherical refraction that requires input parameters including air temperature, humidity, and aerosol content of the atmosphere, location of the study area and the time of data collection (Bosch and Alley, 1990). MODTRAN uses similar assumptions and technique as LOWTRAN but it operates at a finer spectral resolution (Berk et al., 1989). The spectral range extends from the UV into the far-infrared (0–50,000  $\text{cm}^{-1}$ ), providing resolution as fine as 0.2  $\text{cm}^{-1}$  (Berk et al., 1989).

The MODTRAN and LOWTRAN algorithms have been extensively used and validated over the last 30 years. Wright (1994) collected airborne thermal data to evaluate LOWTRAN and MODTRAN using a set of field survey data. In his assessment, high agreement between the field data and the airborne thermal data was observed for both models. Barsi et al. (2005) examined the applicability of MODTRAN on the Landsat TM thermal bands. It was shown that atmospheric

correction models applied to the Landsat thermal bands decreased radiometric error to less than  $0.5\pm 0.8$  K. Bosch and Alley (1990) used LOWTRAN to perform atmospheric correction on the Airborne Visible/Infrared Imaging Spectrometer (AVIRIS) data. They concluded that, the use of LOWTRAN minimizes the necessity of a priori knowledge of the study area and eliminates most of the errors induced by atmospheric interactions. Voogt and Oke (2003), Harris et al. (2005), and Sugawara and Takamura (2006) also successfully used LOWTRAN for atmospheric correction of airborne thermal imagery. However, correction using radiative transfer techniques requires large amounts of data collection and a very good understanding of the study area (Du et al., 2002). Even then, these expensive measurements (in terms of equipment and deployment costs) tend to be sparsely sampled, and provide a relatively uniform atmospheric correction parameter for a large area.

#### 2.3.2.2 Problems of urban atmosphere: *microclimate*

All atmospheric correction models estimate atmospheric correction parameters for a *uniform atmosphere* (Jensen, 2005). Such approximation for a rural area might produce very good results. However, it might fail to take into account the local variability resulting from urban microclimates.

The main components of local microclimate that influence thermal remote sensing are wind, precipitation, relative humidity<sup>10</sup>, surface moisture content, and presence of pollutants in the air (Giannini et al., 2003; Hartz et al., 2006). Wind helps to dilute pollutants (Oke, 1978). Also, surface winds increase convective heat loss from ground objects, and makes them cooler

---

<sup>10</sup> Relative humidity is a measure of the amount of moisture in the air at a given temperature relative to the maximum amount of moisture the air can hold at the same temperature and pressure.

(Santamouris et al., 2001). In general, wind speed is lower in urban areas than in rural areas and as the urban density increases, wind speed decreases (Auer, 1975). At a fine scale, urban wind is highly influenced by the vertical structures, which create urban canyons that funnel air down and along them (Figure 2-1). Consequently, the orientation of vertical structures and their varied height results in varied wind-speed and direction within the urban environment (Vardoulakis, 2002).

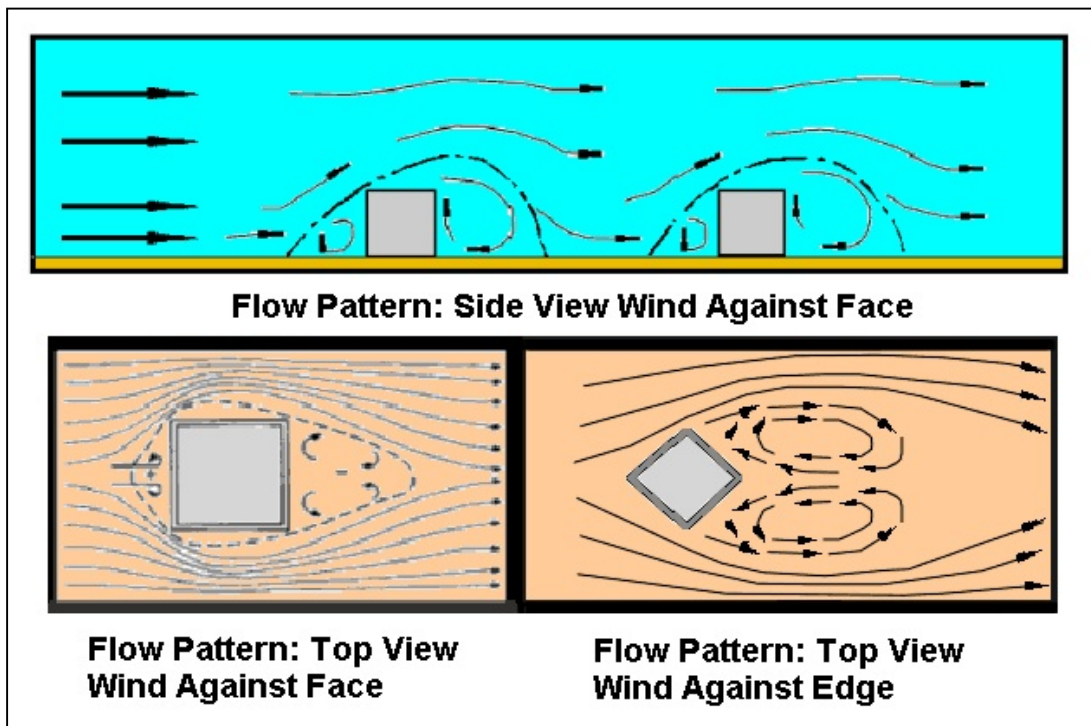


**Figure 2-1: Urban wind flow pattern from top and side<sup>11</sup>**

The presence of pollutants increases the absorption of thermal radiation (Landsberg, 1981). It is important to note that the urban atmosphere is characterized by concentrations of pollutants, which vary depending on the location of the pollutant source and the nature of air circulation. For example, point sources like industries have a very high concentration of pollutants at the source, with pollutants being increasingly dispersed away from the source, based on the dominant wind

---

<sup>11</sup> Source: <http://www.islandnet.com/~see/weather/elements/citywind.htm>

direction (Turner, 1970). In the case of line sources such as roads, pollution concentration is highest at the source and the nature of its dispersion depends on the presence of vertical structures (primarily buildings) along the side of the source (Mu and Peng, 2009). An example is given in figure 2-2 that shows the variability of PM<sub>10</sub><sup>12</sup> (Particulate Matter) concentration in the City of Leicester, UK (Pierse et al., 2006). A strong concentration of PM<sub>10</sub> is observed within the city core (brown). As the concentration of pollutants changes, the amount of atmospheric absorption is also altered, imposing varying amounts of noise within the remote sensor's field of view.

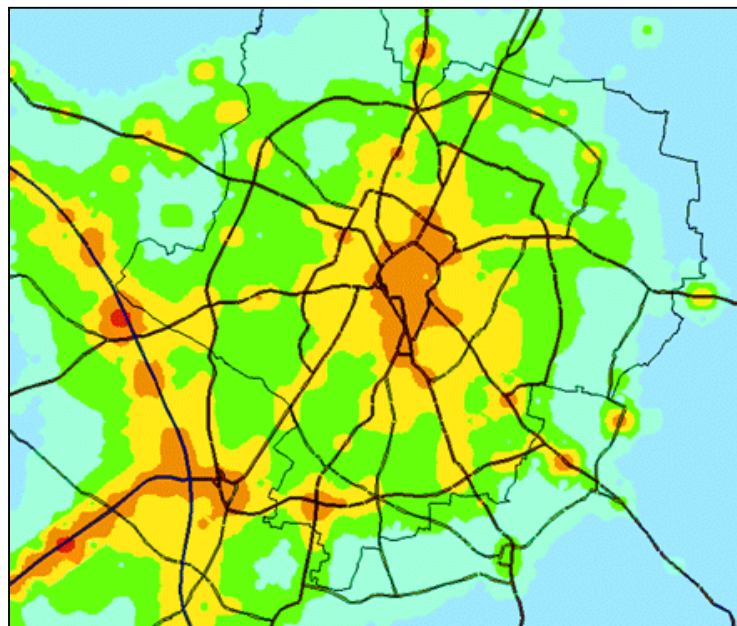


**Figure 2-2: Map of annual mean total PM10 for Leicester. The spectrum ranges from blue (low concentration of PM10) to green, yellow, orange and red (High concentration of PM10) (Pierse et al., 2006).**

### ***2.3.3 Difference between radiant temperature and true kinetic temperature***

As discussed in the ‘Thermography basics’ section (2.1), the radiant temperature of an object (observed by a remote sensor) and its true kinetic temperature are not the same. The portion

---

<sup>12</sup> PM<sub>10</sub> are tiny amounts of solid matter (greater than 10 micrometers in diameter) suspended in the air.

of the kinetic temperature that is recorded by the sensor is determined by the emissivity of the surface. Surface emissivity is different for different objects and is highly influenced by the object's color, surface roughness, moisture content, compaction, field of view, and wavelength (Jensen, 2007). Objects having the same kinetic temperature on the earth's surface might exhibit very different radiant temperatures when viewed with a thermal sensor, (Figure 2-3), as their emissivities may be different.

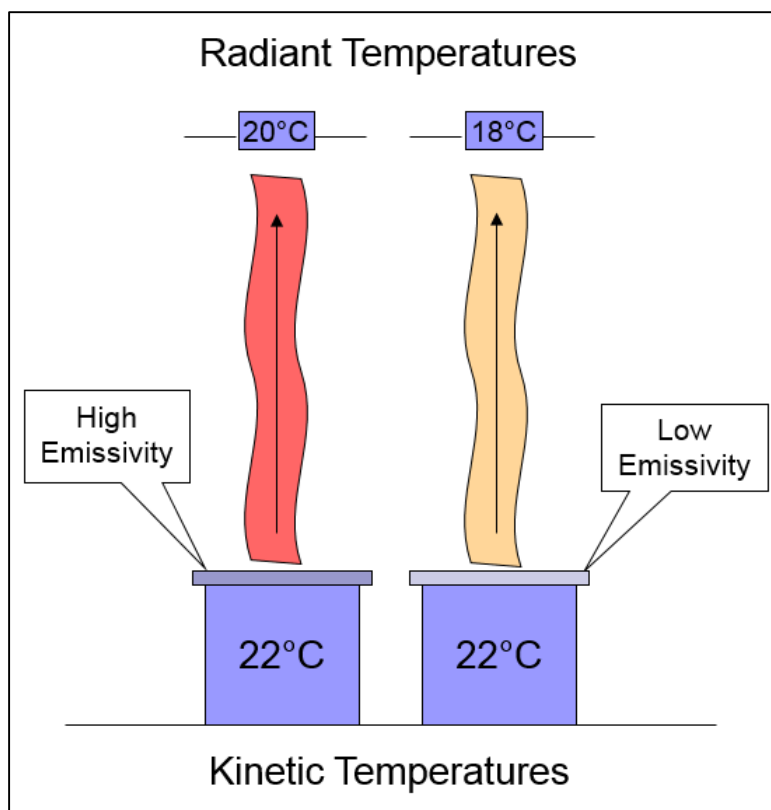


**Figure 2-3: An example of the Effect of Emissivity on Radiant Temperature. Each house has the same internal true temperature (22°C). However, the roof of each house is composed of materials with different emissivity. Consequently the sensor views a different radiant temperature for each roof.**

Therefore, to measure true kinetic temperature in a TIR image, it is necessary to correct for emissivity. For a rural homogeneous vegetated surface, it may be relatively easy to estimate

emissivity, but for a complex heterogeneous urban surface, it is not trivial to accurately estimate the emissivity of all the different objects composing a scene.

The correction to true temperature (from sensor observed radiant temperature) would be perfect, if one had a database containing a map of the entire city with associated attributes including landcover type (building, road, footpath, grass lawn, tree etc.), surface material (shingle, concrete, tar, asphalt, brick, bitumen etc.), surface color, roughness etc. But unfortunately, with the available technology it is almost impossible to create such a comprehensive database. In addition, the sensor does not look at a single object; rather it looks at whatever falls within its *instantaneous field of view*<sup>13</sup> (IFOV). Within a heterogeneous urban surface, there is a strong possibility of viewing portions of different objects (each with different emissivity) at a single instance in time. However, it is not currently possible to accurately correct for different portions of an IFOV (a single pixel) using different emissivity measures due to the lack of the required datasets. Therefore, correcting urban features for emissivity remains a challenge. To normalize thermal images for different emissivities, researchers have used different methods; some of which are briefly discussed in the next section.

While studying the surface temperature of ground objects using remote sensing technologies, several studies have neglected the effects of emissivity due to relatively coarse image resolutions and/or a lack of detailed information on ground targets (Kidder and Wu, 1987; Roth et al., 1989; Gallo et al., 1993; Chen et al., 2006; Xian and Crane, 2006). It has also been argued that, the varied emissivity of surface materials has an insignificant influence on the qualitative analysis of surface temperature variations (Kidder and Wu, 1987; Xian and Crane, 2006). Despite

---

<sup>13</sup> Solid angle through which a detector is sensitive to radiation

arguments to the contrary, attempts have been made to quantify the effects of emissivity on estimating the true kinetic temperature of specific ground objects and/or landcover types. One of the simplest methods is to integrate landuse data with the corresponding thermal imagery (Balling and Brazel, 1988; Weng, 2001). For example, Saveljev and Sugumaran (2008) collected the radiant temperature of ground-objects with known emissivity. The emissivity of these field samples were integrated with Planck's Law (Rybicki and Lightman 1979) to develop an empirical regression model for calculating the true kinetic temperature of the corresponding pixels in the image. More recently, Nichol (2009) proposed the *Emissivity Modulation* method (similar to image sharpening described by Gustavson et al., 2003) to correct an ASTER (90 m) thermal image for emissivity. This method used a geographically corresponding higher resolution optical image (15 m ASTER) to classify ground objects. The emissivity values corresponding to these land classes were then integrated with the lower resolution thermal image to calculate true kinetic temperature and increase the resolution of the thermal scene. While none of these methods is able to completely solve the problem of emissivity, they provide effective means to cope with the situation.

#### **2.4 An introduction to the study area**

The City of Calgary is located approximately 80 km east to the front ranges of Canadian Rockies. It experiences a dry and humid continental climate, which is characterized by large seasonal temperature differences with warm and hot summers and cold winters. Being located in the heart of Canadian Prairies, Calgary is generally windy. The Chinook wind (a hot and dry wind that blasts from the Canadian Rockies) regularly blows in the city during the winter months (Brinkmann, 1970). The winter in Calgary can be very cold, with temperatures going down to -45 °C. However, the warm Chinook wind often raise the winter temperature by as much as 20-

30 °C within a few hours. Calgary is one of the sunniest cities in Canada with an average of ~332 days of sunshine<sup>14</sup>.

#### ***2.4.1 Microclimatic condition at the time of data collection***

Standard climate conditions for collecting TIR data for urban waste heat mapping should meet the following conditions (Jensen, 2007):

- Standing water, ice, or snow should not be present on the surface as it has a significant influence on emissivity characteristics.
- Wind speed should be lower than 7 km/hr.
- Humidity of ground fog should be minimum.
- Cloud cover should be minimum.

The data for this research were collected over The City of Calgary on May 12-13, 2012 between 11:00 pm and 5:00 am under clear sky conditions. For a large metropolitan area like Calgary where weather is largely unpredictable, it is extremely challenging to have perfect data collection situation over the entire study area. However, to mitigate adverse climate conditions, we selected the month of May for two main reasons: (i) in Calgary, snow is generally melted by the end of April, and (ii) the average monthly wind speed is comparatively low during May<sup>15</sup>. Unfortunately, there was an unexpected snowfall (totaling ~10 cm) a week before the data collection. However, the average daytime temperature of that week was ~16 °C (maximum 25.1 °C and minimum 8.5 °C) which we believe melted all the snow. The reported wind speed during the data acquisition was 5-13 km/hr. with winds gusting to ~20 km/hr. There was no precipitation

---

<sup>14</sup> <http://www.weatherstats.ca/winners.html?46>

<sup>15</sup> <http://www.myweather2.com/City-Town/Canada/Alberta/Calgary/climate-profile.aspx?month=5>

from May 10-13 and these days were mostly sunny. We also chose a late night data acquisition as:

- (i) the earth's surface is expected to reach a more stable thermal condition during the late night,
- and (ii) the impact of sun-surface-sensor geometry on sensor observation is mitigated.

## References:

- Aniello, C., Morgan, K., Busbey, A., Newland, L. 1995. Mapping micro urban heat islands using Landsat TM and a GIS. *Comparative Geoscience*, 21, 965–969.
- Auer, J.A.H. 1975. Calculation of divergence from the wind field over an urban area. U.S Natl Conference Wind Eng. Res. Ft Collins, Colorado. 2: I-20-1 – I-20-3 (Cermak, J.E. Edited).
- Balling, R.C., Brazell, S.W. 1988. High-resolution surface temperature patterns in a complex urban terrain. *Photogrammetric Engineering and Remote Sensing*. 54, 1289–1293.
- Barsi, A.J., Schott, J.R., Palluconi, F.D., Hook, S.J. 2005. Validation of web-based atmospheric correction tool for single thermal band instrument. *Proceedings, SPIE*, 5882.
- Berk, A., Bernstein, L. S., Robertson, D. C. 1989. MODTRAN A Moderate Resolution Model for LOWTRA7N, AFGL-TR-89-0122, U.S. Air Force Geophysics Laboratory, Hanscom Air Force Base.
- Bosch, J.M., Alley, R.E. 1990. Application of LOWTRAN 7 as an atmospheric correction to airborne visible/infrared imaging spectrometer (AVIRIS) data. *IGRASS '90*. 175-177.
- Brinkmann, W.A. 1970. The chinook at Calgary (Canada). *Archiv für Meteorologie, Geophysik und Bioklimatologie, Serie B*, 18:3-4, 269-278.
- Carlson T.N., Augustin J.E.A, Bolandf, E. 1977. Potential application of satellite temperature measurements in the analysis of land use over urban areas. *Bulletin American Meteorological Society*. 58, 1301-1 303.
- Carlson T.N., Dodd J.K., Benjamin, S.G., Cooper, J.M. 1981. Satellite estimation of the surface energy balance, moisture availability and thermal inertia. *Journal of Applied Meteorology*, 20-6747.

- Carslon, T.N., Sanchez-Azofeifa, G.A. 1999. Satellite remote sensing of land use changes in and around San Jose, Costa Rica. *Remote Sensing of Environment*. 70, 247– 256.
- Carnahan, W.H., Larson, R.C. 1990. An analysis of an urban heat sink. *Remote Sensing of Environment*, 33, 65–71.
- Caselles, L.V., Garcia, M.J., Melia, J., Perez C.A.J. 1991. Analysis of the heat-island effect of the city of Valencia, Spain through air temperature transits and NOAA satellite data. *Theoretical and Applied Climatology*. 43, 195– 203.
- Chen, X., Zhao, H., Li, P., Yin, Z. 2006. Remote sensing image based analysis of the relationship between urban heat island and land use/cover changes. *Remote Sensing of Environment*. 104, 133-146.
- Coolbaugh, M.F., Kratt, C., Fallacaro, A., Calvin, W.M., Taranik, J.V. 2007. Detection of geothermal anomalies using Advanced Spaceborne Thermal Emission and Reflection Radiometer ASTER thermal infrared images at Brady's Hot Springs, Nevada, USA. *Remote Sensing of Environment*, 106, 350-359.
- Cooper D., Asrar, G. 1989. Evaluating atmospheric correction models for retrieving surface temperature from the AVHRR over a tall grass prairie, *Remote Sens. Environ.* 27, 93–102.
- Döllner, J., Buchholz, H. 2005. Continuous level-of-detail modeling of buildings in 3D city models. In: *Proc. of ACM GIS*, ACM Press.
- Dousset, B. 1991. Surface temperature statistics over Los Angeles: The influence of land use. *Proceedings of IGARSS-91*, New York, NY: IEEE, 367–371.
- Du, Y., Teillet, P.M., Cihlar, J. 2002. Radiometric normalization of multitemporal high-resolution satellite images with quality control for landcover change detection. *Remote Sensing of Environment*. 82-123.

- Elachi, C., Van Zyl, J. J. 2006. Introduction to the physics and techniques of remote sensing; Vol. 28. John Wiley & Sons.
- Eliasson, I. 1992. Infrared thermography and urban temperature patterns. *International Journal of Remote Sensing*, 13, 869– 879.
- Epperson, D.L., Davis, J.M., Bloomfield, P., Karl, T.R., McNab, A.L., Gallo, K.P. 1995. Estimating the urban bias of surface shelter temperatures using upper-air and satellite data 2. Estimation of the urban bias. *Journal of Applied Meteorology*, 34, 358– 370.
- FLIR, 2014. website: <http://www.flir.com/thermography/americas/us/content/?id=17862>, last accessed June 10, 2014.
- Foster J.L., Ormsby, J.P., Gurney R.J. 1981. Satellite observations of England and North-Western Europe. *Weather*, 36, 252-259.
- French, A.N., Jacob, F., Anderson, M.C., Kustas, W.P., Timmermans, W., Gieske, A. 2005. Surface energy fluxes with the Advanced Spaceborne Thermal Emission and Reflection radiometer ASTER at the Iowa 2002 SMACEX site USA. *Remote Sensing of Environment*, 99:1–2, 55–65.
- Frueh, C., Zakhor, A. 2003. Constructing 3D city models by merging ground-based and airborne views. *IEEE Computer Graphics and Applications*, Special Issue Nov/Dec-2003. 52-41.
- Gallo, K.P., McNab, A.L., Karl, T.R., Brown, J.F., Hood, J.J., Tarpley, J.D. 1993. The use of a vegetation index for assessment of the urban heat island effect. *International Journal of Remote Sensing*, 14, 2223–2230.
- Gallo, K.P., Owen, T.W. 1998. Assessment of urban heat island: A multi-sensor perspective for the Dallas-Ft. Worth, USA region. *Geocarto International*, 13: 4, 35–41.

- Giannini, A., Saravanan, R., Chang, P. 2003. Oceanic forcing on sahel rainfall on interannual to interdecade time scales. *Science*. 302:5647, 1027-1030
- Giglio, L., Csiszar, I., Restas, A., Morisette, J.T., Schroeder, W., Morton, D., Justice, C.O. 2008. Active fire detection and characterization with the advanced spaceborne thermal emission and reflection radiometer ASTER, *Remote Sensing of Environment* 112, 3055–3063.
- Gillespie, A., Rokugawa, S., Matsunaga, T., Cothorn, J. S., Hook, S., Kahle, A. B. 1998. A temperature and emissivity separation algorithm for Advanced Spaceborne Thermal Emission and Reflection Radiometer ASTER images. *IEEE Transactions on Geoscience and Remote Sensing*, 36: 4, 1113 - 1126.
- Gluch, R. 2002. Using high-spatial resolution airborne thermal-IR data to map the urban thermal environment. *IEEE International Geoscience and Remote Sensing Symposium*. 1923-1925.
- Gluch, R., Quattrochi, D.A., Luvall, J.C. 2006. Multi-scale approach to urban thermal analysis, *Remote Sensing of Environment*. 104:2, 123–132.
- Goel, N.S., Knox, L.B., Norman, J.M. 1991. From artificial life to real life: Computer simulation of plant growth *International Journal of General System*. 18, 291–319.
- Gonzalez, J.E., Luvall, J.C., Rickman, D., Comarazamy, D., Picon, A.J., Harmsen, E.W., Parsiani, H., Ramirez, N., Vasquez, RE., Williams, R., Waide, R.B., Tepley, C.A. 2005. Urban heat islands developing in coastal tropical cities. *Eos, Transactions American Geophysical Union*. 86, 397- 403.
- Gustavson, W.T., Handcock, R., Gillespie, A.R., Tonooka, H. 2003. An image sharpening method to recover stream temperatures from ASTER images, *Remote Sensing for Environmental Monitoring, GIS applications and Geology* M. Ehlers, editor, *Proceedings of SPIE*, 4886, 72–83.

- Hafner, J., Kidder, S.Q. 1999. Urban heat island modeling in conjunction with satellite-derived surface/soil parameters. *Journal of Applied Meteorology*. 38, 448– 465.
- Harris, A.J.L., Dehn, J., Patrick, M.R., Calvari, S., Ripepe, M., Lodato, L. 2005. Lava effusion rates from hand-held thermal infrared imagery: an example from the June 2003 effusive activity at Stromboli. *Bulletin of Volcanology*. 68, 107–117.
- Hartz, D.A., Prashad, L., Golden, J., Brazel, A. J. 2006. Linking satellite images and hand held infrared thermography to observe neighborhood climate conditions. *Remote Sensing of Environment*. 104:2. 190-200.
- Hay, G. J. 2014. GEOBIA – Evolving Beyond Segmentation. Keynote Presentation at the 5th International GEOBIA Conference, Thessaloniki, Greece, May 24, 2014 <http://geobia2014.web.auth.gr/geobia14/sites/default/files/pictures/hay.pdf> - last visited Sept 01, 2014.
- Hay G.J., Kyle C., Hemachandran B., Chen G., Rahman M.M., Fung T.S., Arvai J.L. 2011. Geospatial Technologies to Improve Urban Energy Efficiency. *Remote Sensing*. 3:7, 1380-1405.
- Henry, J.A., Dicks, S.E., Wetterqvist, O.F., Roguski, S.J. 1989. Comparison of satellite, ground-based, and modeling techniques for analyzing the urban heat island. *Photographic Engineering of Remote Sensing*, 55, 69– 76.
- Hewison, T.J. 2001. Airborne measurements of forest and agricultural land surface emissivity at millimeter wavelengths. *IEEE Transactions on Geoscience and Remote Sensing*. 39:2, 393-400.
- Hook, S.J., Gabell, A.R., Green, A.A., Kealy, P.S. 1992. A comparison of techniques for extracting emissivity information from thermal infrared data for geologic studies. *Remote Sensing of Environment*. 42:2, 123-135.

- ITRES, 2014. website: <http://itres.com/products/imagers/tab1800/>, last accessed: June 10 2014.
- Jacob, F., Francois, P., Schmugge, T., Vermote, E., French, A., Ogawa, K. 2004. Comparison of Land Surface Emissivity and Radiometric Temperature Derived from MODIS and ASTER. *Remote Sensing of Environment*, 90, 137-152.
- Jensen, J. R. 2005. *Introductory digital image processing: a remote sensing perspective* 3<sup>rd</sup> edition. Prentice-Hall Inc.
- Jensen, J. R. 2007. *Remote Sensing of the Environment: An Earth Resource Perspective* 2<sup>nd</sup> edition. Upper Saddle River: Pearson Prentice Hall.
- Kahle, A.B. 1986. Surface emittance, temperature, and thermal inertia derived from Thermal Infrared Multispectral Scanner TIMS data for Death Valley, California. *Geophysics*. 52:7, 858 - 874.
- Kidder, S.Q., Wu, H.T. 1987. A multispectral study of the St. Louis area under snow-covered conditions using NOAA-7 AVHRR data. *Remote Sensing of Environment*, 22, 159–172.
- Kim, H.H. 1992. Urban heat island. *International Journal of Remote Sensing*, 13, 2319–2336.
- Kim, T., Muller, J.P. 1998. A technique for 3D building reconstruction. *Photogrammetric Engineering & Remote Sensing*. 64, 923–930.
- King, M.D., Menzel, W.P., Kaufman, Y.J., Tanre, D., Gao, B.C., Platnick, S., Ackerman, S.A., Remer, L.A., Pincus, R., Hubanks, P.A. 2003. Cloud and aerosol properties, precipitable water, and profiles of temperature and water vapor from MODIS, *IEEE Transaction of Geoscience and Remote Sensing*. 41, 442 - 458.
- Kirchhoff, G. 1896. On the relation between the Radiating and Absorbing Powers of different Bodies for Light and Heat, translated by F. Guthrie in *Philosophical Magazine Letters*. 4:20-130, 1-21.

- Kneizys, F.X., Shettle, E.P., Gallery, W.O., Chetwynd, J.H., Abreu, L.W., Selby, J.E.A., Clough, S.A., Fenn, R.W. 1983. Atmospheric transmittance/ radiance: computer code LOWTRAN 6. Air Force Geophysics Laboratory, Environmental Research Paper 846, Hanscom AFB, MA
- Landsberg, H.E. 1981. *The Urban Climate*. Academic Press, New York, 285 p.
- Lee, H.Y. 1993. An application of NOAA AVHRR thermal data to the study of urban heat islands. *Atmospheric Environment*, 27- B, 1–13.
- Liang, S. 2001. An optimization algorithm for separating land surface temperature and emissivity from multispectral thermal infrared imagery. *IEEE Transactions on Geoscience and Remote Sensing* 39, 264–274.
- Lougeay, R., Brazel, A., Hubble, M. 1996. Monitoring intra-urban temperature patterns and associated landcover in Phoenix, Arizona using Landsat thermal data. *Geocarto International*, 11, 79– 89.
- Loveland, T.R., Hansen, M.C. 2012. Global Data Availability from US Satellites: Landsat and MODIS. *Global Forest Monitoring from Earth Observation*, 69.
- Lu, D., Weng, Q., 2006. Use of impervious surface in urban land-use classification. *Remote Sensing of Environment*, 102, 146–160.
- Markham, B.L., Storey, J.C., Williams, D.L., Irons, J. R. 2004. Landsat sensor performance: history and current status. *Geoscience and Remote Sensing, IEEE Transactions on*, 42:12, 2691-2694.
- Matson, M., McClain, E.P., McGinnis, D.F., Puitcharj, D.A. 1978. Satellite detection of urban heat islands, *Monthly Weather Review*, 106, 1725-1734.
- Matson, M., Legeckis, R.V. 1980. Urban heat island detected by satellite. *Bulletin American meteorological Society*, 61,212.

- McInerney, M., Lozar, R.C. 2007. Comparison of methodologies to derive a Normalized Difference Thermal Index NDTI from ATLAS imagery, In Proceedings of the ASPRS 2007 Annual Conference, Tampa FL.
- Mu, H., Peng, W. 2009. Numerical Simulation of Dispersion of Air Pollutant around Buildings. Computer Science and Information Engineering, 2009 WRI World Congress on. March 31 2009-April 2 2009.
- Nichol, J.E. 1996. High-resolution surface temperature patterns related to urban morphology in a tropical city: A satellite-based study. *Journal of Applied Meteorology*, 35, 135-146.
- Nichol, J.E. 1998. Visualisation of urban surface temperatures derived from satellite images. *International Journal of Remote Sensing*, 19, 1639-1649.
- Nichol, J.E. 2009. An Emissivity Modulation Method for Spatial Enhancement of Thermal Satellite Images in Urban Heat Island Analysis. *Photogrammetric Engineering & Remote Sensing*. 75:5, 1-10.
- Norman, J. M., Becker, F. 1995. Terminology in thermal infrared remote sensing of natural surfaces. *Agricultural and Forest Meteorology*. 77:3, 153-166.
- Oke, T.R. 1978. *Boundary Layer Climates*. Methuen and Co. Ltd. 11 New fetter Lane London EC4P 4EE.
- Oke, T.R. 1997. *Urban Climates and Global Environmental Change*. In: Thompson, R.D. and A. Perry eds. *Applied Climatology: Principles & Practices*. New York, NY: Routledge, 273-287.
- Otterman, J., Susskind, J., Brakke, T., Kimes, D., Pielke, R., Lee, T.J. 1995. Inferring the thermal-infrared hemispheric emission from a sparsely vegetated surface by directional measurements. *Boundary – Layer Meteorology*, 74, 163–180.

- Owen, T.W., Carlson, T.N., Gillies, R.R. 1998. An assessment of satellite remotely-sensed landcover parameters in quantitatively describing the climatic effect of urbanization. *International Journal of Remote Sensing*, 19, 1663–1681.
- Parlow, E. 1999. Remotely-sensed heat fluxes of urban areas. In de Dear, et al. Eds., *Biometeorology and urban climatology at the turn of the millennium*. WMO Tech. Doc., Geneva, Switzerland: World Meteorological Organization, 1026, 523–528.
- Pierse, N., Rushton, L., Harris, R.S., Kuehni, C.E., Silverman, M., Grigg, J. 2006. Locally generated particulate pollution and respiratory symptoms in young children. *Thorax*. 61, 216–220.
- Planck, M. 1901. On the law of the energy distribution in the normal spectrum. *Ann. Phys.* 4:553, pp. 90.
- Prakash, A. 2000. Thermal remote sensing: concepts, issues and applications. *International Archives of Photogrammetry and Remote Sensing*, XXXIII: B1.
- Price J.C. 1979, Assessment of the urban heat island effect through the use of satellite data. *Monthly Weather Review*. 107, 1554-1557.
- Pu, R., Gong, P., Michishita, R., Sasagawa, T. 2006 Assessment of multi-resolution and multi-sensor data for urban surface temperature retrieval. *Remote Sensing of Environment*. 104, 211-225.
- Qin, W., Gerstl, S.A.W. 2000. 3-D Scene modeling of semi desert vegetation cover and its radiation regime. *Remote Sensing of Environment*, 74, 145– 162.
- Quattrochi D.A., Luvall, J.C. 1999. Thermal infrared remote sensing for analysis of landscape ecological processes: methods and applications. *Landscape Ecol.* 14, 577–598.

- Quattrochi D.A., Ridd, M.K. 1998. Analysis of vegetation within a semi-arid urban environment using high-spatial resolution airborne thermal infrared remote sensing data. *Atmospheric Environment*, 32, 19–33.
- Rahman, M.M. Hay, G.J. Couloigner, I. Hemachandaran, B. 2014. Transforming image-objects into multiscale fields: a GEOBIA approach to mitigate microclimatic variability within a H-res thermal infrared urban scene. *Remote Sensing - Special Issue (ISSN 2072-4292): Advances in Geographic Object-Based Image Analysis (GEOBIA) – (Manuscript ID: remotesensing-60154) (Accepted)*.
- Rahman, M. M., Hay, G. J., Couloigner, I., Hemachandaran, B., Bailin, J. 2014. A comparison of four relative radiometric normalization (RRN) techniques for mosaicking H-res multi-temporal thermal infrared (TIR) flight lines of a complex urban scene. (PHOTO-D-14-00266). *The ISPRS Journal of Photogrammetry and Remote Sensing (Accepted)*.
- Rahman, M.M. Hay, G.J. Couloigner, I. Hemachandran, B. Bailin, J. Zhang Y. Tam, A. 2013. Geographic Object-Based Mosaicking (OBM) of High-resolution Thermal Airborne Imagery (TABI-1800) to improve the Interpretation of Urban Image-Objects. *Geoscience and Remote Sensing Letters, IEEE*. 10-4, 918-922.
- Rao, P. K. 1972. Remote sensing of urban heat islands from an environmental satellite. *Bulletin of the American Meteorological Society*, 53, 647– 648.
- Raytek, 2014. Website: <http://spectralemissivity.com/2013/12/17/rayteks-online-spectral-emissivity-guide/>. Last accessed: June 25, 2014.
- Rigo, G., Parlow, E., Oesch, D. 2006. Validation of satellite observed thermal emission with in-situ measurements over an urban surface. *Remote Sensing of Environment*, 104, 201–210.

- Roth, M., Oke, T.R., Emery, W.J. 1989. Satellite-derived urban heat island from three coastal cities and the utilization of such data in urban climatology. *International Journal of Remote Sensing*, 10, 1699–1720.
- Rybicki, G.B., Lightman, A.P. 1979. *Radiative Process in Astrophysics*. New York: John Wiley and Sons. ISBN - 0-471- 82759-2.
- Sabins, F.F. 1997. *Remote sensing: principles and interpretation*. New York: W.H. Freeman and Company.
- Santamouris M., Papanikolaou N., Livada I., Koronakis I., Georgakis A., Assimakopoulos D.N. 2001. On the impact of urban climate on the energy consumption of buildings. *Solar Energy*, 70:3, 201-216.
- Savelyev, A., Sugumaran, R. 2008. Surface temperature mapping of the University of Northern Iowa campus using high-resolution thermal infrared airborne imageries. *Sensors*, 8, 5055-5068.
- Schott, J. 2007. *Remote sensing the image chain approach*. Oxford Press, 2nd edition.
- Seemann, S.W., Li, J., Menzel, W.P., Gumley L.E. 2003. Operational retrieval of atmospheric temperature, moisture, and ozone from MODIS infrared radiances. *Journal of Applied Meteorology*. 42, 1072.
- Short, N.M., Stuart Jr, L.M. 1982. *The heat capacity mapping mission (HCMM) anthology*. NASA SP-465. NASA Special Publication, 465.
- Small, C. 2006. Comparative analysis of urban reflectance and surface temperature. *Remote Sensing of Environment*. 104, 168-189.
- Soux, C.A., Voogt, J.A., Oke, T.R. 2004. A model to calculate what a remote sensor ‘sees’ of an urban surface. *Boundary - Layer Meteorology*. 111, 109–132

- Streutker, D.R. 2002. A remote sensing study of the urban heat island of Houston, Texas, *International Journal of Remote Sensing*, 23:13, 2595 – 2608.
- Sugawara, H., Takamura, T. 2006. Longwave radiation flux from an urban canopy: evaluation via measurements of directional radiometric temperature. *Remote Sensing of Environment*. 104, 226-237.
- Tucker, C.J. 1996. History of the use of AVHRR data for land applications. In *Advances in the use of NOAA AVHRR data for land applications*. Springer Netherlands. 1-19.
- Turner D.B. 1970. *Workbook of Atmospheric Dispersion Estimates*. PHS Publication 999: AP-26.
- Vardoulakis, S., Fisher, B.E.A., Pericleous, K., Gonzalez-Flesca, N. 2002. Modeling air quality in street canyons; a review. *Atmospheric Environment*. 37:2, 155-182.
- Voogt, J.A. 2000. Image representations of urban surface temperatures. *Geocarto International*, 15, 19–29.
- Voogt, J.A. 2008. Assessment of urban sensor view model for thermal anisotropy. *Remote Sensing of Environment*, 112, 482-495.
- Voogt, J.A., Oke, T.R. 1997. Complete urban surface temperatures. *Journal of Applied Meteorology*, 36, 1117–1132.
- Voogt, J.A., Oke, T.R. 1998. Radiometric temperatures of urban canyon walls obtained from vehicle traverse. *Theoretical and Applied Climatology*. 60, 199-217.
- Voogt, J.A., Oke, T.R. 2003. Thermal remote sensing of urban climates. *Remote Sensing of Environment*, 86, 370–384.
- Vukovic, F.H.M. 1983. An analysis of the ground temperature and reflectivity pattern about St. Louis, Missouri, using HCMM satellite data. *Journal of Applied Meteorology*, 22, 566-571.

- Wald, L., Baleynaud, J.M. 1999. Observing air quality over the city of Nantes by means of Landsat thermal infrared data. *International Journal of Remote Sensing*, 20, 947– 959.
- Wan, Z., Li, Z.L. 1997. A physics-based algorithm for retrieving land-surface emissivity and temperature from EOS/MODIS data, *IEEE Transactions on Geoscience and Remote Sensing* 35: 4, 980–996.
- Watanabe, H., Bailey, B., Duda, K., Kannari, Y., Miura, A., Ramachandran, B. 2011. The ASTER Data System: An Overview of the Data Products in Japan and in the United States. In *Land Remote Sensing and Global Environmental Change*. Springer New York. 233-244.
- Weng, Q. 2001. A remote sensing-GIS evaluation of urban expansion and its impact on surface temperature in the Zhujiang Delta, China. *International Journal of Remote Sensing*, 22, 1999–2014.
- Weng, Q., Lu, D., Schubring, J. 2004. Estimation of land surface temperature–vegetation abundance relationship for urban heat island studies. *Remote Sensing of Environment*, 89: 4, 467–483.
- Wright, J. 1994. Accuracy of LOWTRAN 7 and MODTRAN in the 2.0-5.5  $\mu\text{m}$  Region. *Appl. Opt.*, 33, 1755.
- Xian, G., Crane, M. 2006. An analysis of urban thermal characteristics and association landcover in Tampa Bay and Las Vegas using Landsat satellite data, *Remote Sensing of Environment*, 104, 147–156.

### **Linking Chapters 2 and 3**

In Chapter 2, we provided a thorough literature review, describing the complexity of TIR imagery for studying the urban environment. The most notable challenges include the complex nature of urban surfaces, the influence of the atmosphere, microclimate variability, and the impact of emissivity on sensor observation. In an effort to resolve many of these issues, Chapter 3 describes a novel automated method to mitigate the variability within a TIR flight line caused by microclimate variability, the complex shape and orientation of urban features, and varying ground conditions such as slope and aspect. To achieve this, we consider urban roads as a pseudo invariant feature, spatially model its diverse temperature variability, and then remove this spatially variable difference from the original image. Testing is applied to three non-adjacent TABI-1800 airborne TIR flight lines ( $\sim 182 \text{ km}^2$ ).

## Chapter Three: Transforming image-objects into multiscale fields: A GEOBIA approach to mitigate urban microclimatic variability within H-res thermal infrared airborne flight lines<sup>16</sup>.

### 3.1 Abstract

In an effort to minimize complex urban microclimatic variability within high spatial resolution (H-res) airborne thermal infrared (TIR) flight lines, we describe the *Thermal Urban Road Normalization* (TURN) algorithm, which is based on the idea of *pseudo invariant features*. By assuming a homogeneous road temperature within a TIR scene, we hypothesize that any variation observed in road temperature is the effect of local microclimatic variability. To model microclimatic variability, we define a road-object class (road), compute the within-road temperature variability, sample it at different spatial intervals (10, 20, 50, and 100 m) then interpolate samples over each flight line to create an object-weighted variable temperature field (a *TURN-surface*). The optimal TURN-surface is then subtracted from the original TIR image, essentially creating a microclimate-free scene. Results at different sampling intervals are assessed based on their ability to visually and statistically reduce overall scene variability and computation speed. TURN is evaluated on three non-adjacent TABI-1800 flight lines (~182 km<sup>2</sup>) that were acquired in 2012 at midnight over The City of Calgary, Alberta, Canada. TURN also meets a recent GEOBIA (Geospatial Object Base Image Analysis) challenge to incorporate existing GIS vector objects within the GEOBIA workflow, rather than relying exclusively on segmentation methods.

**Keywords:** Thermal Urban Road Normalization (TURN), Surface Temperature, Temporal Variation, Microclimatic Variability, Thermal Infrared Imagery, Geographic Objects, TABI-1800.

---

<sup>16</sup> This work is co-authored by Rahman, M. M., Hay, G. J., Couloigner, I., and Hemachandaran, B. and has recently been accepted to a Special Issue (ISSN 2072-4292) of the open-source Journal 'Remote Sensing', titled *Advances in Geographic Object-Based Image Analysis (GEOBIA)*- Manuscript ID: remotesensing-60154

### 3.2 Introduction

*Thermal infrared (TIR)* remote sensing entails the acquisition, processing and analysis of remote sensing data acquired in the thermal infrared region (3 – 14  $\mu\text{m}$ ) of electromagnetic spectrum (Prakash, 2000). Currently, non-military TIR satellite sensors have moderate to low spatial resolution capabilities (e.g. 90 m ASTER, to 1.0 km NOAA-AVHRR). Consequently, studies using these data are typically limited to qualitative heat island analyses and rural-urban temperature comparisons (Kidder and Wu, 1987; Roth et al., 1989; Kim, 1992; Gallo and Owen, 1998; Streutker, 2002). Only recently, has the availability of high-spatial resolution (H-res) airborne imagery (e.g. ATLAS: 10 m, TIMS: 2 m, TABI: 0.5 m) made it possible to perform micro-scale thermal mapping of urban areas (Voogt and Oke, 1997; Quattrochi and Ridd, 1998; King et al., 2003; Gonzalez et al., 2005; Pu et al., 2006; Gluch et al., 2006; Hay et al., 2011, Rahman et al., 2013). Unfortunately, as the spatial resolution increases, the radiometric calibration of these images becomes ever more complex. This is increasingly apparent when:

- (i) Estimating true kinetic temperature from sensor observed radiant temperature (Voogt and Oak, 1997);
- (ii) Identifying atmospheric attenuation (Quattrochi and Luvall, 1999);
- (iii) Understanding and mitigating the influence of microclimatic variability (Hartz et al., 2006).

A *microclimate* is a local atmospheric zone where local climate differs from its surroundings. It may refer to areas as small as a few square meters (for example: a garden bed) or as large as many square kilometers (for example: a grassland). Microclimatic variability represents the climatic differences in the local environment, typically defined at fine spatial, temporal and thermal resolutions (Hartz et al., 2006). Thermal resolution is defined as the smallest temperature

difference that a TIR sensor is able to measure. Wind, precipitation and humidity are key microclimate components that influence thermal remote sensing. For example:

- (i) Surface winds increase convective heat loss from ground objects and help the ground surface to cool down (Santamouris et al., 2001),
- (ii) Precipitation forces objects to achieve a uniform temperature state (Giannini et al., 2003),  
and
- (iii) Increased relative humidity makes ground targets appear cooler than they would be under similar but drier conditions (Hartz et al., 2006).

As a result, objects composed of similar materials but placed in different microclimatic conditions typically exhibit different radiant temperatures. In the case of an urban surface, additional challenges are posed by the composite and heterogeneous nature of the surface itself, as well as the surrounding environment (Voogt and Oak, 2003). For example, as a part of the Heat Energy Assessment Technology (HEAT) project, Hay et al. (2011) explicitly noted the varying effects of microclimate on TIR imagery as well as the need to normalize for them when comparing urban rooftop temperatures.

A number of studies have addressed the impact of microclimate on TIR remote sensing. Friedl and Davis (1994) used TIR data from the NS001 Thematic Mapper Simulator (TMS) and helicopter-based multi-band radiometer measurements, in association with concurrent measurements of land surface energy balance components and limited in situ surface temperature measurements to identify sources of variation in radiometric surface temperature on mixed vegetation. They concluded that the amount of moisture significantly alters the radiant surface temperature, thus it needs to be accounted for in order to accurately estimate land surface fluxes. Lagourade et al. (2000) used a TIR camera (INFRAMETRICS Model 7601) placed aboard a small

aircraft and found that wind speed strongly influenced the remote measurement of surface brightness temperature. As a result, they only collected forest canopy thermal data under low wind conditions. Similarly, Crippen et al. (2007) found that when filling voids in SRTM digital elevation models using a night-time ASTER thermal dataset, microclimatic effects were one of the major sources of error in their TIR imagery, and that an abrupt deviation in surface temperature could be found even within a 100 m distance. This is notable, as the TIR spatial resolution of ASTER is 90 m, thus they were referring to an abrupt temperature variation over a single pixel.

Several researchers have attempted to develop models to mitigate the influence of microclimatic components on TIR imagery (Friedl and Davis, 1994, Voogt and Oak 2003). However, there are certain limitations to these models. In particular:

- (i) they primarily focus on a single microclimatic component, like wind speed, or humidity; thus they are unable to mitigate the integrated impact of microclimate components as a whole,
- (ii) they are developed for homogeneous vegetated, or sea surfaces – thus they are unable to handle the complexity of heterogeneous urban surfaces, and
- (iii) they are developed for moderate, to low-resolution imagery, which does not account for the fine details in H-res imagery.

WEIn an effort to overcome the limitations outlined from the literature, the objective of this paper is to develop an automated GEOBIA method to mitigate the integrated influence of local microclimatic variability within a multi-flight line H-res airborne thermal infrared scene. The geospatial object-based image analysis (GEOBIA) paradigm allows a user to integrate a broad spectrum of different object features such as size, shape, tone, pattern, association, and texture into the analysis process (Blaschke et al., 2014). With the advancement of digital cartography and GIS

technology, semi-automated and automated methods of object-based image analysis are becoming an important component in the remote sensing image analyst's tool kit, which places the emphasis on geographic objects rather than cells (Hay and Castilla, 2008).

To provide a GEOBIA solution to mitigate the microclimatic impact on TIR imagery, we introduce a unique method referred to as *Thermal Urban Road Normalization* (TURN) and test it on three non-adjacent TABI-1800 flight lines. A TURN adjusted flight line is expected to display more consistent temperatures within the flight line so that similar objects can be better classified, compared and assessed. In order to fully evaluate TURN, the proceeding sections describe the study area and dataset (Section 3.3), followed by a detailed explanation of how TURN is developed (Section 3.4) and applied (Section 3.5). This is then followed by the results and a discussion of the operational considerations and lessons learned (Section 3.6).

### **3.3 Study area and dataset**

Our study area consists of three non-adjacent H-res TIR flight lines (~182 km<sup>2</sup>) that were extracted for analysis from a full City of Calgary TABI-1800 (Thermal Airborne Broadband Imager) dataset (~825 km<sup>2</sup>) composed of 43 flight lines (Figure 3-1). These three flight lines were acquired during the night (between 00:00 to 04:30) on May 13, 2012 at a 50 cm spatial resolution. During their acquisition, the ambient night-time temperature<sup>17</sup> ranged from 8-13°C (measured from the ground) and winds ranged from 5-13 km/hr., gusting to 20 km (measured from ground stations).

---

<sup>17</sup> Local weather data were accessed from 26 reporting sites available from the Weather Underground <http://www.wunderground.com> - last accessed June 06, 2014.

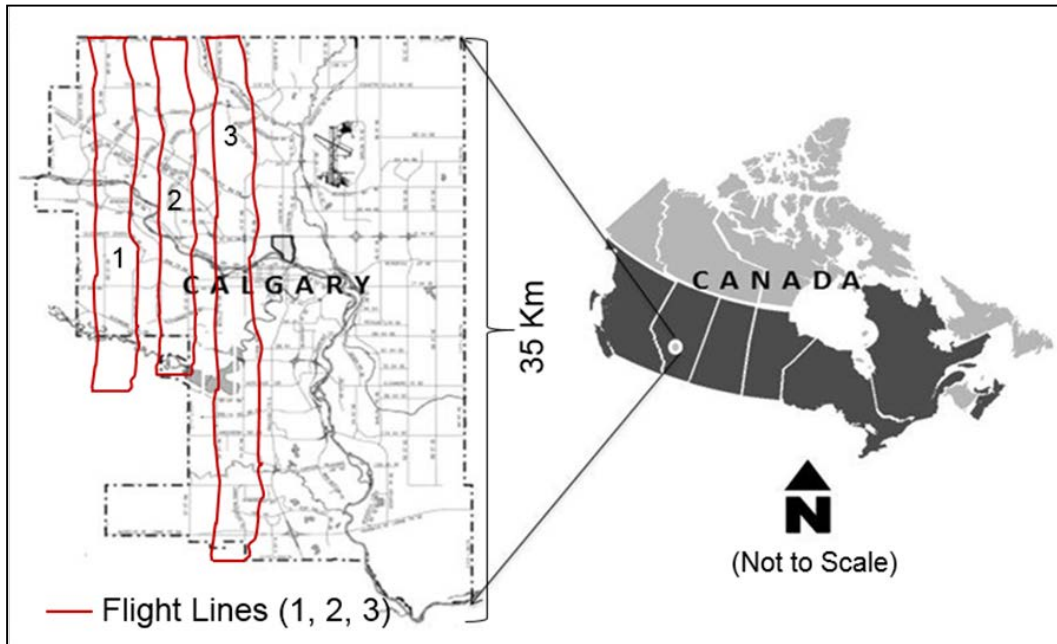


**Figure 3-1: Map of The City of Calgary showing the location of the flight lines evaluated in this study.**

The TABI-1800 is a recent airborne thermal infrared sensor (circa 2012) with a swath width of 1,800 pixels in the 3.7 - 4.8  $\mu\text{m}$  spectral region, a thermal resolution of  $0.05^{\circ}\text{C}$ , and the ability to collect up to  $175 \text{ km}^2$  per hour at 1.0 m spatial resolution (ITRES, 2013). This is three to five times faster than most other airborne TIR sensors (Hay et al., 2011). All the flight lines were orthorectified by the service provider (ITRES Research LTD) using a 10 m digital elevation model (DEM), and the reported geometric accuracy of the dataset was  $\pm 1$  meter. The City of Calgary also provided an RGB-NIR<sup>18</sup> orthorectified airphoto-mosaic (acquired in 2012, at a 25 cm spatial resolution, geometric accuracy  $\pm 25$  cm) and a GIS road dataset (geometric accuracy  $\pm 25$  cm) – composed of polylines that represent road centers. The TABI data were resampled to 1.0 m using bilinear interpolation. Similarly, the City ortho-mosaic was resampled to a 1.0 m spatial resolution

---

<sup>18</sup> RGB-NIR : Red, Green, Blue, Near Infra-red

using cubic-convolution (CC). This was based on visual results and the fact that CC models a 4x4 pixel area, which corresponds nicely to resampling the scene from 25 cm to 1.0 m.

### **3.4 Methods**

In the proceeding section, we describe TURN (the method) applied only to a single flight line of TABI-1800 data. Once this entire process has been described, we then repeat the method (Sections 3.4.2 - 3.4.6) on the remaining two non-adjacent flight lines and present the results of all three flight lines in the Results and Discussion sections. This is to minimize repetition in the Methods section and to illustrate that TURN can be applied to independently collected H-res TIR flight lines of different data-volumes and acquisition times.

#### ***3.4.1 Pseudo invariant features and mode road temperature***

To develop the Thermal Urban Road Normalization (TURN) method, objects (roads) are considered as pseudo invariant features. This is because: (i) roads are relatively well distributed over modern urban environments, (ii) their primary construction materials are generally the same for each major road type within a given city, thus providing consistent thermal properties, and (iii) previous research has revealed a strong correlation between air temperature and road surface temperature (Bogren and Gustavson, 1991; Gustavsson, 1995), from which we assume that the road temperature can be used to model urban microclimatic variability in terms of energy flux.

As the TIR images were acquired late at night, any variation from the (mode) road temperature within a flight line is considered the result of local microclimatic variability. Based on these conditions, the TURN method consists of extracting an object road class from a TIR flight line, calculating its deviation (see section 3.4.5 for details), and interpolating it over the entire TIR flight line to create a temperature variability surface. This surface can then be used to minimize the impact of microclimate variability on other object classes present in the TIR flight line. We

Object/shape based interpolation techniques are commonly used in medical image processing to fill voids in an image (Herman et al., 1992; Grevera et al., 1996; Bors et al., 2002). Building on these ideas, we use similar techniques to create a continuous, smooth microclimatic variability map. Figure 3-2 briefly outlines this methodology, which is further described in detail in the following sections (3.4.2-3.4.6).

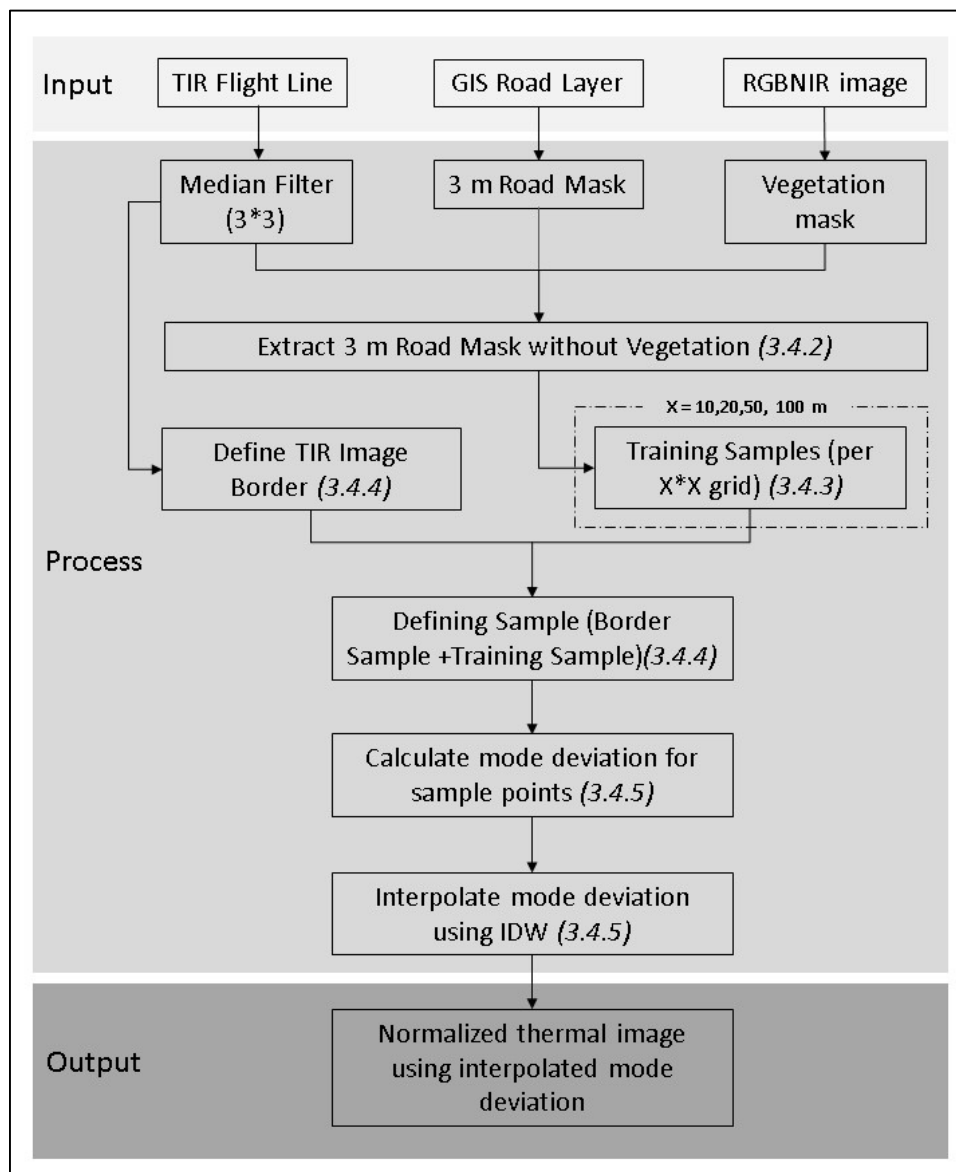


**Figure 3-2: This methodology flow chart describes the main steps for normalizing a thermal flight line using the TURN method. The italic numbers in parenthesis indicate the sections where details are provided.**

### ***3.4.2 Road extraction***

A global road class is extracted from the TIR flight line based on The City of Calgary vector road data. These data represent the road centerlines of four different road types: (i) primary, (ii) secondary, (iii) access, and (iv) back-alleys. In this study, only primary and secondary roads are considered. Back-alleys and access roads are omitted as they are typically covered by trees, and are composed of numerous mixed materials (e.g., gravel, clay, brick, asphalt, cement and others), many of which have very different thermal characteristic and emissivity values.

To extract the road class, we first apply a 3x3 median filter to the TIR image to smooth the signal, which aids in delineation. We then create a 1.5 m buffer on each side of the road center (Figure 3-3A) to produce a 3.0 m wide road mask (Figure 3-3B). This is combined with the TIR image to extract the central portions of the corresponding roads. A visual inspection reveals that portions of many roads are covered by trees (Figure 3-3C). To eliminate these trees, a vegetation mask (Figure 3-3D) is created by generating an NDVI (from the RGB-NIR ortho-photo), then manually thresholding a general vegetation class based on visual inspection. Once defined, this vegetation mask is then dilated by 1.0 m to compensate for possible geometric misalignment between the RGB-NIR and the TIR images. This dilated vegetation mask is then applied to the 3.0 m road class to eliminate overhanging vegetation (Figure 3-3E).

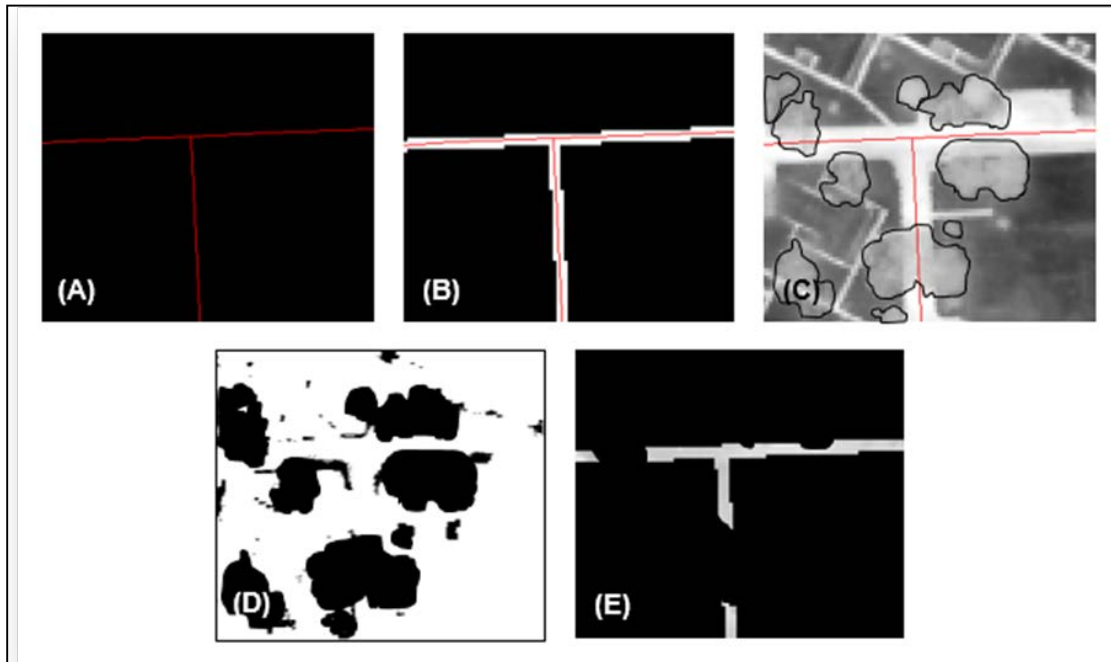


**Figure 3-3: An example of the road extraction technique. (A) The vector road layer (red). (B) The 1.5 m buffer created on both sides of the road center (road mask in white). (C) The TIR image showing dark tones as cool objects and bright tones as hot objects. Vegetation is delineated with black polygons (for illustration only) and the road center as a red line. (D) The dilated vegetation mask created from an NDVI image where black areas represent vegetation. (E) A ‘vegetation-free’ 3.0 m wide TIR road mask filled with thermal DNs.**

Next, a histogram of the extracted road class (Figure 3-4A) is created to visually and statistically assess any remaining road temperature noise. Here noise refers to pixels that are not representative of the road class. From Figure 3-4A, the histogram has a bimodal distribution. When linked to the corresponding thermal flight line, it was possible to determine that the left distribution is primarily representative of gravel roads, road construction, and vehicles, which is denoted as noise (Figure 3-4B). In an effort to automate the process of reducing this noise, we examined many different combinations of mean ( $\mu$ ) and standard deviation ( $\sigma$ ) (derived from each flight line) to determine an optimum range of noise DNs. Analysis revealed that a range of  $(\mu - 2\sigma)$  to  $(\mu + 3\sigma)$  best represents the road class with minimal noise. Consequently, the DNs beyond this range (the noise) were masked out, and the remaining road pixels were used for further processing. This noise

minimizing technique was evaluated on all three flight lines separately and was observed to work well on each of them.

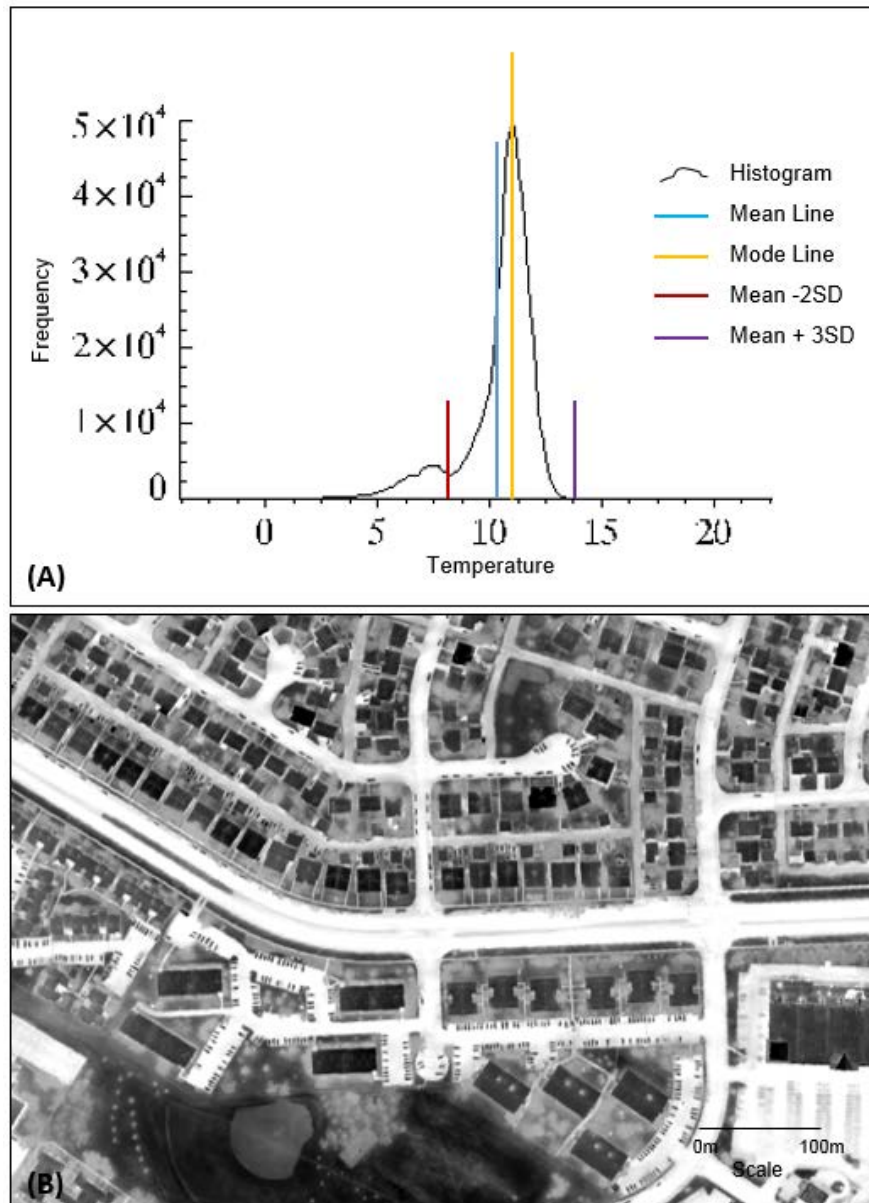


**Figure 3-4: (A) Histogram of flight line 1 showing a bimodal distribution, where the left distribution represents noise (i.e. road construction and vehicles) and the right distribution represents the road class. (B) A portion of the raw TIR image displaying roads, rooftops, trees, grass, parked vehicles and back alleys. Dark areas are cool, bright areas are warm.**

### ***3.4.3 Multi interval sampling***

Of all the *Road* pixels defined in Section 3.4.2, 0.5% of each flight line (totaling ~1800-2400 pixels, depending on the size of the flight line) are randomly selected and saved as a test dataset for accuracy assessment (Figure 3-5A-C). The remaining road pixels (95.5%) are used for analysis.

At 1.0 m spatial resolution, a 3.0 m wide section of the road mask (Figure 3-5A) distributed over each flight line contains many spatially adjacent and spectrally similar pixels, making spatial interpolation challenging. Furthermore, due to the varying size, shape and orientation of road objects, it is not possible to determine an optimal sample interval using statistical autocorrelation. To simplify this interpolation problem, we divide the entire flight line into  $X \times X$  m grid cells ( $X = 10, 20, 50, \text{ and } 100$  m) and select one representative road pixel from each cell (which is the median of all sampled road pixels within each cell). The median is selected rather than mode, as it is possible that all samples are unique. We also retain each median road DN at its actual sampled location, rather than arbitrarily placing it at the center of an  $X \times X$  cell - as the cell center may be located far from the road. These road samples (Figure 3-5C) are then used for further processing. We evaluate this sampling technique at four different sampling intervals ( $X = 10, 20, 50, \text{ and } 100$  m) to determine the optimum sampling strategy.

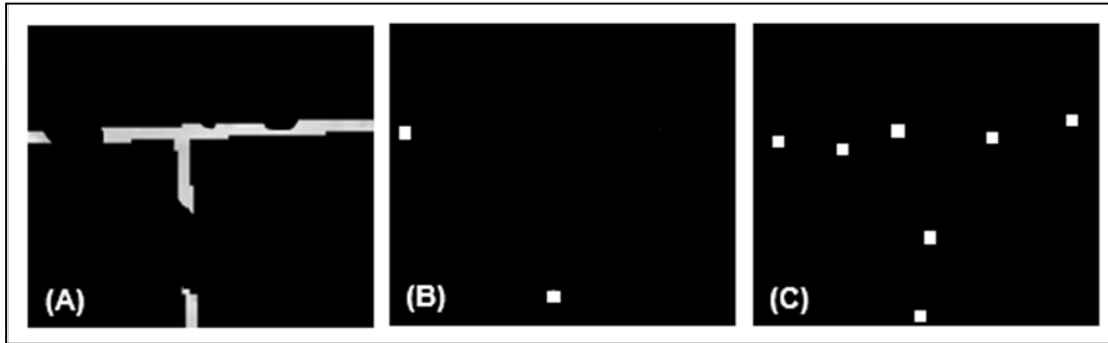


**Figure 3-5: An example of road training and test samples. (A) An example of a 3.0 m wide road mask. (B) An example of the test pixels derived from the road shown in 3-5A. (C) An example of the extracted training pixels (one sample per 10m\*10m grid).**

#### **3.4.4 Sampling optimization: borders and oversampling**

Airborne data are seldom acquired in perfect straight lines. Consequently, the border of such data is often padded with zero values to ensure a rectangular shape of the output flight line (Figure 3-6A). To tie the interpolated TURN surface to this edge, its boundary is detected using a *Laplacian edge detection filter* (Figure 3-6B), and sample points are taken along the border at 10 m intervals<sup>19</sup> (Figure 3-6C). For parsimony, these border samples are then assigned the values of the closest road sample (Figure 3-6D) and are combined with the samples generated in step 3.4.3 (Figure 3-6E). Next, a *cleaning filter* is run over all flight line samples so that there is a maximum of one sample point within a 10\*10 m window (Figure 3-6F). Cleaning is performed to avoid oversampling of points. The remaining sample points are then interpolated to create a (continuous) road temperature variability surface over the entire flight line.

---

<sup>19</sup> In this section we describe the sampling optimization technique at 10 m intervals. Later, the same process is repeated for 20, 50, and 100 m intervals and results are described in Section 4.

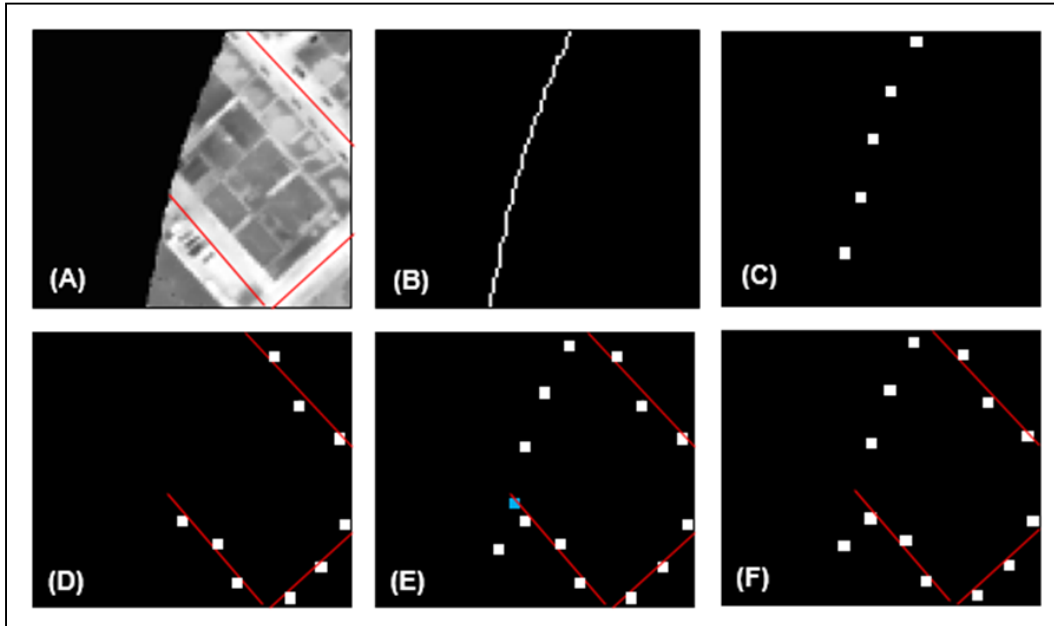


**Figure 3-6: An example of selecting sample points from the image border, then cleaning of these points to reduce oversampling. (A) A portion of the thermal flight line (grayscale) showing the acquisition border (black) and road center line (red). (B) A corresponding portion of the borderline detected using edge detection. (C) Sample points taken along the border at a 10 m interval. (D) Road samples (white) with the road center (red). (E) Border samples from (3-6C) combined with the road samples. The blue square (lower center) represents a sample location to be cleaned. (F) Final sample points after cleaning.**

### ***3.4.5 Spatial interpolation of road temperature variations***

The objective is to interpolate road temperature deviation as a smooth and continuous surface for each flight line. Conceptually, this surface represents variation in land surface temperature within a flight line due to the nonlinear interaction of local microclimatic components (i.e. wind, precipitation, and humidity). To create this surface, we first calculate the mode road temperature from the road class generated in step 3.3.2. From a statistical perspective, we consider the mode of the road temperature samples of a TIR flight line as the most representative temperature of all roads (rather than the average) as it occurs most frequently throughout the flight line; thus it is the most ‘road-like’. We then collect TIR road training samples (steps 3.3.3-3.3.4), and then, for each sample point we calculate the local mode deviation ( $D_{ij}$ ) using Equation 3-1.

These mode deviation values are then interpolated over the entire flight line using *Inverse Distance Weighting* (IDW) (Franke, 1982). Specific interpolation parameters includes: (i) Maximum search radius = 100 m, (ii) Minimum number of closest points used for each local fit = 3, and (iii) Smoothing radius = 10 m.

$$D_{ij} = (X_{ij} - X) / X_{ij} \quad (\text{Equation 3-1})$$

Where,

$D_{ij}$  = Mode deviation at pixel (i, j)

$X_{ij}$  = Radiant temperature of pixel (i, j)

$X$  = Mode Road temperature for a given flight line

Prior to selecting IDW, seven different interpolation techniques were visually and statistically evaluated. These included: (i) Splines (Franke, 1982), (ii) Nearest Neighborhood (Parker et al., 1983), (iii) Polynomial (De-Boor, 1978), (iv) Kriging (Isaaks and Srivastava, 1989), (v) Inverse Distance Weighting (IDW), (vi) Triangular Integrated Network (TIN) (Renka, 1984), and (vii) Radial Basis Function (RBF) (Franke, 1979). Based on visual and statistical assessment of the resulting surfaces, IDW was shown to produce the smoothest appearing surface based on locally varying values, which is consistent with the conceptual models of locally explicit, but regionally continuous microclimatic variability (Bogren and Gustavsson, 1991; Friedl and Davis, 1994). Therefore, we have used IDW interpolation for the remainder of this analysis.

We then consider the interpolated deviation surface to represent temperature differences in a flight line resulting from local microclimatic variations. Conceptually, this surface can be used to normalize the contribution of microclimate from the original thermal flight line using Equation 3-2, where the interpolated variability map is simply subtracted from the thermal flight line.

$$N_{ij} = X_{ij} - D_{ij} \quad (\text{Equation 3-2})$$

Where,

$N_{ij}$  = Normalized radiant temperature of pixel  $(i, j)$

$D_{ij}$  = Mode deviation at pixel  $(i, j)$

$X_{ij}$  = Original radiant temperature of pixel  $(i, j)$

### **3.4.6 Validation of the model**

Once the original flight lines are normalized for microclimatic variability using road temperature deviation, an accuracy assessment is performed to evaluate the performance of the model. It is expected that the radiant road temperatures over an entire flight line will be equal to the mode road temperature after applying TURN. To verify this, the temperature of the test road pixels (step 3.4.3) before and after normalization were compared using the *Root Mean Square Error* (RMSE) which is calculated using equation 3-3.

$$RMSE = \sqrt{\frac{\sum_1^n (X - X_{ij})^2}{n}} \quad (\text{Equation 3-3})$$

Where,

$X$  = mode road temperature of a flight line

$X_{ij}$  = road temperature of pixel  $(i,j)$

$N$  = number of total test pixels

In this experiment, the RMSE essentially describes how the radiometric variability of similar objects (i.e. samples derived from a ‘homogeneous’ road class) change after applying TURN. Lower RMSE values represent more ‘object-like’ results, thus our goal is to obtain a lower RMSE result for the same (road) class. This is because image-objects by definition (Castilla and Hay, 2008) tend to be composed of similar components (i.e. pixels with similar DN values), thus they have lower internal variability.

### 3.5 Results and discussions

The Methods section described TURN applied to a single TIR flight line with a 10 m sampling interval. In this section we describe and discuss the results of the same method independently applied to all three thermal flight lines (as shown in Figure 3-1) over four different sampling intervals (10, 20, 50, and 100 m). Table 3-1 outlines the size of the flight lines, the number of training samples for each sampling interval, and the number of test pixels used for accuracy assessment.

**Table 3-1: Training and test sample sizes of the evaluated flight lines for different sampling intervals.**

Scene Attributes		Flight line 1	Flight line 2	Flight line 3
Size (pixels)		2283*22680	1853*22318	2451*36260
Training Samples	10 m	20252	20884	27854
	20 m	13855	14433	19069
	50 m	4889	5098	6671
	100 m	1763	1853	2423
Test Samples (total)		1792	1874	2462

The following sections (3.5.1 – 3.5.4) discuss and compare the results achieved from these flight lines at different sampling intervals. Section 3.5.5 discusses operation considerations, and 3.5.6 discusses the importance of incorporating existing GIS image-objects into the GEOBIA workflow.

#### 3.5.1 Sample size vs. processing time

As automation and operationalization of the TURN model are important goals of this research, we compared the processing speeds for collecting and interpolating samples at different sampling intervals for different sized flight lines. To do so, we ran TURN with the same

workstation<sup>20</sup> on each of the three flight lines for four different sampling intervals. TURN code is written in Interactive Data Language (IDL 8.0, 64 bit version<sup>21</sup>). Figure 3-7 and Table 3-1 show that as the road sample interval (i.e. distance between adjacent samples) for each flight line decreases, the number of samples and the required processing time increases.

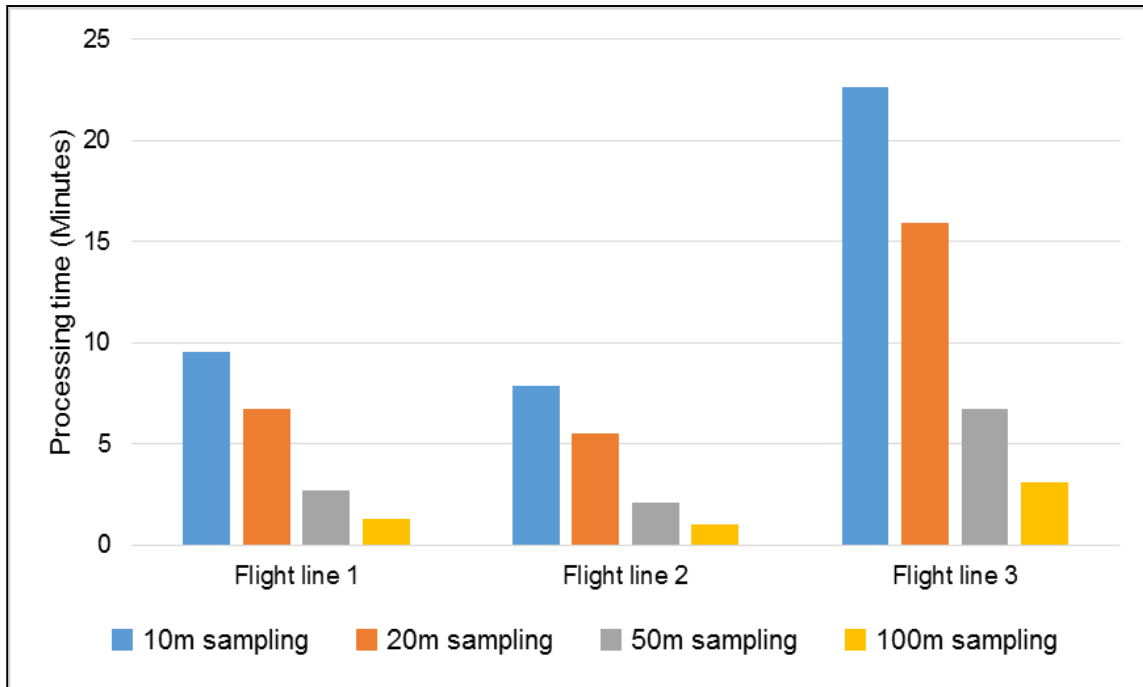


**Figure 3-7: A comparison of CPU processing time for four different sampling intervals (10, 20, 50, and 100 m) for each of the three different flight lines. Time differences between flight lines are due to differences in data volumes/flight line. Time differences within flight lines are due to the size of the sample to be processed.**

To process The entire City of Calgary TIR scene (which consists of 43 TABI-1800 flight lines ~ 825 km<sup>2</sup>), it will require ~7 hours for the 10 m sampling interval, ~5 hours for the 20 m sampling interval, ~2.5 hours for the 50 m sampling interval, and ~1.2 hours for the 100 m sampling interval. Thus, the processing time is negatively correlated with the sampling interval

<sup>20</sup> Intel® Core™ i7-2600, Windows Server 2008 (64 bit) on a Quad Core CPU at 3.40GHz, RAM: 16 GB

<sup>21</sup> <http://www.exelisvis.com>

(i.e. the larger the sampling interval, the less processing time involved). Flight line 3 requires considerably more processing time than the other flight lines, as it is ~50% larger (in size) than the other two flight lines (see Table 3-1 and Figure 3-1).

### ***3.5.2 A comparison of radiometric normalization accuracy based on RMSE***

We consider the mode road temperature of each independent flight line as its reference temperature, and radiometrically normalize the thermal flight line to this mode as it represents the most abundant temperature within the flight line. Therefore, after normalization, road temperatures within a flight line should shift to its mode temperature. To test this hypothesis, we randomly selected a number of road test pixels from the original flight lines (see Table 3-1) and evaluated their RMSE with corresponding samples from the normalized mode road temperature scenes, to determine their radiometric similarity (in °C). Conceptually, the smaller the RMSE, the closer the road temperature is to the mode road temperature, meaning that the effects of microclimate are increasingly normalized.

In order to best illustrate the effects of all four different sample intervals on each of the 3 flight lines, Figure 3-8 shows the percent decrease in RMSE - where larger values are better. This is because they represent a greater reduction in RMSE between the original image and the normalized image. In all cases, the RMSE decreases after normalization, thus the road temperatures are becoming more consistent across the scene, as per our initial hypothesis. However, the normalized test pixels are closest to the mode road temperature for TURN-surfaces generated from small sampling intervals. This means that greater overall similarity is achieved for smaller sample sizes; though statistically, there is only ~2-3% difference between the 10 m, 20 m and 50 m sample intervals. In contrast, the 100 m sample shows a notable decrease (4-7%) in

RMSE compared to the 10 m sample, indicating that microclimatic variability is less well (statistically) modeled at this coarser sampling interval.

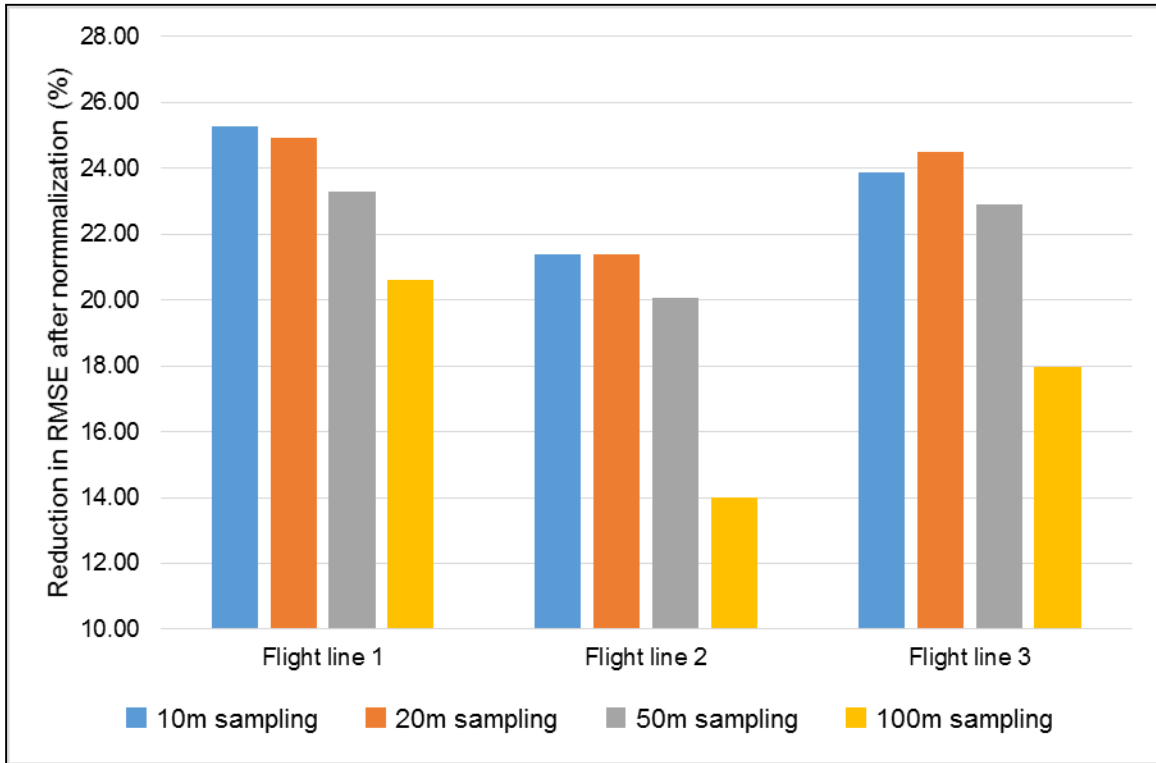


**Figure 3-8: The percent (%) decrease in RMSE of three evaluated flight lines after radiometric normalization at four different sampling intervals (larger RMSE values are better).**

### ***3.5.3 Root mean square error (RMSE) vs. processing time***

Considering the fact that TURN is developed for large-area high-spatial resolution (1.0 m) TIR imagery, processing needs to be fast while also maintaining a strong reduction in RMSE. To compare accuracy (RMSE) vs. processing time, Figure 3-9 shows the mean decrease in RMSE and mean processing time for each flight line and sampling interval.

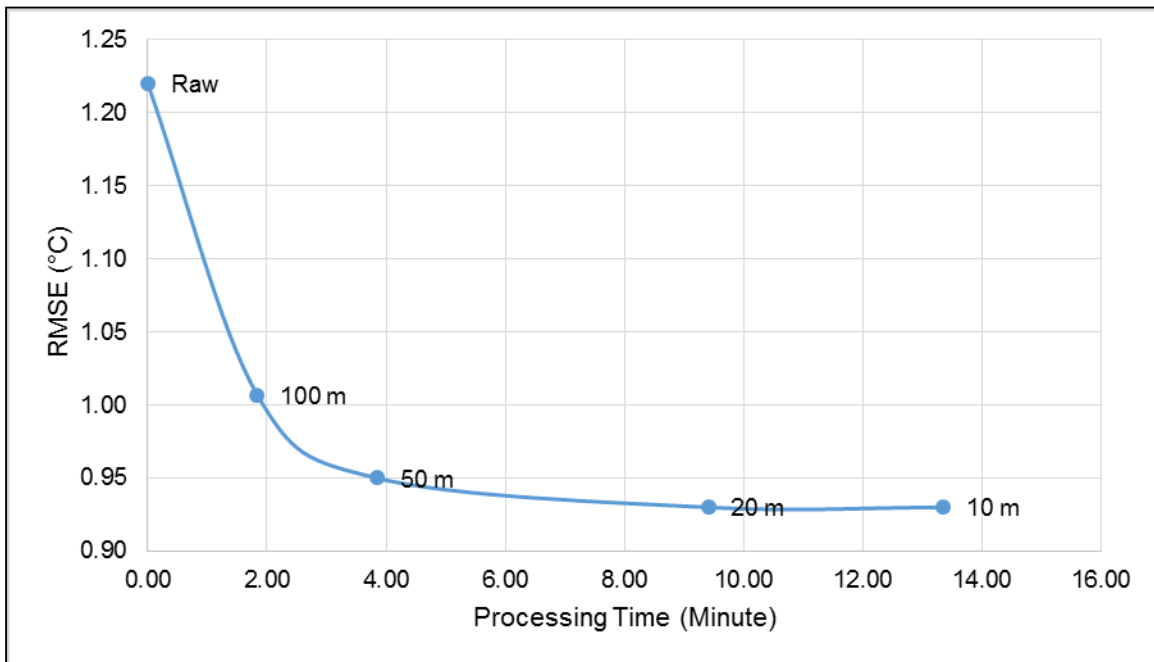


**Figure 3-9: A comparison of average radiometric accuracy vs. average processing time for 3 flight lines at four different sample intervals.**

As the sampling interval decreases, the accuracy increases (thus the RMSE gets smaller), but the processing time also increases. However, between the 10 m and 20 m sample intervals, processing time decreased by ~30%, but average accuracy did not notably change. Conversely, the processing time for the 100 m sample interval is ~85% less than at the 10 m sampling interval. However, its average accuracy is considerably decreased (~10%). Considering these results, we conclude that 20 m is the optimum sample interval for this study, as it balances local temperature variability (Figure 3-10) and computation speed.

#### ***3.5.4 Visual assessment of the interpolated surface at different sampling intervals***

TURN generates an interpolated surface representing the road temperature deviations within a flight line. Figure 3-10 provides an example of how microclimate variability is visually represented by the *TURN-surface* at different sampling intervals.

The flight line sample in Figure 3-10A represents two main vegetated areas (one at the top and another at the middle of the figure) surrounded by roads and buildings. Detailed visual inspection shows that the vegetated areas are cooler than the built-up areas, making the adjacent roads appear cooler (dark grey) than the mode road temperature, thus, requiring a positive temperature adjustment (see the light grey surfaces at the top and middle of 3-10 B). Figure 3-10 (B-C) shows that the thermal characteristics of different landcover types are visually represented in greater detail with 10 m and 20 m sampling intervals. At the 50 m sampling interval (Figure 3-10 D), the surface is more generalized, but still sufficient to distinguish different types of landcover (compared with 3-10 A). However, at the 100 m sampling interval (Figure 3-10 E), a larger portion of the corresponding land surface temperature detail is lost through generalization. Given these unique perspectives, TURN-surfaces may also represent useful tools for urban planners to identify potential urban heat sinks, and localized sources of urban heat islands.

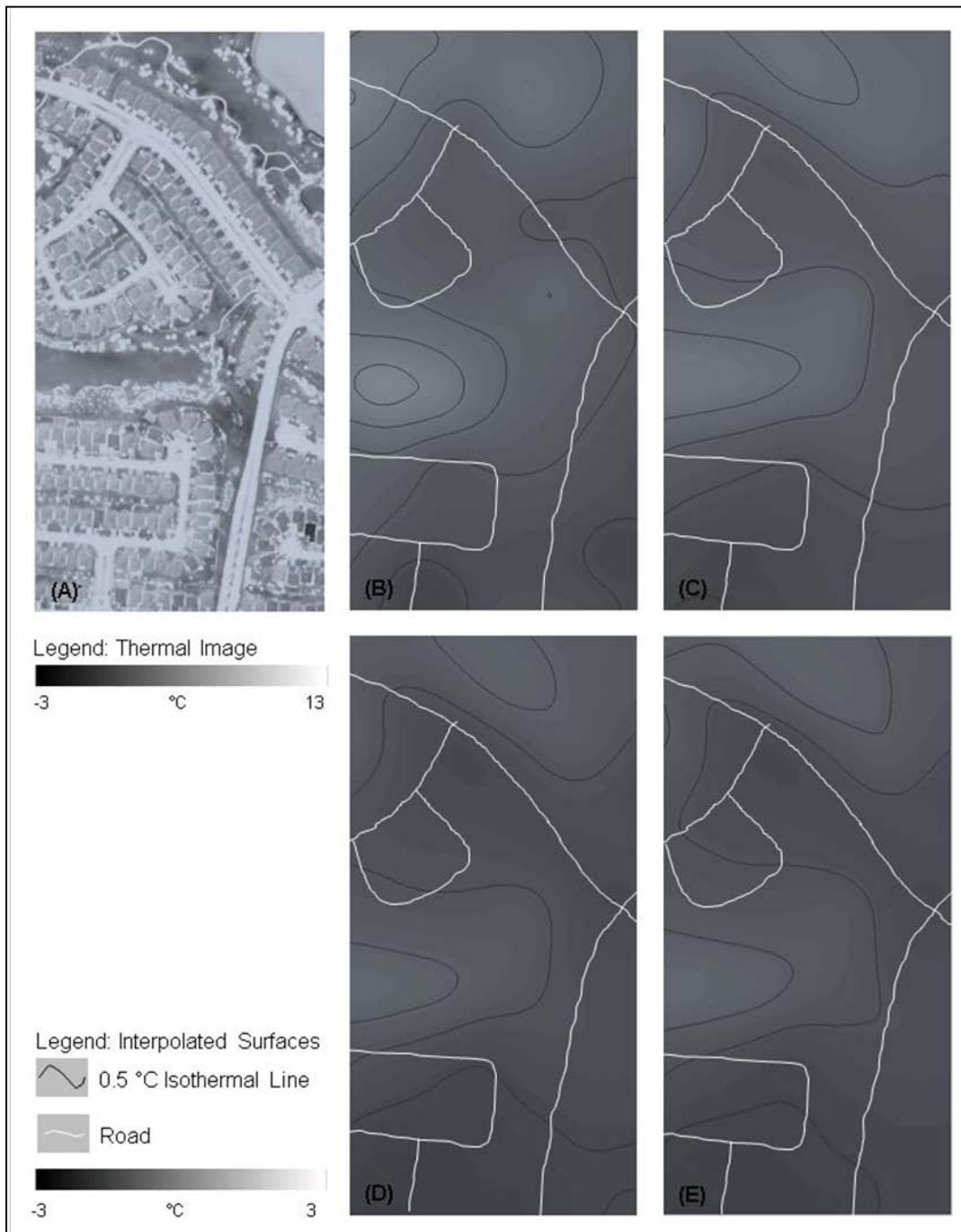


**Figure 3-10: In this figure (A) shows a portion of the original TIR flight line displaying typical landcover (buildings, roads, grass). (B-E) illustrates four interpolated TURN surfaces that represent continuous urban microclimate temperature variability surfaces (°C), derived from local TIR road-objects, at four different sampling intervals: (B) 10 m, (C) 20 m, (D) 50 m, and (E) 100 m. Roads are in white, and isotherms are dark lines representing 0.5 °C intervals.**

The final output of the proposed model is a flight line free from the effects of microclimate, thus displaying a more uniform radiometric response of similar objects within it. Figure 3-11 shows an example of how radiometric difference among similar objects decreases after applying TURN. Figure 3-11(A) represents a portion of the raw flight line displaying rooftop, road, grass, etc., 3-11(B) represents the TURN-surface created using 10 m sampling interval, and 3-11(C) represents the normalized portion of the flight line using TURN-surface. Rooftops in the raw image (3-11A) are represented by different shades of blue and green, indicating that there is a notable variation in rooftop temperature. However, once TURN is applied (3-11C), the rooftops visually appear more consistent (green).

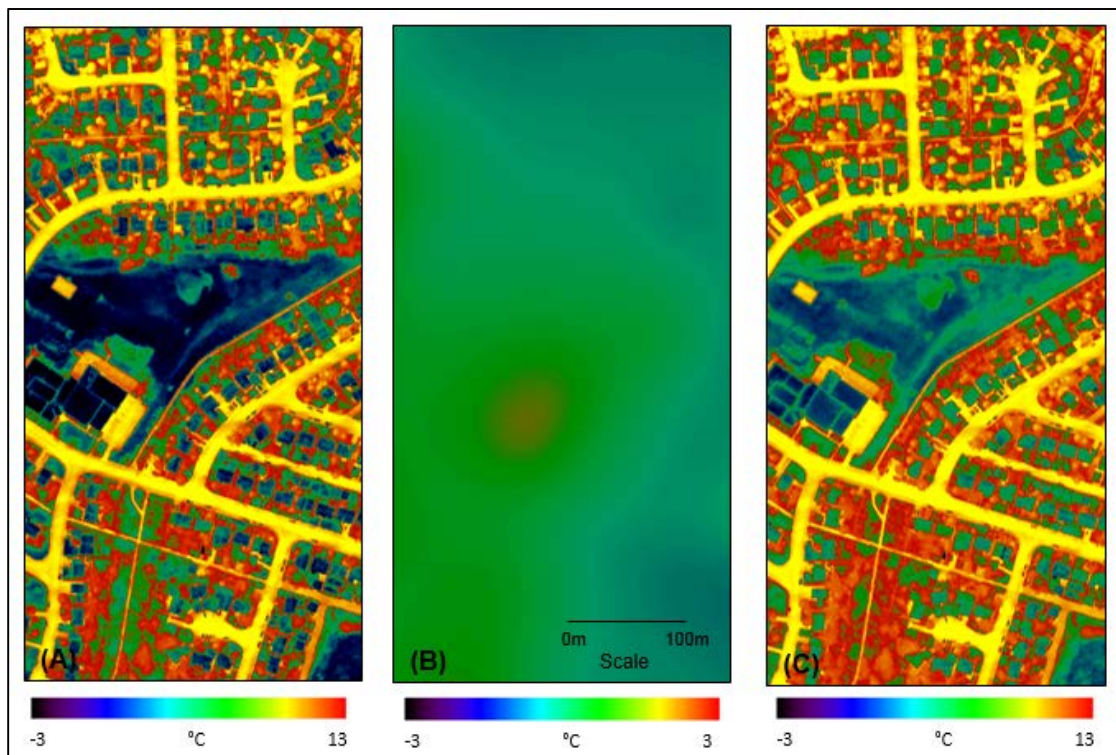


**Figure 3-111: An example of radiometric normalization using TURN. (A) A portion of the raw TABI-1800 image. (B) A TURN-surface (i.e. an interpolated road temperature deviation surface) of the same area. (C) An image of the same area after applying the TURN-surface.**

### ***3.5.5 Operational considerations, errors and uncertainties***

This section briefly discusses three important operational considerations, errors and uncertainties about TURN.

#### **3.5.5.1 Mitigating microclimate and surface effects**

When acquiring TIR airborne imagery, ideally winds should be lower than 5-10 km/hr. and ambient temperature lower than 7°C so as to provide sufficient environmental contrast (Hay, 2014). However, weather is dynamic, and even the best planned acquisitions need to deal with the often changing meteorological conditions they are presented with. This in part is why TURN was conceived, and why it is expected to become an important contribution to the TIR community. Given sufficient spatial and temperature resolution to define appropriate road samples, the TURN method is able to visually and statistically mitigate the *integrated impact* of microclimatic and atmospheric variability and other physical surface conditions such as elevation, slope, aspect etc. that externally influence TIR radiometry acquired from H-res TIR platforms. This is because the temperatures derived from local road samples already represent an integration of these environmental conditions. As noted in Section 3-2, we do have access to temperature data from 26 meteorological stations during the TIR acquisition time. However, for a large city like Calgary (~43 TABI-1800 TIR flight lines), we suggest that 26 stations is simply too coarse to validate microclimatic variability, which occurs within 1-100 meters. To do so, would require setting up ~ 40 - 60 meteorological stations (1 every km<sup>2</sup>) within each flight line, and ~800-1000 stations for the whole city, which is beyond the scope of this study.

#### **3.5.5.2 Road invariance**

TURN is based on the assumption that roads of the same material are radiometrically invariant. In reality, roads are not completely invariant due to their different material types and

surface conditions resulting from age, traffic load, exposure to solar radiation, geographic location, etc. (Junhui and Jianqiang, 2010). However, this is also true for all other pseudo-invariant features (Schott et al., 1988). Conceptually, this situation can only be avoided by manually acquiring numerous samples of the temperature of invariant materials over the entire study area immediately prior to TIR data collection (to allow for them to reach thermal equilibrium with the environment), which is impractical for large study areas.

### 3.5.5.3 Emissivity correction

The evaluated flight lines represent the radiant temperatures of different landcover. Thus, road extraction and interpolation are also performed based on radiant temperatures. For kinetic microclimate temperature corrections, emissivity corrected road samples need to be interpolated and applied to an emissivity corrected surface. For example, Nichol (2009) proposed the *Emissivity Modulation* (EM) technique (similar to image sharpening described by Gustavson et al., 2003) to correct thermal images for different emissivity classes. EM uses a geographically corrected optical image to classify different landcover classes. The corresponding emissivity class values are then integrated with the thermal image to calculate kinetic temperature. Based on this idea, we suggest that EM along with TURN can be used to produce an emissivity corrected and microclimate normalized TIR flight line that represents the true kinetic temperature of the landcover-types of interest.

### 3.5.6 Transforming existing vector image-objects into multiscale fields

Bain (2007) notes three main categories of geographic space - spatial objects, regions, and fields – and that fields are not well represented by objects. However, to the best of our knowledge, this is the first time in the literature, that discrete image-objects are transformed into a continuously varying multiscale field. To do so, we initially define roads by buffering around an existing City

of Calgary GIS polyline that represents road centers. Thus, we do not actually apply segmentation to the initial road objects (though we do apply thresholding to an NDVI image to remove vegetation objects that overhang/obscure these new road-objects). In this sense, TURN is a step towards meeting the recent challenge to the GEOBIA community (Hay, 2014) to incorporate existing GIS vector objects within the GEOBIA workflow, rather than rely solely on segmentation methods that have no unique solution (Hay and Castilla, 2008).

### 3.6 Conclusions

Local microclimatic components such as wind, humidity, precipitation and surface moisture have a non-linear impact on TIR imaging, making detailed analysis non-trivial. To mitigate these effects, we describe *Thermal Urban Road Normalization* (TURN) applied to three non-adjacent flight lines of H-res TABI-1800 imagery (~182 km<sup>2</sup>), that cover a complex urban scene. TURN is a new method that radiometrically normalizes TIR flight lines so that it appears as if the entire scene were acquired under the same microclimate conditions and at the same time. In this method, roads within the scene are considered as a *pseudo invariant feature* from which (environmentally integrated) temperature samples are defined and interpolated. Road samples are used as a reference object-class for two reasons: (i) road material is generally constant within a city, and (ii) roads are relatively evenly distributed over urban areas – thus providing a sufficient number of evenly distributed samples from which to create a continuous interpolated *TURN-surface*. This TURN-surface is a continuous temperature variability map, that models (i) the integrated effects of microclimatic variability over the entire TIR scene, and (we also suggest), (ii) location-based characteristics such as elevation, slope and aspect, and (iii) atmospheric variability, as these characteristics are already integrated within the extracted TIR samples.

Prior to interpolation, eight different spatial interpolation techniques were evaluated, which showed that *Inverse Distance Weighting* (IDW) produced the most representative surface, as it specifically models the influence of local variability. The resulting TURN-surface is then used to normalize the original TIR flight line by removing the varying effects of local microclimate.

In total, radiometric normalization was performed on three non-adjacent flight lines at four different sample intervals (10 m, 20 m, 50 m, and 100 m). Results show that this method is able to reduce internal road temperature variability by ~25% at 10 m and 20 m sampling interval, ~19% at 50 m sampling interval, and ~15% at 100 m sampling interval. As the sample interval decreased, the accuracy increased (i.e. the internal variability of similar features within a thermal flight line decreased); however, the processing time also increased. From the combined results of reduced within-scene variability and computational speed, we conclude that 20 m is the optimum sampling scheme to generate a TURN-surface, as: (i) processing time was reduced by ~25% (compared to that at 10 m), (ii) the radiometric normalization accuracy (RMSE) changed very little compared to results achieved at 10 m, and (iii) the 20 m temperature variability map showed very similar radiometric detail to that of 10 m. However, this conclusion is made based on the results of this study - for other study area a different sampling strategy may be better suited.

The challenge of using this method remains in considering roads as pseudo invariant features, as the radiometry of roads varies depending upon material composition, age, surface condition, orientation and the surrounding environment, thus a user should take extra care while selecting appropriate roads. Another uncertainty of this method is posed by limited field data to validate the model at fine resolution.

In summary, the Thermal Urban Road Normalization (TURN) method enables the generation of radiometrically uniform flight lines, so that physically similar features within a flight line exhibit consistent temperatures. Furthermore,

- This method can be automated, is computationally fast and highly transferable; thus, it is able to be operationally applied to large H-res TIR datasets.
- TURN-surfaces may represent a useful tool for urban planners to identify urban heat sinks, and localized urban heat islands.
- To the best of our knowledge, this is the first time in the GEOBIA literature, that discrete road-objects are defined and sampled to create a continuous temperature variability field for the full scene, which is then used to automatically obtain a ‘microclimate-free’ scene.
- This research meets a recent challenge to the GEOBIA community to integrate pre-defined GIS vector objects (Hay, 2014) within the analytical process rather than solely defining image-objects with segmentation methods that have no unique solution (Schott et al., 1988; Isaaks and Srivastava, 1989).

## References

- Bain, L. 2007. Object-oriented representation of environmental phenomena: is everything best represented as an object? *Annals of the Association of American Geographers*. 97-2, 267–281.
- Blaschke, T., Hay, G. J., Maggi, K., Lang, S., Hofmann, P., Addink, E., Feitosa, R.Q. Meer, F.V.D., Werff, H.V.D., Coillie, F.V. 2014. Geographic Object-Based Image Analysis – towards a new paradigm. *ISPRS Journal of Photogrammetry and Remote Sensing*. 87, 180-191.
- Bogren, J., Gustavsson, T. 1991. Nocturnal air and Road surface temperature variations in complex terrain. *International Journal of Climatology* 11:4, 443-455.
- Bors, A.G., Kechagias, L., Pitas, I. 2002. Binary morphological shape-based interpolation applied to 3-D tooth reconstruction. *IEEE Transactions on Medical Imaging*. 21:2, 100-108.
- Castilla, G., Hay, G.J. 2008. Image-objects and geo-objects. In: *Object-Based Image Analysis. Spatial concepts for knowledge-driven remote sensing applications*. Ed.; T. Blaschke, S. Lang, G. J. Hay. Springer-Verlag, New York, Chapter 1.5, 91-110.
- Crippen, R.E., Hook, S.J., Fielding, E.J. 2007. Nighttime ASTER thermal imagery as an elevation surrogate for filling SRTM DEM voids. *Geophysical Research Letters*. 34-L01302, 1-5.
- De Boor, C. A. 1978. *Practical guide to splines, Volume 27*; Springer-Verlag: New York. pp. 368
- Franke, R. 1982. Scattered data interpolation: tests of some methods. *Mathematics of Computation*. 38-157, 181–200.
- Franke, R.A. 1979. *Critical comparison of some methods for interpolation of scattered data*, Naval Postgraduate School, Technical Report, NPS 53-79-003.
- Friedl, M.A., Davis, F.W. 1994. Sources of variation in radiometric surface temperature over a tallgrass prairie. *Remote Sensing of Environment*. 48, 1-17.

- Gallo, K.P., Owen, T.W. 1998. Assessment of urban heat island: a multi-sensor perspective for the Dallas-Ft. Worth, USA region. *Geocarto International*. 13-4, 35–41.
- Giannini, A., Saravanan, R., Chang, P. 2003. Oceanic forcing on sahel rainfall on interannual to interdecade time scales. *Science*. 302-5647, 1027-1030.
- Gluch, R., Quattrochi, D.A., Luvall, J.C. 2006. Multi-scale approach to urban thermal analysis, *Remote Sensing of Environment*. 104-2, 123–132.
- Gonzalez, J.E., Luvall, J.C., Rickman, D., Comarazamy, D., Picon, A.J., Harmsen, E.W., Parsiani, H., Ramirez, N., Vasquez, RE., Williams, R., Waide, R.B., Tepley, C.A. 2005. Urban heat islands developing in coastal tropical cities. *Eos, Transactions American Geophysical Union*. 86, 397- 403.
- Grevera, G.J., Udupa, J.K. 1996. Shape-based interpolation of multidimensional grey-level images. *IEEE Transactions on Medical Imaging*. 15-6, 881-892.
- Gustavson, T. 1994. A study of air and Road-surface temperature variations during clear windy nights. *International Journal of Climatology*. 15, 919-932.
- Gustavson, W.T., Handcock, R., Gillespie, A.R., Tonooka, H. 2003. An image sharpening method to recover stream temperatures from ASTER images. In *Remote Sensing for Environmental Monitoring, GIS applications and Geology*, ed.; M. Ehlers, Proceedings of SPIE. 4886, pp. 72–83.
- Hartz, D.A., Prashad, L., Golden, J., Brazel, A. J. 2006. Linking satellite images and hand held infrared thermography to observe neighborhood climate conditions. *Remote Sensing of Environment*. 104-2. 190-200.

- Hay, G.J. 2014. GEOBIA – Evolving Beyond Segmentation. Keynote Presentation: 5th International GEOBIA Conference. Thessaloniki, Greece, May 24. Pp. 54  
<http://geobia2014.web.auth.gr/geobia14/sites/default/files/pictures/hay.pdf>
- Jensen, J. R. Remote Sensing of the Environment: An Earth Resource Perspective, 2nd ed.; Upper Saddle River: Pearson Prentice Hall, 2007; Chapter 8, pp. 249-290.
- Hay, G.J., Castilla, G. 2008. Geographic Object-Based Image Analysis GEOBIA: A new name for a new discipline? In: Object-Based Image Analysis – spatial concepts for knowledge-driven remote sensing applications. Eds: T. Blaschke, S. Lang, G. J. Hay. Springer-Verlag. 1.4, 81-92.
- Hay, G.J., Kyle, C., Hemachandran, B., Chen, G., Rahman, M.M., Fung, T.S., Arvai, J.L. 2011. Geospatial technologies to improve urban energy efficiency. Remote Sensing. 3-7. 1380-1405.
- Herman, G.T., Zheng, J., Bucholtz, C.A. 1992. Shape-based interpolation. IEEE Computer Graphics and Applications. 12-3, 69-79.
- Isaaks, E.H., Srivastava, R.M. 1989. An Introduction to Applied Geostatistics, Oxford University Press: New York.
- ITRES, 2014. <http://www.itres.com/> (accessed on June 13, 2014).
- Jacob, F., Francois, P., Schmugge, T., Vermote, E., French, A., Ogawa, K. 2004. Comparison of Land Surface Emissivity and Radiometric Temperature Derived from MODIS and ASTER. Remote Sensing of Environment. 90, 137-152.
- Junhui, L., Jianqiang, W. 2010. Road surface condition detection based on road surface temperature and solar radiation. International Conference on Computer, Mechatronics, Control and Electronic Engineering (CMCE). 4, 4-7.

- Kidder, S.Q., Wu, H.T. 1987. A multispectral study of the St. Louis area under snow-covered conditions using NOAA-7 AVHRR data. *Remote Sensing of Environment*. 22, 159–172
- Kim, H.H. 1992. Urban heat island. *International Journal of Remote Sensing*. 13, 2319–2336.
- King, M.D., Menzel, W.P., Kaufman, Y.J., Tanre, D., Gao, B.C., Platnick, S., Ackerman, S.A., Remer, L.A., Pincus, R., Hubanks, P.A. 2003. Cloud and aerosol properties, precipitable water, and profiles of temperature and water vapor from MODIS, *IEEE Transaction of Geoscience and Remote Sensing*. 41, 442 – 458.
- Lagouarde, J.P., Ballans, H., Moreau, P., Guyon, D., Coraboeuf, D. 2000. Experimental study of brightness surface temperature angular variations of maritime pine (*Pinus pinaster*) stands. *Remote Sensing of Environment*. 72-1, 17-34.
- Nichol, J.E. 2009. An emissivity modulation method for spatial enhancement of thermal satellite images in urban heat island analysis. *Photogrammetric Engineering & Remote Sensing*. 75- 5, 1-10.
- Parker, J.A., Kenyon, R.V., Troxel, D.E. 1983. Comparison of interpolating methods for image resampling. *IEEE Transactions on Medical Imaging*. 2-1, 31-39.
- Pozo, D., Olnro, F. J., & Alados-Arboledas, L. 1997. Fire detection and growth monitoring using a multitemporal technique on AVHRR mid-infrared and thermal channels. *Remote Sensing of Environment*. 60-2, 111-120.
- Prakash, A. 2000. Thermal remote sensing: concepts, issues and applications. *International Archives of Photogrammetry and Remote Sensing*. XXXIII: B1.
- Pu, R., Gong, P., Michishita, R., Sasagawa, T. 2006. Assessment of multi-resolution and multi-sensor data for urban surface temperature retrieval. *Remote Sensing of Environment*. 104, 211-225.

- Quattrochi D.A., Luvall, J.C. 1999. Thermal infrared remote sensing for analysis of landscape ecological processes: methods and applications. *Landscape Ecology*. 14, 577–598.
- Quattrochi D.A., Ridd, M.K. 1998. Analysis of vegetation within a semi-arid urban environment using high-spatial resolution airborne thermal infrared remote sensing data. *Atmospheric Environment*. 32, 19–33.
- Rahman, M.M., Hay, G.J., Couloigner, I., Hemachandran, B., Bailin, J., Zhang Y., Tam, A. 2013. Geographic Object-Based Mosaicking (OBM) of high-resolution thermal airborne imagery (TABI-1800) to improve the interpretation of urban image objects. *IEEE Geoscience and Remote Sensing Letters*. 10-4, 918-922.
- Renka, R.J. 1984. A triangle-based C1 interpolation method. *Rocky Mountain Journal of Mathematics*. 14-1.
- Roth, M., Oke, T.R., Emery, W.J. 1989. Satellite-derived urban heat island from three coastal cities and the utilization of such data in urban climatology. *International Journal of Remote Sensing*. 10, 1699–1720.
- Santamouris, M., Papanikolaou, N., Livada, I., Koronakis, I., Georgakis, A., Assimakopoulos, D.N. 2001. On the impact of urban climate on the energy consumption of buildings. *Solar Energy*. 70-3, 201-216.
- Schott, J.R., Salvaggio, C., Volchok, W.J. 1988. Radiometric scene normalization using pseudo invariant features, *Remote Sensing of Environment*. 26-1, 1-14.
- Streutker, D.R. 2002. A remote sensing study of the urban heat island of Houston, Texas, *International Journal of Remote Sensing*. 23-13, 2595 – 2608.
- The city of Calgary. 2012. Road Construction: 2012 Standards and Specifications. Transportation Department, The City of Calgary, ROADS Construction Division.

<http://www.calgary.ca/Transportation/Roads/Pages/Contractors-and-Consultants/Contractors-and-Consultants.aspx>

Voogt, J.A., Oke, T.R. 1997. Complete urban surface temperatures. *Journal of Applied Meteorology*. 36, 1117–1132.

Voogt, J.A., Oke, T.R. 2003. Thermal remote sensing of urban climates. *Remote Sensing of Environment*. 86-3, 370-384.

## **Linking Chapters 3 and 4**

In Chapter 3, we described a method (TURN) to mitigate the radiometric issues within three airborne thermal infrared flight lines. However, a large urban area requires the acquisition of many flight lines – typically over many hours or days. This results in radiometric (i.e. radiant temperature) differences between the TIR flight lines that make up a mosaic. These differences occur over time primarily from atmospheric and microclimate variability occurring during flight line acquisitions, in comparison to a satellite acquisition that essentially covers a very large area, instantaneously. In an effort to mitigate these visible effects on the mosaicked scene, Chapter 4 evaluates the utility of four different relative radiometric normalization (RRN) techniques applied over two adjacent multi-temporal TABI-1800 flight lines (each ~35.5 km x 0.9 km, at 50 cm spatial resolution). It is expected that the best RRN method will produce a seamless mosaic that appears as if all the flight lines were acquired under identical atmospheric and environmental conditions.

## **Chapter Four: A comparison of four relative radiometric normalization (RRN) techniques for mosaicking H-res multi-temporal thermal infrared (TIR) imagery of a complex urban scene<sup>22</sup>**

### **4.1 Abstract**

High-spatial resolution (H-res) thermal infrared (TIR) airborne imagery, such as the TABI-1800 (Thermal Airborne Broadband Imager) provides unique surface temperature information that can be used for urban heat loss mapping, heat island analysis, and landcover classifications. For mapping large urban areas at a sub-meter resolution, airborne thermal imagery needs to be acquired over a number of flight lines and mosaicked together. However, due to radiometric variations between flight lines the same objects (observed within the scene overlap) tend to have different temperature characteristics, resulting in reduced visual and radiometric agreement between the flight lines composing the final mosaicked output.

In an effort to produce a visually ‘seamless’ TIR mosaic over a complex urban scene, we evaluate four relative radiometric normalization techniques on two adjacent multi-temporal TABI-1800 flight lines (each ~35.5 km x 0.9 km, at 50 cm spatial resolution, and 0.05 °C thermal resolution) and describe their effects on the resulting mosaic. The methods evaluated include: (i) Histogram Matching, (ii) Pseudo Invariant Feature (PIF) Based Linear Regression, (iii) PIF-Based Theil-Sen Regression, and (iv) No-Change Stratified Random Samples (NCSRS) Based Linear Regression. Based on four criteria: (a) the speed of computation, (b) the ability to automate, (c) the visual assessment, and (d) the statistical analysis of four landcover classes (road, water, grass, and rooftops), results show that NCSRS-Based Linear Regression produces the best overall results

---

<sup>22</sup> This work (PHOTO-D-14-00266) is co-authored by Rahman, M. M., Hay, G. J., Couloigner, I., Hemachandaran, B., and Bailin, J and has recently been accepted with corrections in ‘The ISPRS Journal of Photogrammetry and Remote Sensing’

closely followed by Histogram Matching. Specifically, these two radiometric normalization techniques: (1) increase the visual and statistical agreement between the tested TIR airborne flight lines (NCSRS Based Linear Regression increases radiometric agreement between flight lines by 53.3% and Histogram Matching by 52.4%), (2) produce a visually seamless image mosaic, and (3) can be rapidly automated within an operational multi-flight line, multi-temporal mosaic workflow.

**Keywords:** Relative Radiometric Normalization (RRN), Thermal Infrared Imagery, High Resolution, Radiometric Variability, TABI-1800, Airborne.

#### **4.2 Introduction: radiometric normalization**

Unlike optical or active microwave remote sensing techniques that measure reflected energy, thermal infrared (TIR) remote sensing measures radiant energy emitted from ground objects, resulting in measures of relative or radiant temperature (Prakash, 2000). As such, TIR data are useful for identifying surface temperatures and emissivity, and for distinguishing features such as rock type, soil moisture, and geothermal anomalies. However, these data tend to be largely underutilized due to: (i) difficulties calibrating and correcting the measured radiance to consistent physical quantities, (ii) the challenges of accurately estimating surface energy fluxes over complex terrain, which may consist of numerous vegetation classes, sloped surfaces, water bodies, bare soil or urban landscapes (Voogt and Oke, 2003), (iii) the detection and removal of cloud effects (Quattrochi and Luvall, 1999), and (iv) the removal of microclimate effects (Ben-Dor and Saaroni, 1997; Rahman et al., 2013). Furthermore, current satellite platforms provide moderate to low spatial resolution thermal imagery (e.g., 60 meter: LANDSAT ETM+ to 1 km: NOAA AVHRR), which are not appropriate for detailed thermal urban mapping.

For mapping a large urban area at a fine spatial resolution (0.5-2 meter), airborne TIR imagery typically needs to be acquired in a number of flight lines and mosaicked together (Weng,

2009; 2012). Unfortunately, due to radiometric variations between flight paths, similar objects may express different spectral characteristics, making image analysis difficult (Tuominen and Perkkarinen, 2004). For example, images acquired at different times of the day, or on different dates have radiometric variations (even for the same object) caused by varied sun angles, illumination differences, atmospheric conditions and microclimatic conditions, rather than by physical changes in surface properties (Yang and Lo, 2000). Therefore, when comparing, or mosaicking images from different times/dates and/or different sensors, it is necessary to radiometrically normalize one image to another to produce images of similar radiometric response, or to produce a seamless composite map (by mosaicking). Such normalization may be performed either by: (i) an *absolute* radiometric correction, or (ii) a *relative* radiometric normalization.

Absolute radiometric correction reveals actual surface response (actual surface response refers to the surface radiance/reflectance/emittance that is not subjected to atmospheric factors, or to any other external factors) by removing the effects of the atmosphere (Jensen, 2005). To achieve this, several radiative transfer models have been developed including: (i) LOWTRAN (Kneizys et al., 1983), (ii) MODTRAN (Berk et al., 1989), and (iii) 6S (Vermote et al., 1995), each of which models specific characteristics of atmospheres to estimate the effect of absorption and scattering in related remote sensing imagery. However, for an 'accurate' estimation of atmospheric influences from radiative transfer models, it is necessary to obtain atmospheric properties at the time of data collection including air temperature, relative humidity, atmospheric pressure, visibility, altitude, and elevation. Even then, these expensive measurements (in terms of equipment and deployment costs) tends to be sparsely sampled. Conversely, relative radiometric normalization (RRN) aims at minimizing the radiometric differences between images so it appears that different images were captured under identical atmospheric conditions, rather than at

completely removing the effects of the atmosphere. In a relative radiometric normalization, one of the images is considered as the *master*<sup>23</sup> image and all other images (*slave* images) are normalized in such a way that they become radiometrically similar to the master image (Hall et al., 1991).

With increasing access to massive archives of historical remotely sensing data (e.g., LANDSAT, ASTER, MODIS, and NOAA collected over the last 40+ years), remarkable opportunities to use these data for long-term change detection have been observed (Lu et al., 2004, Chen et al., 2012). Nevertheless, it has always been a challenge to incorporate data collected at different times and/or from different sensors. Difficulty in obtaining atmospheric properties at the time of data collection, along with an absence of historical climate/weather data have further reduced the opportunity to perform absolute radiometric correction on multitemporal images (Du et al., 2002). However, since RRN does not require any atmospheric data, it has been extensively used by the remote sensing community to compare images of different times, and/or to mosaic adjacent scenes together. For example, Hall et al. (1991) evaluated seven different relative radiometric normalization methods applied to Landsat MSS multispectral images collected in 1973 and in 1990. They compared results visually and statistically, and concluded that a linear regression equation obtained from dark and bright reference pixels produced the best results. An automatic RRN technique was also demonstrated by Canty et al. (2004), who described the use of *Multivariate Alteration Detection* (MAD)<sup>24</sup> to automatically define *pseudo invariant features* (PIFs) within multispectral images of the same area, collected at two different times. They evaluated this technique using data from three different sensors (Landsat TM, Landsat ETM+, and

---

<sup>23</sup> The master image is the reference image whereas the slave image(s) are normalized to the master image.

<sup>24</sup> Multivariate Alteration Detection is an automatic change detection method proposed by Nielsen et al. (2002) that distinguishes change/no change pixels between bi-temporal images

SPOT HRV) over three different study areas (Nevada, Morocco and Kenya) against manually collected pseudo invariant features. Their results showed that automatically obtained PIFs generated better results than those produced by manual selection. Similarly, Fernandes and Leblanc (2005) tested *Theil-Sen*<sup>25</sup> regression against least squares (linear) regression in three case studies involving the integration of remote sensing and field data to estimate Leaf Area Index (LAI). They concluded that TS regression was relatively simple and that the results were robust to outliers, thus more reliable. Olthof et al., (2005) also tested the performance of the TS estimator against Gaussian linear regression using multispectral Landsat 7 ETM+ data and SPOT-4 vegetation data (1 km spatial resolution) and concluded that the TS estimator performed better than Gaussian linear regression. More recently, Yu et al. (2010) divided two ASTER images (acquired at different times) into high- and low-temporal frequency components. They considered the high frequency components as changes on the surface rather than being due to the impact of the atmosphere and thus did not perform any normalization on these components. Instead, they manually extracted PIFs from the low frequency components and developed a linear regression equation to radiometrically normalize the low frequency components of the slave image to the master image. They concluded that their RRN approach improved the accuracy of dynamic monitoring. Similarly, a number of researchers, including Salvaggio (1993), Furby and Campbell (2001), and Du et al. (2002) tested different RRN algorithms over multispectral multitemporal datasets and reported improved results.

---

<sup>25</sup> The Theil-Sen (Theil, 1950, Sen, 1968) estimator is a robust linear regression model that uses the median of pairwise slopes as an estimator of the slope parameter of the correlation between two datasets.

Although RRN has been extensively tested on multispectral data, very few studies have been conducted to radiometrically normalize multitemporal TIR imagery. With on-line access to satellite-based moderate resolution (i.e. 60-120 m) TIR imagery as well as an availability to high-resolution airborne (i.e. 0.5 m - 5 m) TIR platforms, thermal images are increasingly being used for urban and rural temperature studies (Carnahan and Larson, 1990, Streutker, 2002), urban heat island analysis (Gallo and Tarpley, 1996; Hafner and Kidder, 1999; Gonzalez et al., 2005; Gluch et al., 2006), forest fire detection (Giglio et al., 2008), surface energy flux estimation (Wan and Li, 1997; Voogt and Grimmond, 2000; French et al., 2005), building waste heat analysis (Hay et al., 2011) and others. Although Warner and Chen (2001), Koltunov and Ustin (2007), and Scheidt et al. (2008) and others, have applied radiometric normalization techniques on moderate to low-resolution (60 m to 1 km) TIR imagery, this research recognizes an emerging need to evaluate the utility of relative radiometric normalization techniques on H-res TIR data (Hay et al., 2011; Rahman et al., 2013).

Based on this summary, and as part of an ongoing TIR research in urban energy efficiency (Hay et al., 2011), the goal of this paper is to operationally evaluate four existing relative radiometric normalization techniques on two adjacent H-res TIR flight lines, so that it appears as if the scenes were collected at the same time, under the same microclimatic and atmospheric conditions. For operationalization, the best technique needs to be automated, computationally fast, and produce strong visual and statistical results.

### **4.3 Methods**

In order to evaluate the utility of RRN techniques on H-res TIR data, this section describes four relative radiometric normalization techniques applied on two adjacent flight lines of TABI-1800 imagery. The earliest acquired flight line is considered the master image and the later as the

slave. The overlap areas of the master and the slave images represent the same ground targets observed through the same TIR sensor, but collected ~25 minutes apart. Differences in this overlap are expected to represent deviations in surface temperatures caused by the environment (i.e. wind, humidity, etc.) rather than by changes in the surface itself. To radiometrically normalize the slave image to the master, these overlap areas are extracted from both scenes and relative radiometric normalization models are developed from them. The resulting radiometric adjustment is then applied on the entire slave image, rather than only on the overlap section. The performances of these methods are then evaluated based on the visual and Root Mean Square Error (RMSE) analysis of four different landcover types within the overlap. The following sections describe the dataset and these RRN methods in detail.

#### ***4.3.1 Study area and dataset***

The study area is located in the west part of The City of Calgary, Alberta, Canada (Figure. 4-1), and is represented by two TABI-1800 (Thermal Airborne Broadband Imager) flight lines acquired between 01:00 to 02:00 AM on May 13, 2012. Each flight line is ~0.9 km wide x 35.5 km long and acquired with a 50 cm spatial resolution. Under ideal conditions, each flight line has a 30% overlap, with adjacent flight lines. The TABI-1800 is an airborne thermal camera developed by ITRES Research Limited (2012) with a swath width of 1,800 pixels (FOV:  $\pm 20^\circ$ ) in the 3.7- 4.8  $\mu\text{m}$  spectral region, a thermal resolution of 0.05  $^\circ\text{C}$ , and the ability to collect data up to 175  $\text{km}^2$  per hour at 1 m spatial resolution (Hay et al., 2011). These data were collected as 14 bit float from an average altitude of 1250 m above ground level and a digital terrain model (10 m spatial resolution) was used to orthorectify the images. Combined with onboard GPS data, this resulted in an overall geometric error of  $\pm 1$  meter (which represents  $\pm 2$  pixels).

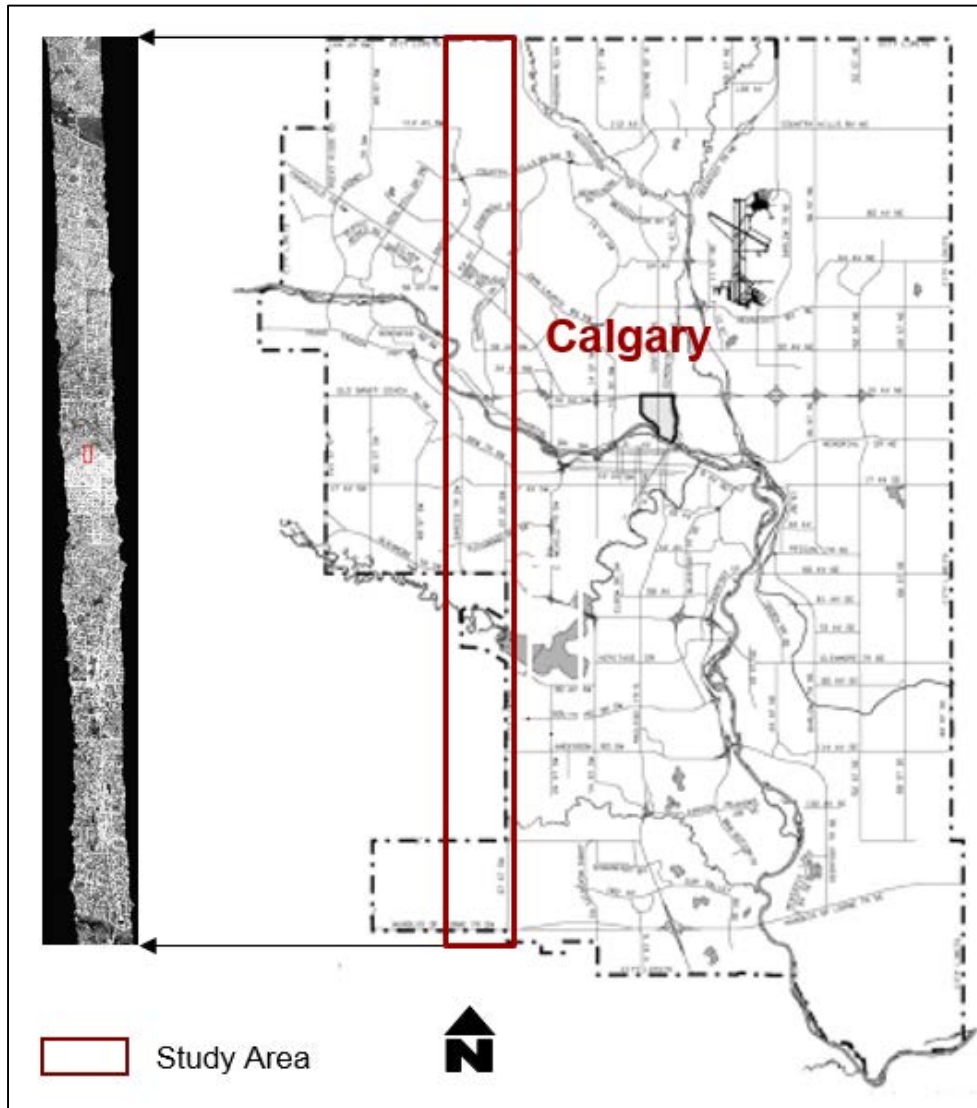


**Figure 4-1: A map showing the approximate location of the flight lines used in this study.**

#### ***4.3.2 Relative radiometric normalization (RRN) algorithms***

This section briefly describes the following four RRN techniques: (i) Histogram Matching, (ii) PIF Based Linear Regression, (iii) PIF Based Theil-Sen Regression, and (iv) No-Change Stratified Random Sample (NCSRS) Based Linear Regression.

### 4.3.2.1 Histogram matching

Richards and Jia (2005) defined Histogram Matching as the scalar shift of the slave histogram to the master histogram based on the mean difference (mean difference is a measure of dispersion between two independent datasets) as shown in Figure 4-2.

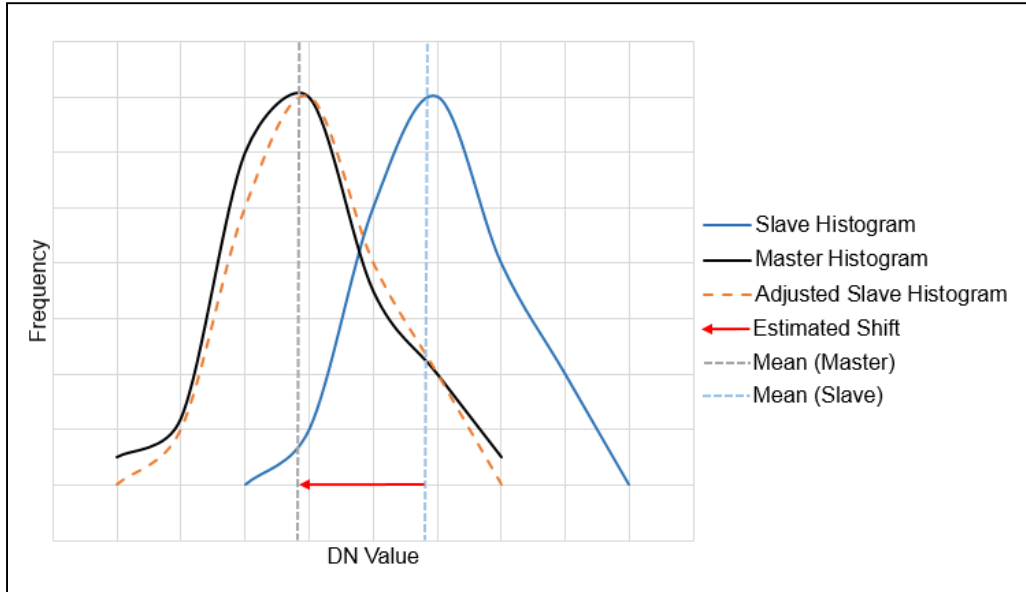


**Figure 4-2: A hypothetical example of the Histogram Matching technique**

To operationalize this method, the mean difference of the overlap sections was calculated (between the master and the slave images) using Equation 4-1, then shifted the slave histogram (of the entire image, not just the overlap) to the master histogram using the calculated mean difference.

$$MD = \frac{1}{n} \sum_{i=1}^{i=n} (y_i - x_i) \quad (\text{Equation 4-1})$$

Where,

$MD$  = mean difference

$n$  = number of pixels

$x_i$  = value of pixel  $i$  in the slave image

$y_i$  = value of pixel  $i$  in the master image

#### 4.3.2.2 Pseudo invariant feature based radiometric normalization

It has been argued that the spectral properties of some features (such as soil and seasonal vegetation) change over time, consequently, their use as reference features for the radiometric normalization of multitemporal images may introduce erroneous results. To mitigate these errors, Schott et al. (1988) and Salvaggio (1993) suggested using Pseudo Invariant Features (PIFs) as references for radiometric normalization as these features are expected to provide consistent radiometric responses over time. To perform a PIF-Based radiometric normalization, we closely examined the overlap portions of the master and the slave images and carefully manually selected 30 samples, that is, region of interests (ROIs) representing three types of landcover (i.e. 10 samples for each type of landcover) - grass (cool), road (hot) and (river) water (in-between temperatures), which are expected to be radiometrically invariant over the (brief) acquisition time. Each sample contains a region of 20 to 24 pixels (5-6 sq. m). The digital numbers (DN) of each class plotted in a histogram (Figure 4-3), show (i) a clear boundary between the selected landcover types, and (ii) a significant variability within each landcover class. The average DN values within each PIF sample area for the slave image were then plotted against those of the master image to enable two different types of regression techniques, (i) Linear Regression, and (ii) Theil-Sen (TS) Regression.

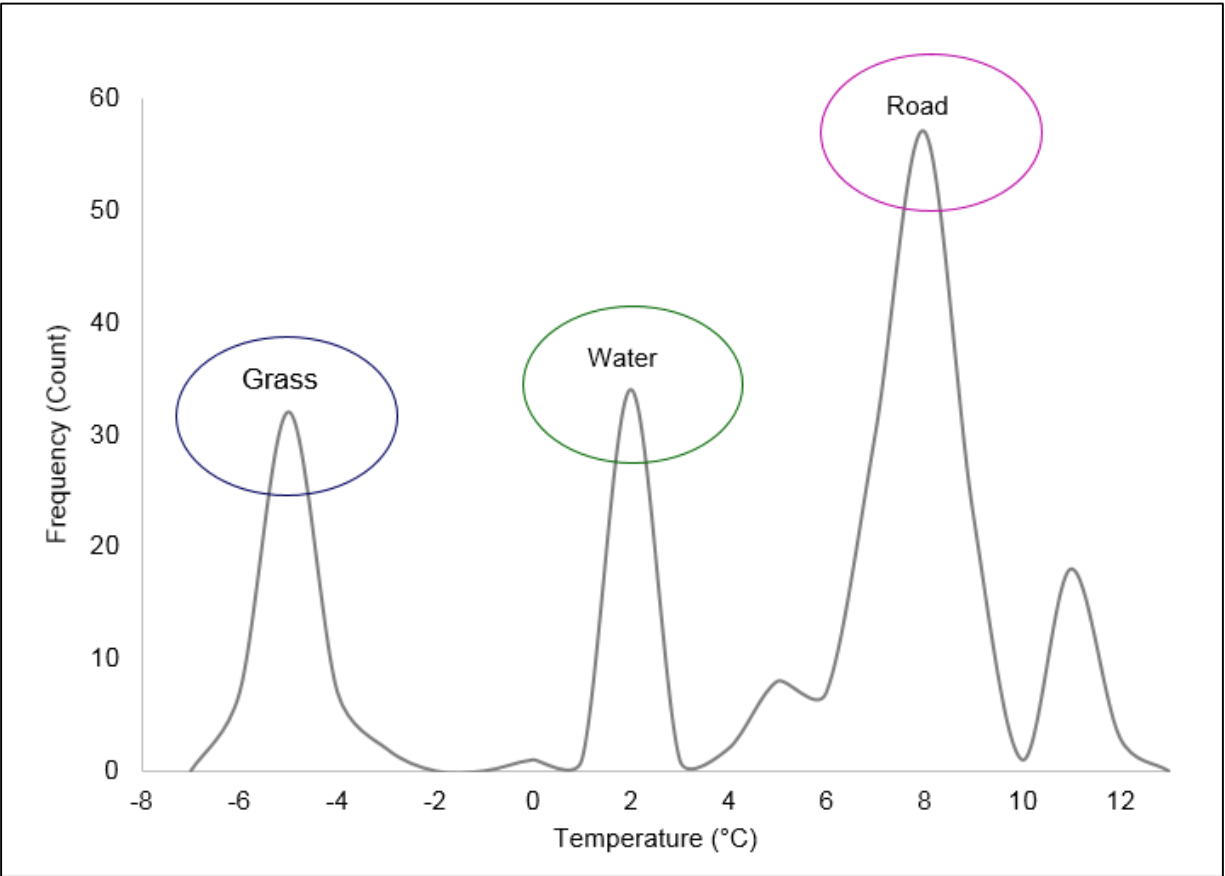


**Figure 4-3: Histogram of three classes of Pseudo Invariant Features (grass, water, and road) selected for Relative Radiometric Normalization (RRN) showing both the intra-class variability and inter-class separability of the selected PIFs.**

#### 4.3.2.2.1 PIF-based linear regression

Linear Regression normalization is based on the assumption that the atmospheric differences between images of a same geographic location, but collected at different times, are linearly correlated (Schott et al., 1988; Hall et al., 1991). To perform a PIF-Based Linear Regression, the average DN values (described in 4.3.2.2) of the PIFs are plotted (Figure 4-4) and a linear regression equation is fitted to the points cloud (Equation 4-2). This fitted regression equation is then applied to the entire slave image to radiometrically normalize it to the master.

$$y = 0.9952 x - 0.4457 (R^2 = 0.95) \quad \text{(Equation 4-2)}$$

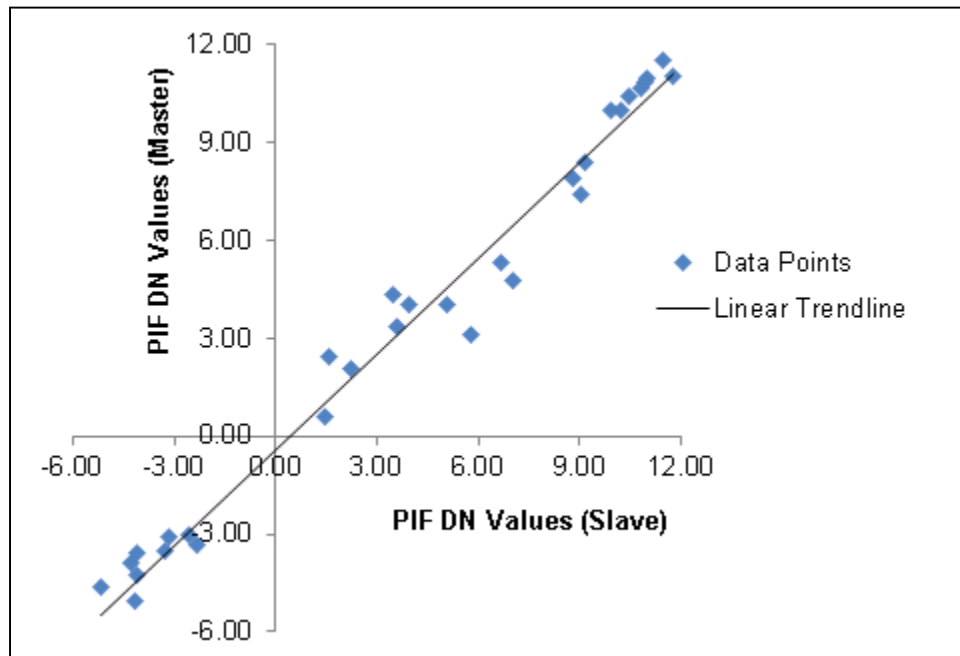


**Figure 4-4: A scatterplot of Pseudo Invariant Features (PIFs) selected from three landcover classes (grass, water, and road) with a linear trend line showing the linear relationship between the master and the slave images.**

#### 4.3.2.2.2 PIF-based Theil-Sen (TS) regression

The Theil-Sen Regression model uses the median of pairwise slopes<sup>26</sup> as an estimator of the slope parameter to describe the correlation between two datasets (Peng et al., 2008). The pairwise slopes were calculated for the same 30 pairs of PIFs previously noted and their median slope ( $m_m$ ) was computed. Then, the median slope value and the median of the pixel values of the PIFs from the master (as Y) and from the slave (as X) were introduced into a linear equation to calculate the y-intercept. The median slope ( $m_m$ ) and the y-intercept formed the linear equation given in Equation 4-3. This equation was then used to radiometrically normalize the slave image to the master image (Figure 4-5).

$$y = 1.0344x - 1.27(R^2 = 0.71) \quad \text{(Equation 4-3)}$$

---

<sup>26</sup> The pairwise slope is the slope of each possible pair of values in the dataset.

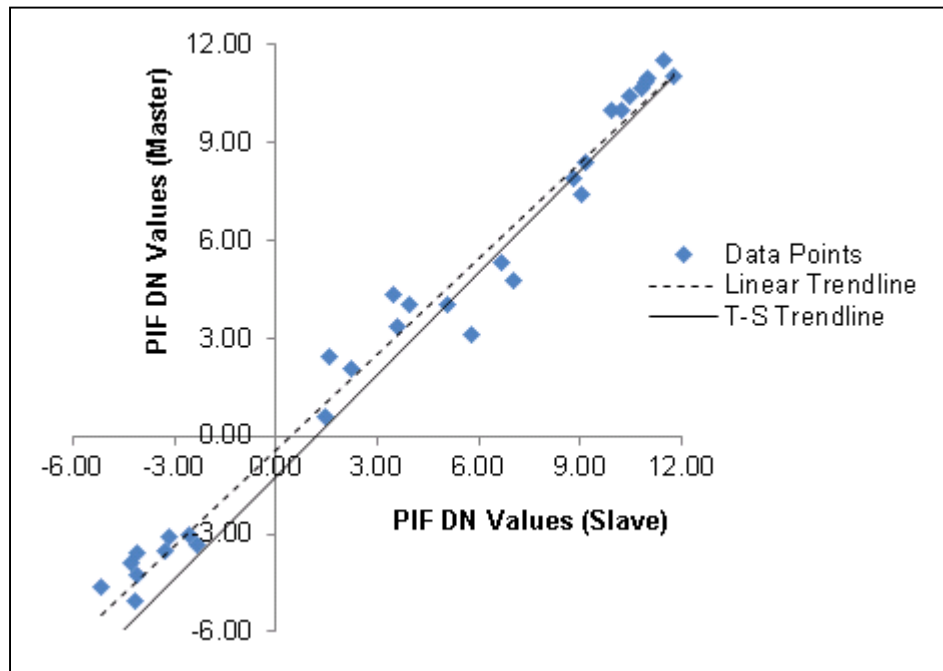


**Figure 4-5: A scatterplot of the PIFs modeled with the Theil-Sen trend line (solid black) and with a linear trendline (dotted black).**

#### 4.3.2.3 No-change stratified random sample (NCSRS) based linear regression

NCSRS Based RRN methods search for no-change areas (i.e. where the landcover is not altered) within the image overlap, and use a number of selected sample points from the no-change areas as a reference for radiometric normalization. Relative radiometric normalization using a no-change (NC) set was described by Evidge et al. (1995), who introduced a scatterplot of the master and the slave images to find the no-change set, with a view to proactively removing outliers before fitting.

Since our images were collected only ~25 minutes apart, it is unlikely that a change in landcover took place within this short time period. However, due to a ( $\pm 1$  m) geometric error between the master and the slave images (see section 4.3.1), distortion along the edges of ground objects appears as a landcover change. In an effort to reduce geometric error between these scenes, we resampled the master and the slave images from 50 cm to 2 m (i.e. 2 times their reported mean

geometric error) using the median of the input DN values as the output DN values. Median was used instead of mean because it is more representative of the input DNs, as the mean is strongly influenced by outliers. However, this two-meter dataset was only used to develop these RRN equations, which were then applied to the original (50 cm) slave image.

To further identify any geometric distortion (noise), an image difference histogram was created from the master and the slave overlap (i.e. Master DN's – Slave DN's). From the resulting difference image and statistics (Figure 4-6), less than 1% of the overlap difference pixels fall in areas of high change (i.e. with temperature differences approximately  $\pm 5^{\circ}\text{C}$ ). Therefore, a range of mean  $\pm 3\text{SD}$  (Standard Deviation) was heuristically considered as identifying areas of no change (Figure 4-6). The remaining areas were then masked within the master and the slave overlap sections, and samples are collected from them.

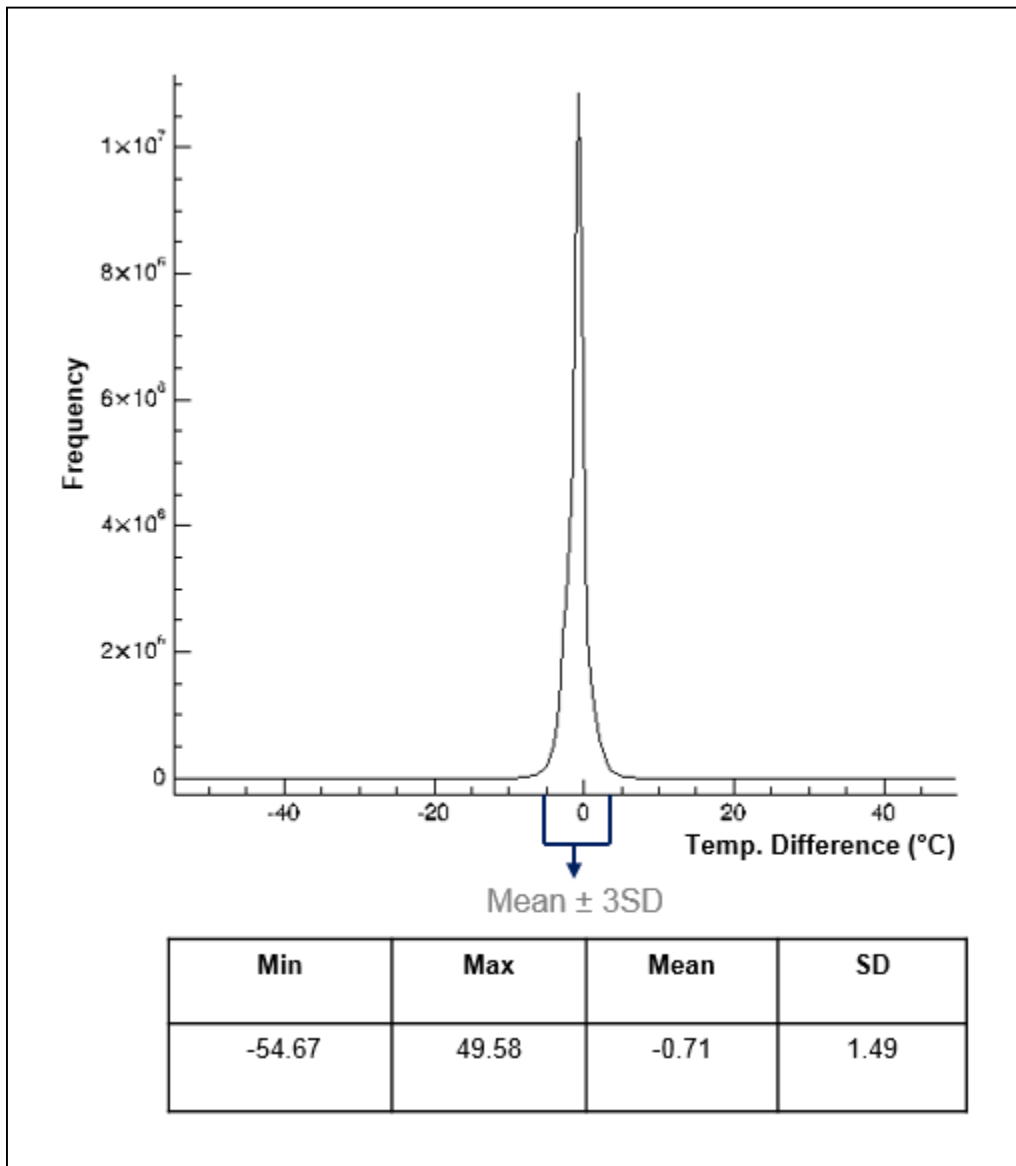


**Figure 4-6: A histogram showing the absolute difference between the master and the raw slave image with associated basic statistics. The range shown by the blue square bracket ( $\text{Mean} \pm 3\text{SD}$ ) represents no change areas.**

To collect these samples, the no-change DN's (both master and slave pairs) are sorted in ascending order and a random point is collected from each 500 point bin (~0.2% of the population). The data are sorted so that the entire radiometric range of the image can be covered and different landcover types (with different temperatures) can be included in the samples. This sampling

strategy is chosen for simplicity and automation. In this example, it resulted in the collection of 28,033 sample points, which were then used to develop a linear regression model.

To perform NCSRS-Based Linear Regression, the sample DN values were plotted in a scatterplot (Figure 4-7) and a linear regression equation (Equation 4-5) was computed. This regression equation was then applied over the entire slave image to radiometrically normalize it to the master image.

$$y = 0.9124x + 0.334 \quad (R^2 = 0.88) \quad \text{(Equation 4-5)}$$

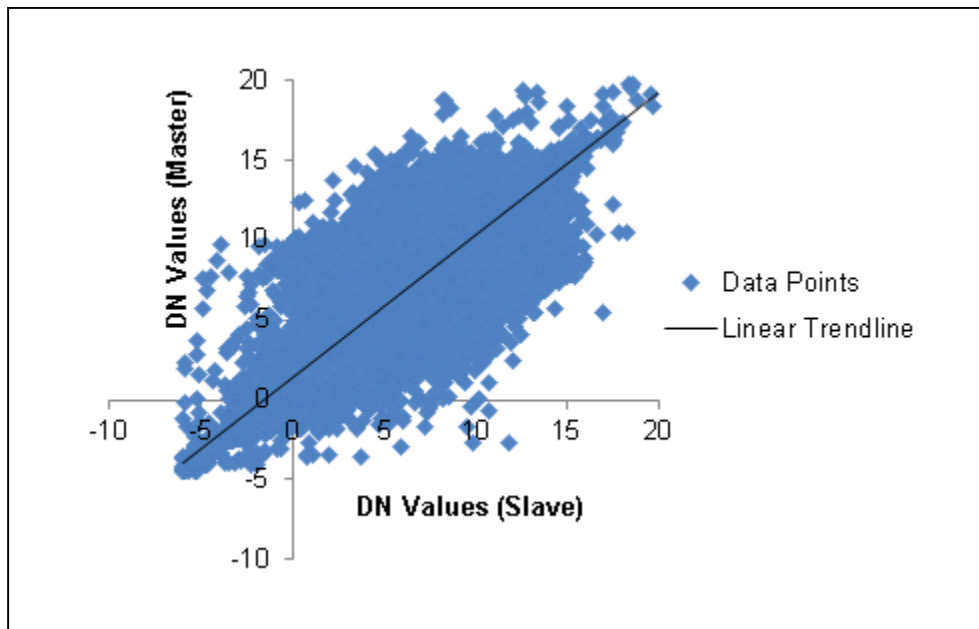


**Figure 4-7: A scatterplot displaying NCSRS-Based Linear Regression trendline derived from 28,033 samples.**

### ***4.3.3 Accuracy assessment***

Relative Radiometric Normalization (RRN) was performed on two adjacent airborne thermal flight lines using four different techniques. It is expected that after applying RRN, similar landcover classes found in both flight lines will provide visually and statistically similar radiometric responses. To compare the performance of the applied techniques, the *Root Mean Square Error* (RMSE) is calculated between the radiometrically normalized images and the master

image, based on 2000 stratified random test pixel pairs that were extracted from the overlap section. These independent samples were not used to generate any models. They represent four landcover types: (i) water, (ii) road, (iii) grass, and (iv) rooftops. The RMSE for each landcover class along with the overall RMSE for all combined classes are calculated using Equation 4-6.

$$RMSE = \sqrt{\frac{\sum_1^n (DN_{master} - DN_{slave})^2}{n}} \quad (\text{Equation 4-6})$$

In addition to this assessment, each method is then ranked (based on its performance) from 1: best to 4: worst for four evaluation criteria. This ranking provides a simple but effective summary, highlighting the attributes of the most appropriate operational method to radiometrically normalize the TABI-1800 dataset. These results are presented and discussed in the following section.

#### **4.4 Results and discussions**

This section describes the visual and statistical results from four different RRN methods. It also includes a related discussion on computation time, automation and on the ranking scheme used to define the most operational RRN method.

##### ***4.4.1 Visual interpretation***

To visually compare the results of the evaluated algorithms, each normalized slave image was separately mosaicked with the master image and features along the mosaic join line were assessed. Visual interpretation reveals that most of the methods exhibit improvement over the raw dataset. However, the magnitude of improvement differs, according to the method used and the type of landcover/ground targets assessed.

For example, Figure 4-8A (raw image) displays a portion of a river vertically bisected by the mosaic line. Histogram Matching (Figure 4-8B) and NCSRS-Based Linear Regression (Figure 4-8E) produce the best visual results, with nearly seamless mosaic lines.

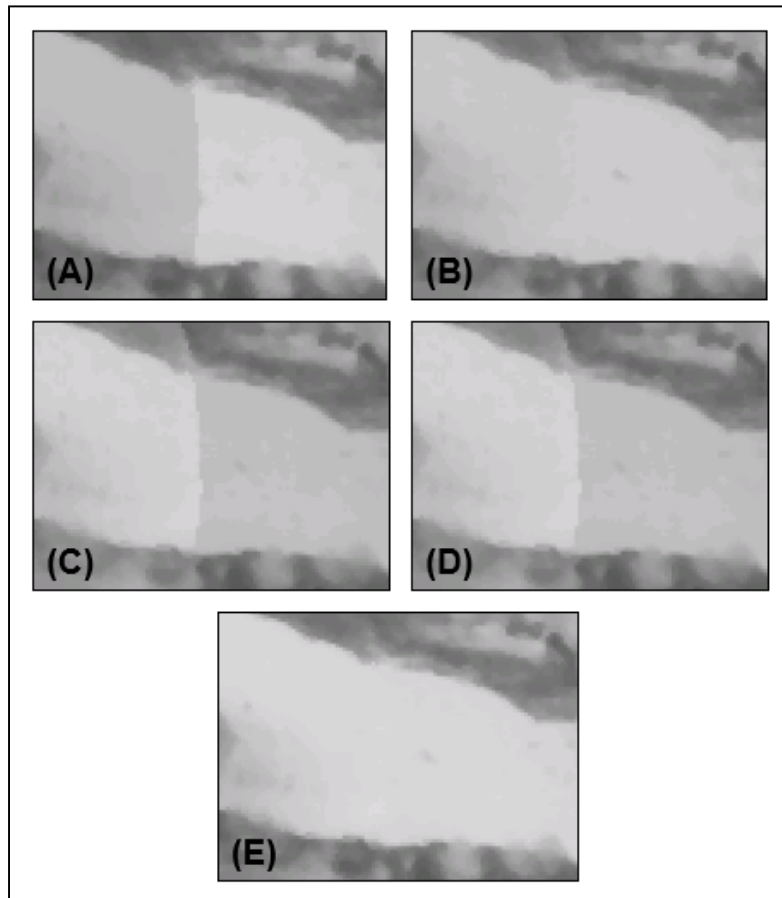


**Figure 4-8: A comparison of four different radiometric normalizations of a river sample. (A) The raw image, (B) Histogram Matching, (C) PIF-Based Linear Regression, (D) PIF-Based TS Regression, (E) NCSRS-Based Linear Regression.**

In a second example, a portion of a road is examined (Figure 4-9). Compared to the raw image (Figure 4-9A) the Histogram Matching method (Figure 4-9B) visually performs very well, barely showing any join line. On the other hand, the PIF-Based methods (Figure 4-9C, 4-9D) do not exhibit much visual improvement over the raw image, though the NCSRS-Based Linear Regression method (Figure 4-9E) does exhibit improved visual agreement.

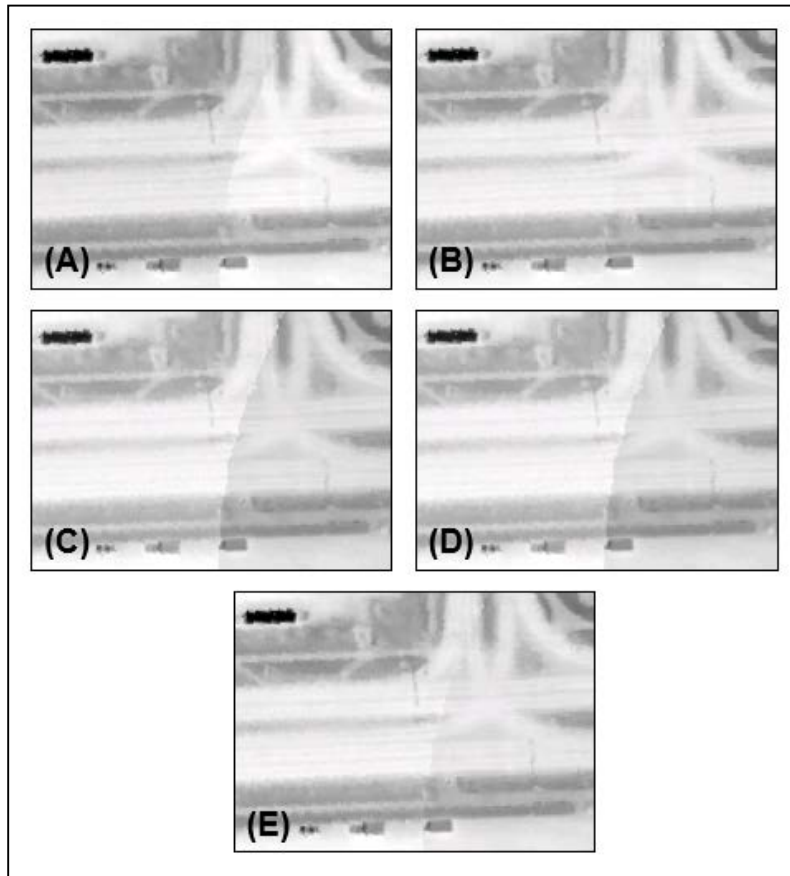


**Figure 4-9: A comparison of four different radiometric normalizations of a road sample. (A) The raw image, (B) Histogram Matching, (C) PIF-Based Linear Regression, (D) PIF-Based TS Regression, (E) NCSRS-Based Linear Regression.**

An example of a grassy field (Figure 4-10) shows similar results to those found for roads (Figure 4-9), where the PIF-Based methods (Figure 4-10C, 4-10D) exhibit limited improvement over the raw image (Figure 4-10A). However, Histogram Matching (Figure 4-10B) and NCSRS-Based Linear Regression (4-10E) show a strong visual agreement between the master and the slave images.

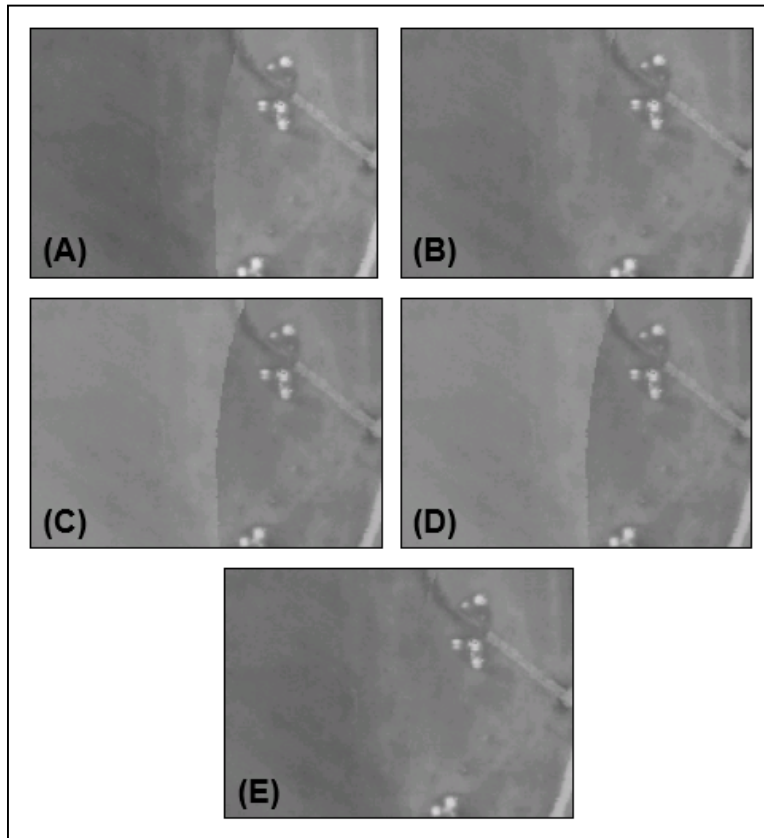


**Figure 4-10: A comparison of four different radiometric normalizations of a grassy field sample. (A) The raw image, (B) Histogram Matching, (C) PIF-Based Linear Regression, (D) PIF-Based TS Regression, (E) NCSRS-Based Linear Regression.**

Figure 4-11 displays a rooftop example where we see that that all methods visually improve the agreement between the master and the slave images. In this example, the PIF-Based methods visually perform better than the others with PIF-Based Linear Regression (4-11D) providing the best visual match.

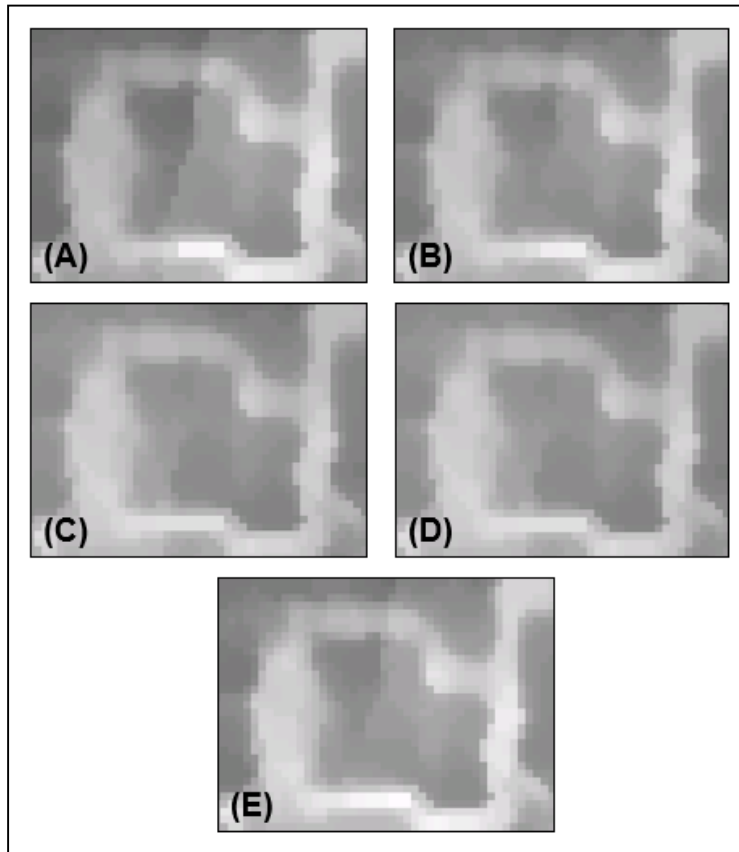


**Figure 4-11: A comparison of different radiometric normalizations of a single rooftop. (A) The raw image, (B) Histogram Matching, (C) PIF-Based Linear Regression, (D) PIF-Based TS Regression, (E) NCSRS-Based linear regression.**

Figure 4-12 shows an example of five color error maps (the absolute temperature differences between the master and normalized slave images) where dark areas represent no change zones ( $0^{\circ}\text{C}$  differences) and red areas represent where the highest temperature differences occurred. All maps are shown with the same range of differences (between 0 and  $2.7^{\circ}\text{C}$ ). From this composite figure, except for the PIF Based TS Regression (Figure 4-12F), all methods demonstrate visual improvement over the raw image (Figure 4-12C). Except for the top-right most portion of Figure 4-12C-G (which represents moist vegetation – possibly from a sprinkler system), the red areas that outline the border of house objects, are the result of geometric error between the master and the slave images rather than radiometric differences in building structures. In this

example, the error of all ground targets decreases with Histogram Matching (Figure 4-12D), PIF-Based Linear Regression (Figure 4-12E) and NCSRS-Based Linear Regression (Figure 4-12G), exhibits the largest reduction in RMSE.

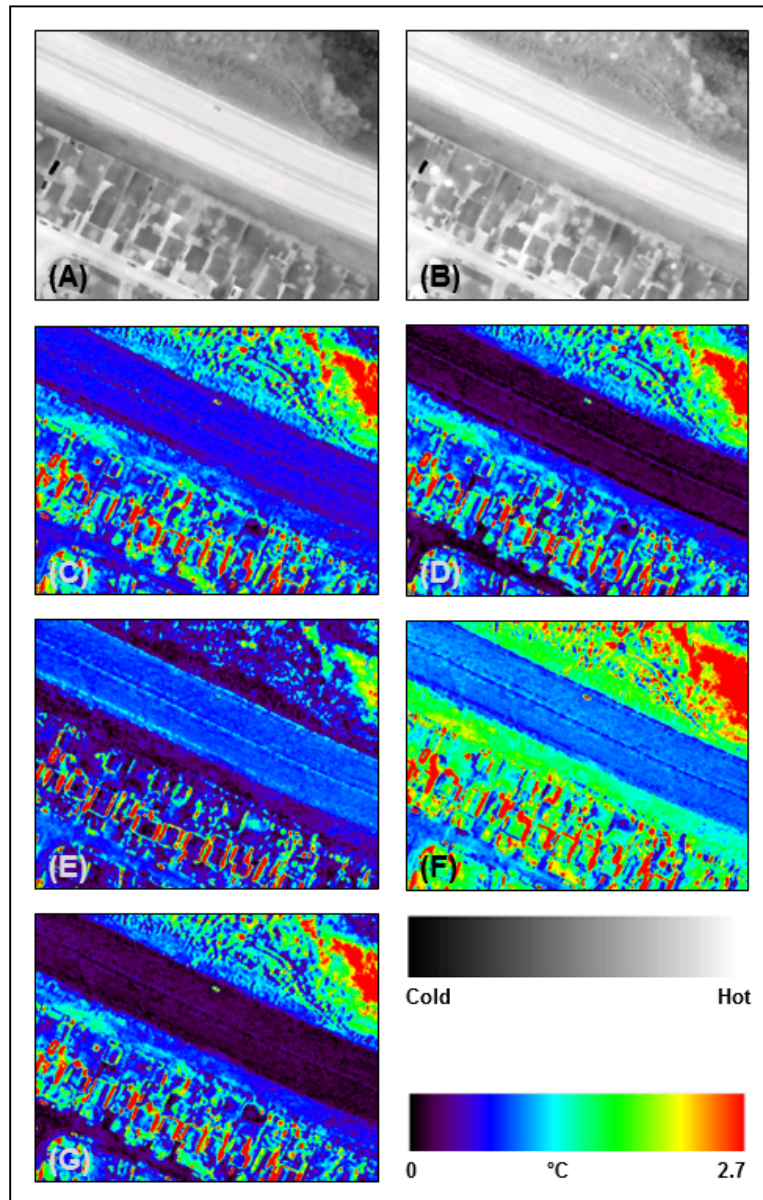


**Figure 4-12: Error maps of a sample location showing roads, rooftops and vegetation. (A) The sample area in the master image (dark areas are cold, bright areas are hot). (B) The corresponding area in the slave image. Error maps of (C) The raw slave image, (D) Histogram Matching (overall RMSE decreased by 52.4%), (E) PIF-Based Linear Regression (overall RMSE decrease by 39.1%), (F) PIF-Based TS Regression (overall RMSE increase by 24.5%), and (G) NCSRS-Based Linear Regression (overall RMSE decrease by 53.3%).**

#### 4.4.2 Statistical analysis

RMSEs were computed between the master and the slave (raw and normalized) images based on 2000 test samples representing four different landcover types including water, road, grass and rooftops. Considering the water class, the RMSE (Figure 4-13) is improved by all methods except PIF-based regression. Specifically, the NCSRS-Based Linear Regression and Histogram Matching methods are shown to perform the best, with their RMSEs reduced by 94.3% and 90.9% respectively.

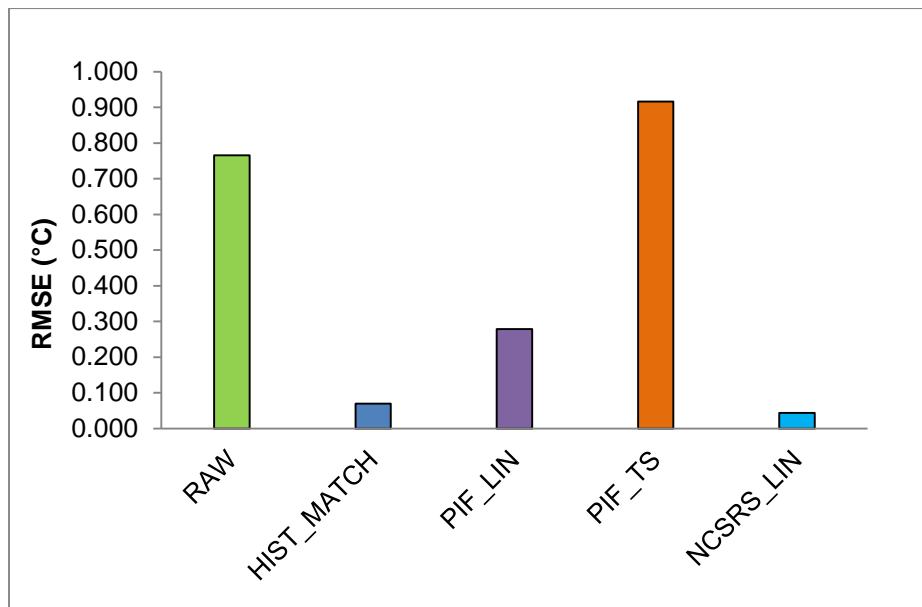


**Figure 4-13: RMSE results of water test samples derived from four RRN methods.**

For the road class (Figure 4-14), the Histogram Matching method performs best with its RMSE reduced by 34.02% (over the raw image), followed by NCSRS-Based Linear Regression which is decreased by 28.74%. Conversely, the PIF-Based TS Regression dramatically reduces agreement between the master and the slave images (by 312%).

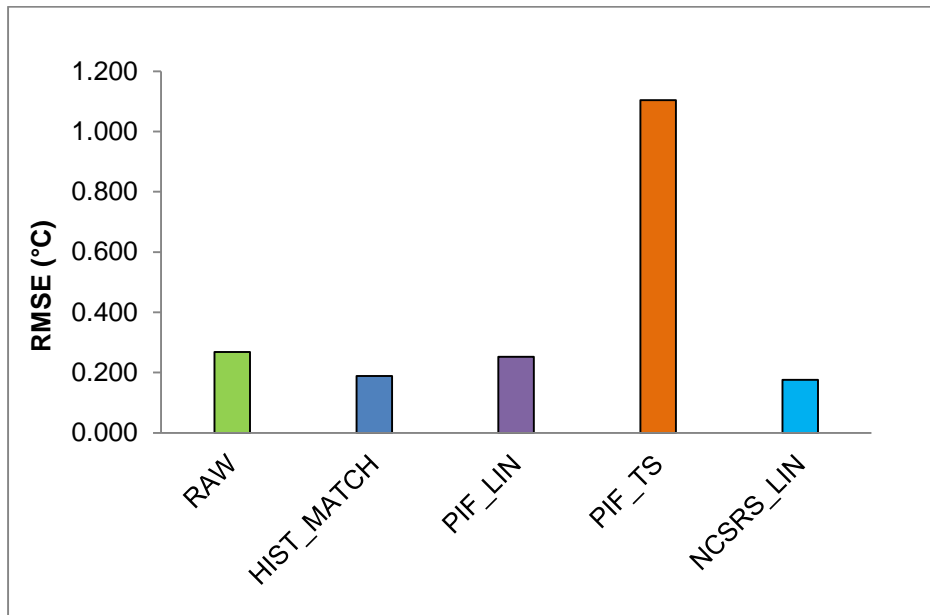


**Figure 4-14: RMSE results of road test samples derived from four RRN methods.**

In the case of grass (Figure 4-15), except for the PIF-Based TS Regression, all methods show significant improvement over the raw image. NCSRS-Based Linear Regression is observed to perform the best for grass (RMSE decreased 68.3%) followed by Histogram Matching (RMSE decreased 58.36%).

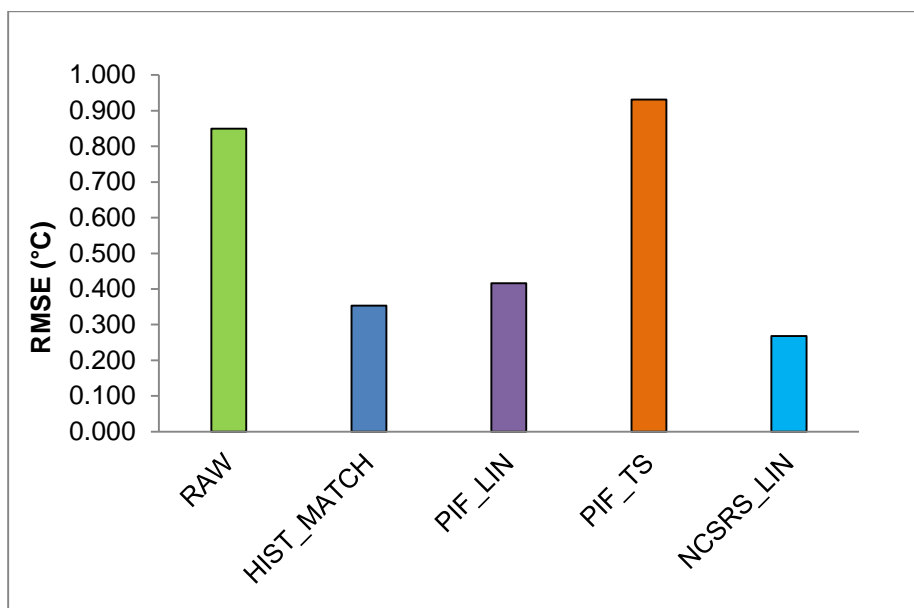


**Figure 4-15: RMSE results of grass test samples derived from four RRN methods.**

Rooftops display the highest RMSE (1.43 °C) in the raw image (Figure 4-16). This is expected as there are many different rooftop materials having different (uncorrected) emissivities, radiant temperatures (and different heating and cooling rates) accompanied by complex shapes and orientations. As a result, none of the methods dramatically improves the radiometric agreement of rooftops between the master and the slave images. However, the Histogram Matching method is observed to perform the best (RMSE decreased 32.8%) closely followed by the PIF-Based Linear Regression (RMSE decreased 30.1%).

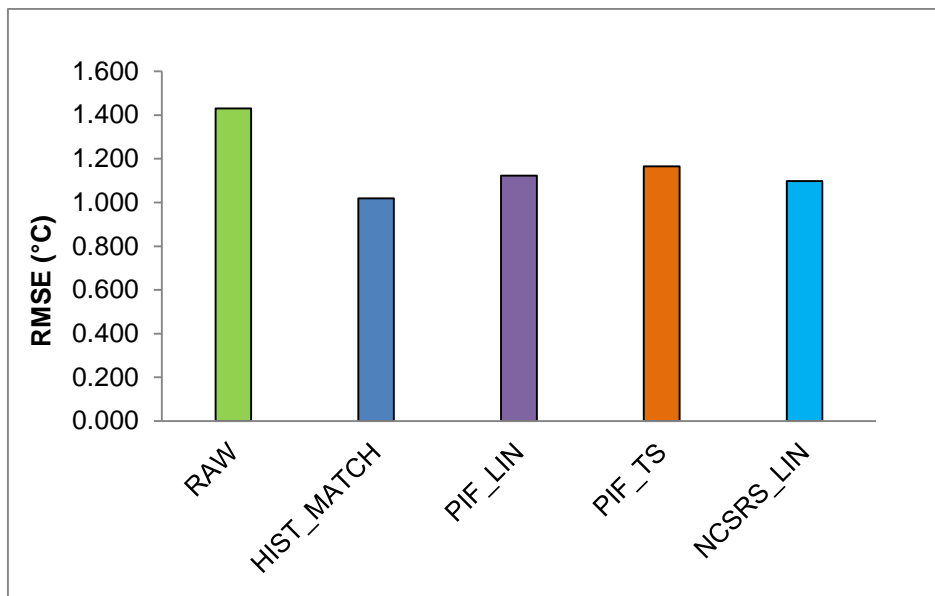


**Figure 4-16: RMSE results of roof-top test samples derived from four RRN methods.**

In summary, except for the PIF-Based TS Regression, all methods increase the radiometric agreement between the master and the slave images (Figure 4-17). PIF-Based TS Regression visually performs the worst. Conversely, NCSRS-Based Linear Regression is observed to perform the best with a 53.3% decrease in RMSE, which is only slightly better than Histogram Matching (52.4%). PIF-Based Linear Regression (39.1%) is also observed to perform well, compared to the raw images.

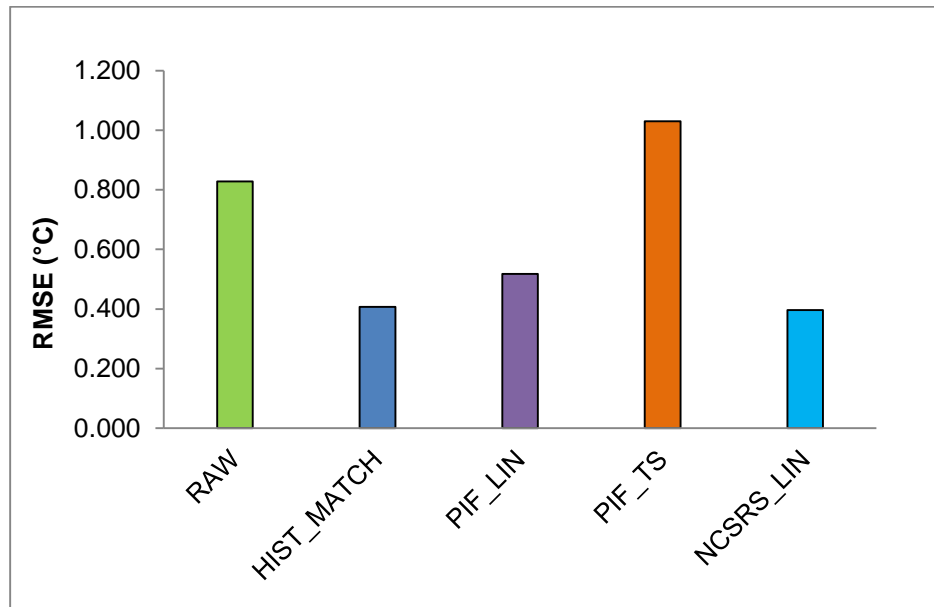


**Figure 4-17: Comparison of overall mean RMSE for four different relative radiometric normalization techniques and the original raw TIR image, based on 2000 test samples - representing four different landcover classes.**

#### 4.4.3 Computation time

An important criterion to consider in this evaluation is the computation time required to handle large datasets. Though this paper only describes evaluation of two flight lines (63.9 km<sup>2</sup>), the full City of Calgary airborne TIR scene (825 km<sup>2</sup>) is composed of 43 TABI-1800 flight lines representing some 600GB of data that requires processing into a mosaic. To assess the computation times of the different RRN methods, we used the same workstation (with an Intel® Core™ i7-2600, running Windows Server 2008 (64 bit) on a Quad Core CPU @ 3.40GHz, RAM: 16 GB) and applied all four algorithms on the same two TIR flight lines. All computer code was written in *Interactive Data Language* (IDL 8.0, 64 bit version<sup>27</sup>).

Among the radiometric normalization methods used in this paper, results show that the NCSRS-Based Linear Regression method was computationally the simplest technique requiring

---

<sup>27</sup> <http://www.exelisvis.com>.

the least amount of time to be executed (1.2 minutes). The second fastest method was Histogram Matching, which required 2.14 minutes to execute. The PIF-based methods required the manual collection of training samples. Thus, as the number of flight lines to be processed increases, this method becomes increasingly complicated to implement as new samples need to be manually collected within each overlapping section. In our case, once samples were manually collected, PIF-Based Linear Regression required 5.22 minutes to execute, while PIF-Based TS Regression required 22.4 minutes. TS Regression took longer to execute (22.4 minutes) as this technique creates pairwise slopes of the input data points that significantly increase the volume of computation [i.e.  $n$  data points have  $n*(n-1)/2$  pairs].

#### ***4.4.4 Ranking the evaluated methods***

To provide an overall operational perspective of the strengths and limitations of the different RRN methods, we ranked them (1: best, to 4: worst) according to four evaluation criteria: (i) computation time, (ii) ability to automate, (iii) visual assessment and (iv) statistical analysis (Table: 4-1). Based on these results, the NCSRS-Based Linear Regression method is the most appropriate method (of those tested) for applying relative radiometric normalization to H-res multitemporal TIR imagery. This is followed by Histogram Matching, PIF-Based Linear Regression and PIF-Based TS Regression. However, due to manual sample selection, these two PIF methods cannot be automatically operationalized within the current framework for large complex datasets.

**Table 4-1: Overall ranking of four RRN methods based on four different criteria (i-iv).**

RRN Methods	(i)	(ii)	(iii) Visual assessment				(iv) Statistical analysis				Final Rank
	Time (min)	Automation	Water	Road	Grass	Roof	Water	Road	Grass	Roof	
<b>Histogram Matching</b>	2.14	Yes	2	1	2	3	2	1	2	1	2
<b>PIF-Linear</b>	5.22	No	3	3	3	1	3	3	3	2	3
<b>PIF-TS</b>	22.4	No	4	4	4	2	4	4	4	4	4
<b>NCSRS-Linear</b>	1.2	Yes	1	2	1	4	1	2	1	3	1

#### 4.5 Conclusions

Absolute atmospheric correction and relative radiometric normalization refer to a family of radiometric normalization techniques. Absolute radiometric correction is intended to completely remove atmospheric effects from the imagery. It is computationally complex and requires a large amount of ancillary data (Jensen, 2005). On the other hand, relative radiometric normalization is computationally simple, easy to understand, requires less ancillary data and tends to increase the radiometric agreement between data collected at different times without explicitly removing atmospheric effects (Hall et al., 1991).

With increasing demand for H-res thermal imagery (Weng, 2009; 2012; Hay et al., 2011; Rahman et al., 2013) we recognize an emerging need to evaluate the utility of relative radiometric normalization (RRN) techniques applied to high-spatial and -spectral resolution (H-res) TIR imagery. To satisfy this need, we describe the evaluation of four different RRN techniques applied to two adjacent flight lines of H-res TABI-1800 imagery (each ~0.9 km wide x 35.5 km long at 50 cm spatial resolution and 0.05 °C thermal resolution) that were collected over The City of Calgary

on May 13, 2012 between 1:00 am - 2:00 am. These evaluated methods include: (i) Histogram Matching, (ii) Pseudo Invariant Feature (PIF) Based Linear Regression, (iii) PIF-Based Theil-Sen Regression, and (iv) No-Change Stratified Random Sample (NCSRS) Based Linear Regression - each of which were originally developed for the radiometric normalization of multispectral multitemporal imagery.

Results show that, except for PIF-Based TS Regression, all other methods improve the radiometric agreement between the master and the slave image. Specifically, the Root Mean Square Error (RMSE) results of four different landcover types [(i) water, (ii) road, (iii) grass, and (iv) rooftop] calculated between the master image and four different normalized images resulting from the four tested methods show that NCSRS Based Linear Regression produced the greatest reduction in RMSE relative to the raw image (53.3% RMSE reduction), followed closely by Histogram Matching (52.4% RMSE reduction). PIF-Based Linear Regression also showed improved agreement between the master and the slave images when compared to the raw image (39.1% RMSE reduction). However (as currently implemented in this research) the manual selection of features makes PIF-Based methods time consuming and unable to be automated, thus they are not operationally able to process large data volumes. Additionally, their computational complexity increases as the number of scenes to be radiometrically normalized increases. Conversely, Histogram Matching and NCSRS-Based Linear Regression methods can be completely automated, and are computationally fast, thus they can effectively be used in an operational setting to normalize large volumes of H-res TIR imagery.

The overall ranking of all four RRN methods based on their performance in four criteria: (i) computation time, (ii) ability to automate, (iii) visual assessment and (iv) statistical analysis, shows that NCSRS-Linear ranks highest, Histogram Matching is second and PIF-Linear is third.

Although PIF-TS is ranked fourth, we would strongly recommend not using it to normalize H-res TIR imagery. For some landcover classes it actually decreased the radiometric agreement between the master and the slave images by 312%.

## References

- Ben-Dor, E., and Saaroni, H. 1997. Airborne video thermal radiometry as a tool for monitoring microscale structures of the urban heat island. *International Journal of Remote Sensing*. 18:14, 3039-3053.
- Berk, A., Bernstein, L.S., and Robertson, D.C. 1989. MODTRAN: A Moderate Resolution Model for LOWTRA7N. AFGL-TR-89-0122, U.S. Air Force Geophysics Laboratory, Hanscom Air Force Base, Mass.
- Canty, M.J., Nielsen, A.A., and Schmidt, M. 2004. Automatic Radiometric Normalization of Multitemporal Satellite Imagery. *Remote Sensing of Environment*. 91:3-4, 441-451.
- Carnahan, W.H., and Larson, R.C. 1990. An analysis of an urban heat sink. *Remote Sensing of Environment*, 33, 65–71.
- Chen, G., Hay, G.J., Carvalho, L.M.T., and Wulder, M. 2012. Object Based Change Detection. *International Journal of Remote Sensing*. 33-14, 4434-4457.
- Du, Y., Teillet, P.M., and Cihlar, J. 2002. Radiometric normalization of multitemporal high-resolution satellite images with quality control for landcover change detection. *Remote Sensing of Environment*. 82:1, 123-134.
- Elvidge, C.D., m Yuan, D., Ridgeway, D.W., and Lunetta, R.S. 1995. Relative radiometric normalization of Landsat Multispectral Scanner (MSS) data using an automatic scattergram-controlled regression. *Photogrammetric Engineering and Remote Sensing*. 61:10, 1255-1260.
- Fernandes, R., and Leblanc, S.G., 2005. Parametric (modified least squares) and non-parametric (Theil–Sen) linear regressions for predicting biophysical parameters in the presence of measurement errors. *Remote Sensing of Environment*. 95:3, 303-316.

- French, A.N., Jacob, F., Anderson, M.C., Kustas, W.P., Timmermans, W., and Gieske, A. 2005. Surface energy fluxes with the Advanced Spaceborne Thermal Emission and Reflection radiometer ASTER at the Iowa 2002 SMACEX site USA. *Remote Sensing of Environment*, 99:1–2, 55–65.
- Furby S.L., and Campbell N.A. 2001. Calibrating images from different dates to ‘like-value’ digital counts. *Remote sensing of Environment*. 77, 186-196.
- Gallo, K.P., and Tarpley, J.D. 1996. The comparison of vegetation index and surface temperature composites for urban heat island analysis. *International Journal of Remote Sensing*. 17:15, 3071– 3076.
- Giglio, L., Csiszar, I., Restas, A., Morisette, J.T., Schroeder, W., Morton, D., and Justice, C.O. 2008. Active fire detection and characterization with the advanced spaceborne thermal emission and reflection radiometer ASTER, *Remote Sensing of Environment*. 112, 3055–3063.
- Gluch, R., Quattrochi, D.A., and Luvall, J.C. 2006. Multi-scale approach to urban thermal analysis, *Remote Sensing of Environment*. 104:2, 123–132.
- Gonzalez, J.E., Luvall, J.C., Rickman, D., Comarazamy, D., Picon, A.J., Harmsen, E.W., Parsiani, H., Ramirez, N., Vasquez, R.E., Williams, R., Waide, R.B., and Tepley, C.A. 2005. Urban heat islands developing in coastal tropical cities. *EOS*. 86, 397- 403.
- Hafner, J., and Kidder, S.Q. 1999. Urban heat island modeling in conjunction with satellite-derived surface/soil parameters. *Journal of Applied Meteorology*. 38, 448– 465.
- Hall, F.G, Sterbel, D.E., Nickeson, J.E., and Goetz, S.J. 1991. Radiometric rectification: toward a common radiometric response among multirate, multisensory images. *Remote Sensing of Environment*. 35, 11-27.

- Hay G.J., Kyle C., Hemachandran B., Chen G., Rahman M.M., Fung T.S., and Arvai J.L. 2011. Geospatial Technologies to Improve Urban Energy Efficiency. *Remote Sensing*. 3:7, 1380-1405.
- ITRES, 2011. <http://www.itres.com/> (Last accessed: October 25, 2013)
- Jensen, J.R. 2005. *Introductory Digital Image Processing: A Remote Sensing Perspective* 3rd, Upper Saddle River, NJ: Prentice-Hall.
- Jensen, J. R. 2007. *Remote Sensing of the Environment: An Earth Resource Perspective* 2nd edition. Upper Saddle River: Pearson Prentice Hall.
- Jolliffe, I.T. 1986. *Principal Component Analysis*. Springer-Verlag, New York.
- Lu, D., Mausel, P., Brondizio, E. and Moran, E. 2004. Change detection techniques. *International Journal of Remote Sensing*, 25, 2365–2407.
- Koltunov, A. and Ustin, S.L. 2007. Early fire detection using nonlinear multitemporal prediction of thermal imagery. *Remote Sensing of Environment*, 110:1, 18–28.
- Kneizys, F.X., Shettle, E.P., Gallery, W.O., Chetwynd, J.H., Abreu, L.W., Selby, J.E.A., Clough, S.A., and Fenn, R.W. 1983. *Atmospheric transmittance/ radiance: computer code LOWTRAN 6*. Air Force Geophysics Laboratory, Environmental Research Paper 846, Hanscom AFB, MA
- McGovern, E.A., Holden, N.M., Ward, S.M., and Collins, J.F. 2002. The radiometric normalization of multitemporal Thematic Mapper imagery of the midlands of Ireland – a case study. *International Journal of Remote Sensing*, 23:4, 751-766.
- Olthof, I., Poulitot, D., Fernandes, R., and Latifovic, R. 2005. Landsat-7 ETM+ radiometric normalization comparison for northern mapping applications. *Remote Sensing of Environment*. 95:3, 388-398.

- Peng, H., Wang, S. and Wang, X. 2008. Consistency and asymptotic distribution of the Theil-Sen estimator. *J. Statist. Plann. Infer.* 138, 1836-1850.
- Prakash, A. 2000. Thermal remote sensing: concepts, issues and applications. *International Archives of Photogrammetry and Remote Sensing*, XXXIII: B1.
- Quattrochi D.A., and Luvall, J.C. 1999. Thermal infrared remote sensing for analysis of landscape ecological processes: methods and applications. *Landscape Ecol.* 14, 577–598.
- Rahman, M.M., Hay, G.J., Couloigner, I., Hemachandran, B., and Tam, A. 2013. Geographic Object-Based Mosaicking (OBM) of High-resolution Thermal Airborne Imagery (TAB1-1800) to Improve the Interpretation of Urban Image Objects. *IEEE Geoscience and Remote Sensing Letters*, 10:4, 918-922
- Richards, J.R., and Jia, X. 2005. *Remote Sensing Digital Image Analysis: An Introduction*, Springer-Verlag. Berlin.
- Richter, R. and Schläpfer, D. 2011. *Atmospheric / Topographic Correction for Satellite Imagery*. DLR report DLR-IB 565-02/11, Wessling, Germany.
- Salvaggio, C. 1993. Radiometric scene normalization utilizing statistically invariant features, *Proceedings of Workshop Atmospheric Correction of Landsat Imagery*, Defense Landsat Program Office, [dates of workshop] Torrance, California, 155-159.
- Sen, P.K. 1968. Estimates of the regression coefficient Based on Kendall's tau. *J. Amer. Statist. Assoc.* 63, 1379-1389.
- Scheidt, S., Ramsey, M., and Lancaster, N. 2008. Radiometric normalization and image mosaic generation of ASTER thermal infrared data: An application to extensive sand sheets and dune fields. *Remote Sensing of Environment*, 112, 920-933.

- Schott, J.R., Salvaggio, C., and Vochok, W.J. 1988. Radiometric scene normalization using pseudo-invariant features. *Remote Sensing of Environment*, 26, 1–16.
- Streutker, D.R. 2002. A remote sensing study of the urban heat island of Houston, Texas, *International Journal of Remote Sensing*, 23:13, 2595-2608.
- Tarantola, A. and Valette, B. 1982. Generalized nonlinear inverse problems solved using the least squares criterion. *Rev. Geophys. Space Phys.* 20, 219-232.
- Theil, H. 1950. A rank-invariant method of linear and polynomial regression analysis, I. *Proc. Kon. Ned. Akad. v. Wetensch.* A53, 386-392.
- Tuominen, S., and Pekkarinen, A. 2004. Local radiometric correction of digital airborne photographs for multi-source forest inventory. *Remote Sensing of Environment*. 89:1, 78-82.
- Vermote, E., Tanre, D., Deuze, J.L., Herman, M., and Morcrette, J.J. 1995. 6S user guide version 1. NASA-Goddard Space Flight Center-Code 923, Greenbelt, MD 20771, USA.
- Voogt, J.A., and Grimmond, C.S.B. 2000. Modeling surface sensible heat flux using surface radiative temperatures in a simple urban area. *Journal of Applied Meteorology*. 39, 1679– 1699.
- Voogt, J.A., and Oke, T.R., 2003. Thermal remote sensing of urban climate. *Remote Sensing of Environment*. 86:3, 370-384.
- Wan, Z., and Li, Z.L. 1997. A physics-Based algorithm for retrieving land-surface emissivity and temperature from EOS/MODIS data. *IEEE Transactions on Geoscience and Remote Sensing* 35: 4, 980–996.
- Warner, T. A. and Chen, X. 2001. Normalization of Landsat thermal imagery for the effects of solar heating and topography. *International Journal of Remote Sensing*. 22:5, 773-788.

- Weng, Q. 2009. Thermal infrared remote sensing for urban climate and environmental studies: Methods, applications, and trends. *ISPRS Journal of Photogrammetry and Remote Sensing*, 64:4, 335-344.
- Weng, Q. 2012. Remote sensing of impervious surfaces in the urban areas: Requirements, methods, and trends. *Remote Sensing of Environment*, 117: 2. 34-49.
- Xing, Y., Jiang, Q.G., Qiao, Z.P., and Li, W.Q. 2010. Study of Relative Radiometric Normalization Based on Multitemporal ASTER Images. *Advanced Materials Research* 108:111, 190-194.
- Yang, X., and Lo, C.P. 2000. Relative radiometric normalization performance for change detection from multi-date satellite images. *Photogrammetric Engineering & Remote Sensing*. 66:8, 967-980.

## **Linking Chapters 4 and 5**

To mitigate the radiometric variability between airborne thermal infrared flight lines of a large urban area, Chapter 4 evaluated the applicability of four existing linear relative radiometric normalization techniques. While three of these methods show improved radiometric agreement between flight lines, we hypothesize that the use of non-linear techniques will further improve the radiometric agreement over the best linear methods, as the thermal behavior of urban features is naturally complex. To test this hypothesis, Chapter 5 evaluates two newly proposed polynomial-based relative radiometric normalization techniques compared with the two best linear techniques described in Chapter 4. These methods are tested over two adjacent flight lines ( $\sim 70 \text{ km}^2$ ) of TABI-1800 airborne data and the results of the four methods are visually and statistically compared.

## **Chapter Five: An assessment of polynomial regression techniques for relative radiometric normalization (RRN) of high-resolution multitemporal thermal infrared (TIR) imagery<sup>28</sup>**

### **5.1 Abstract**

Thermal Infrared (TIR) remote sensing scenes of urban environments are increasingly available from airborne and satellite platforms. However, limited access to high-spatial resolution (H-res ~1 m) TIR satellite images requires the use of TIR airborne sensors for mapping large complex urban surfaces, especially at micro-scales. A critical limitation of such H-res mapping is the need to acquire imagery in multiple flight lines and mosaic them together. This results in the same scene components (e.g. roads, buildings, green space and water) exhibiting different temperatures in different flight lines. To mitigate these effects, linear relative radiometric normalization (RRN) techniques are often applied. However, the earth's surface is composed of features whose thermal behaviour is characterized by complexity and non-linearity. Therefore, we hypothesize that non-linear RRN techniques should demonstrate increased radiometric agreement over similar linear techniques. To test this hypothesis, this paper evaluates two newly proposed non-linear regression techniques: (i) *Pseudo Invariant Features (PIF) Based Polynomial Regression*, and (ii) *No-Change Stratified Random Samples (NCSRS) Based Polynomial Regression* against the two best linear RRN techniques recently described in the literature. When applied to two adjacent flight lines (~ 70 km<sup>2</sup>) of (Thermal Airborne Broad-band Imager) TABI-1800 airborne data, visual and statistical results show that both new non-linear techniques improved radiometric agreement over the previously evaluated linear techniques. The new fully automated method NCSRS based Polynomial Regression provide the highest radiometric

---

<sup>28</sup> This work is co-authored by Rahman, M. M., Hay, G. J., Couloigner, I., Hemachandaran, B., and Bailin, J and was submitted (Sept 09, 2014) to a Special Issue (ISSN 2072-4292) of the open-source journal Remote Sensing, titled "*Recent Advances in Thermal Infrared Remote Sensing*". It is currently in review.

agreement between the master and the slave images, at ~ 56%. This is ~5% higher than the best previously evaluated linear technique (NCSRS based Linear Regression) recently described in the literature.

**Keywords:** Relative Radiometric Normalization, Thermal Infrared, Polynomial Regression, Airborne, High Resolution, TABI-1800.

## 5.2 Introduction

Remote sensing technology has been widely used to monitor the earth's surface from satellite, airborne, and UAV (Unnamed Aerial Vehicle) platforms, by recording the radiant energy emitted, or reflected from the earth's surface. However, these recorded images are strongly influenced by sun-surface-sensor geometry, sensor characteristics, atmospheric absorption and scattering, and microclimatic conditions that introduce noise within the sensor recorded radiant energy (Richards, 2013; Rahman et al., 2013). As the influence of these factors varies over time, a ground object viewed at different times, or by different sensors, tends to exhibit different sensor measurements. Thus, to use multiple data sets collected at different times, or from different sources, it is necessary to either retrieve the surface radiance by applying suitable atmospheric corrections to each image (i.e. *absolute* atmospheric correction), or normalize the radiance values to a standard set of conditions (i.e. *relative* radiometric normalization) (Hill and Sturm, 1991).

Absolute radiometric correction techniques aim to extract absolute surface radiances using sensor calibration parameters and atmospheric properties at the time of data acquisition (Du et al., 2002). However, it is often difficult to collect the necessary ancillary data (atmospheric characteristics and sensor calibration parameters) for absolute corrections due to the financial and logistical costs involved and the lack of historical weather data. On the other hand, *relative radiometric normalization* (RRN) techniques aim to reduce radiometric differences among multi-

temporal images by normalizing the radiometric properties of the slave<sup>29</sup> image(s) to the master<sup>30</sup> image, so that it appears as if all the images were acquired using the same sensor and under the same environmental conditions as the master (Hall et al., 1991).

RRN techniques are often preferred over absolute techniques because they require no in-situ data, and they are able to take into account all forms of noise generated from the atmosphere, sensor, microclimate and other possible sources in a single straightforward process (Chen et al., 2005). Therefore, relative techniques have been widely used for the normalization of multi-temporal multispectral imagery (Hall et al., 1991; Canty et al., 2004; Fernandes and Leblanc, 2005; Xing et al., 2010).

There are few reports of RRN techniques applied to airborne thermal infrared (TIR) imagery, as they are typically applied to satellite based TIR imagery acquired at moderate to low spatial resolution (60 meter to 1 km). For example, Warner and Chen (2001) applied RRN to suppress the effects of solar heating and topography in daytime Landsat TIR data. They evaluated three RRN techniques and concluded that all the methods were able to demonstrate improved radiometry of the original dataset. Scheidt et al. (2008) mosaicked night-time ASTER TIR data by automatically selecting Pseudo Invariant Features (PIFs) from scene overlaps and then fitting the PIFs in a linear regression model. More recently, Rahman et al. (2014) recognized the need to validate RRN techniques on H-res multi-temporal TIR imagery and evaluated four existing RRN techniques on multiple flight lines of TABI-1800 data (at a 50 cm spatial resolution). These are: (i) Histogram Matching, (ii) Pseudo Invariant Features (PIF) based Linear Regression, (iii) PIF

---

<sup>29</sup> Slave images (one or more images in an image-set) that are normalized to the master image.

<sup>30</sup> A master image is the reference image.

based Theil-Sen<sup>31</sup> Regression, and (iv) No-Change Stratified Random Sample (NCSRS) based Linear Regression. Their study showed that two of these evaluated methods (i and iv) visually and statistically performed better than the others, improving the radiometric agreement between multi-temporal images by ~50%.

Each of the RRN techniques described in these studies was linear in nature. That is, for the purpose of simplifying analysis, it was assumed that the thermal properties of the different surface types were linearly correlated. However, in reality, the earth's surface is a complex mixture of natural and anthropogenic features exhibiting very different, often non-linear, thermal properties (Kahle et al., 1976). For example, if water and rock are heated for a constant time under identical environmental settings, the rock temperature will rise more quickly than the water due to its lower thermal capacity (Jensen, 2007). Oke (1981) conducted an extensive study on the thermal characteristics of different earth surfaces. His results demonstrated a clear difference in the cooling rates of different surfaces including snow, peat soil, sandy soil, clay soil, water, rocks, farmlands, and woods from sunset to sunrise. A more recent study (Chudnovsky et al., 2004) also examined the daytime thermal behavior of urban surfaces, which revealed nonlinear thermal relationships among different construction materials over time, including granulite, mixed asphalt, bright concrete, and dark concrete. Thus, assuming a simple linear thermal relationship among different types of complex surfaces is expected to produce sub-optimal results. Consequently, we hypothesize that non-linear RRN techniques should demonstrate increased radiometric agreement over complex urban surfaces, compared to similar linear techniques. To test this hypothesis, the

---

<sup>31</sup> The Theil-Sen (Theil, 1950; Sen, 1968) estimator is a robust linear regression model that uses the median of pairwise slopes as an estimator of the slope parameter of the correlation between two datasets (Peng et al., 2008).

objective of this paper is to evaluate the two most suitable linear techniques for the RRN of airborne TIR imagery as recently described by Rahman et al. (2014) as compared to two newly proposed polynomial techniques that are expected to better suit the thermal complexity of urban surfaces, and to evaluate them visually and statistically. To achieve this objective, the following section (Section 5.3) describes the study area, datasets and the RRN techniques used, followed by the a discussion of the results (Section 5.4) and lessons learned (Section 5.5).

### **5.3 Methods**

This section introduces the study area and the dataset. Then, the Relative Radiometric Normalization (RRN) techniques evaluated in the study are described.

#### ***5.3.1 Study area and dataset***

The study area of this research represents a ~ 70 km<sup>2</sup> portion of The City of Calgary, Alberta, Canada composed of two adjacent TABI-1800 TIR flight lines (Figure 5-1A), each ~0.9 km X 39 km with ~30% overlap between them. The City of Calgary is a modern metropolitan center, composed of a variety of urban landscape features (Figure 5-1B). The TABI-1800 (Thermal Airborne Broadband Imager) is a H-res TIR sensor (1 channel) that collects data within the 3.7 - 4.8  $\mu\text{m}$  spectral range. It has an IFOV of 0.405 milliradians and a FOV of  $\pm 20$  degrees with a 14-bit dynamic range. The sensor's radiometric accuracy is 0.05 °C and it is able to collect data at 90-100 frames per second (ITRES, 2014). The data for this project were acquired between 2:00 am and 3:00 am on May 13, 2012 at a 50 cm spatial resolution, and were ortho-rectified using a 10 m DEM (Digital Elevation Model). The reported geometric accuracy of the dataset is  $\pm 1$  m.

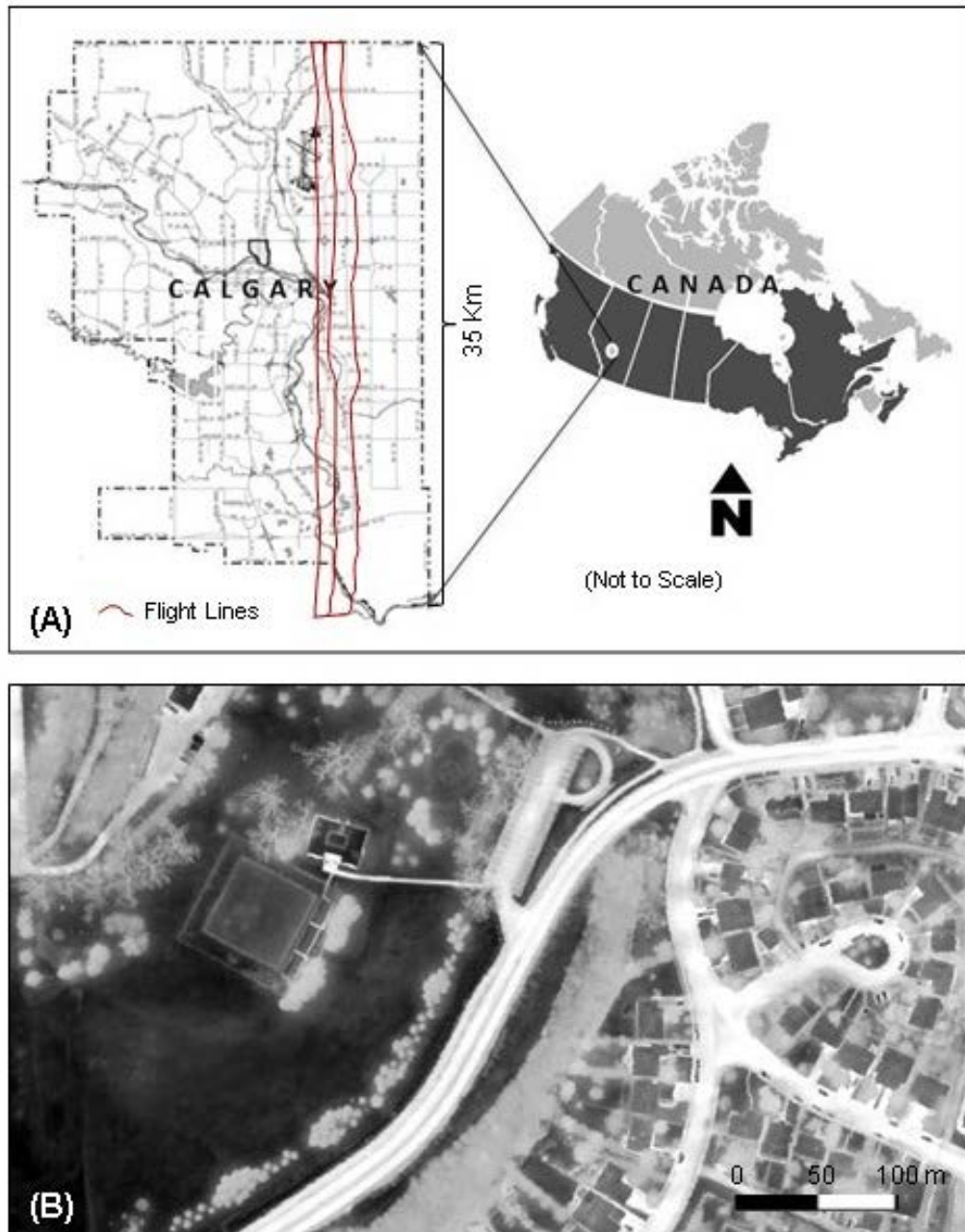


**Figure 5-1: (A) A map of The City of Calgary, displaying the study area, and the location of the two TABI-1800 flight lines used in this study. (B) An example of TABI-1800 imagery within the study area, detailing the urban complexity resulting from roads, buildings, trees, green space, etc. Bright locations are warm, dark locations are cool.**

### **5.3.2 Relative radiometric normalization**

RRN techniques consider one scene from a multi-temporal image-set as the reference (master) and normalize the others (slaves) to it. To radiometrically normalize the thermal flight lines, we consider the earlier acquired image as the master, and the later image as the slave. The RRN methods evaluated in this study are: (i) Histogram Matching (HM), (ii) Pseudo Invariant Feature Based Polynomial Regression (PIF\_Poly), (iii) No-Change Stratified Random Sample Based Linear Regression (NCSRS\_Lin), and (iv) No-Change Stratified Random Sample Based Polynomial Regression (NCSRS\_Poly). All algorithms were written in Interactive Data Language (IDL 8.0), applied to the same datasets using the same workstation<sup>32</sup>.

As there is only a maximum of 30% overlap between the master and the slave images, we first extract the overlap sections from both flight lines, which represents the same land area observed at two different acquisition times, then develop all RRN methods based on these overlaps, and apply the RRN methods to the entire slave flight line, thus, normalizing it to the master. The RRN methods used in this study are briefly described below.

#### **5.3.2.1 Histogram matching**

Histogram Matching (HM) is described as matching the histogram of one image to that of another image so that their apparent distribution of DN values becomes more similar (Richards, 1999). The simplest way to perform Histogram Matching is to create the histogram of the reference and the slave images, then calculate the mean difference using Equation 5-1, and use it to normalize the slave histogram to the master (Rahman et al., 2014). Figure 5-2 displays a hypothetical example of the HM technique.

---

<sup>32</sup> An Intel® Core™ i7-2600, running Windows Server 2008 (64 bit) on a Quad Core CPU @ 3.40GHz, RAM: 16 GB.

$$MD = \frac{1}{n} \sum_{i=1}^n (y_i - x_i) \quad (\text{Equation 5-1})$$

Where

$MD$  = mean difference,

$n$  = number of pixels,

$x_i$  = value of pixel  $i$  in the slave image, and

$y_i$  = value of pixel  $i$  in the master image.

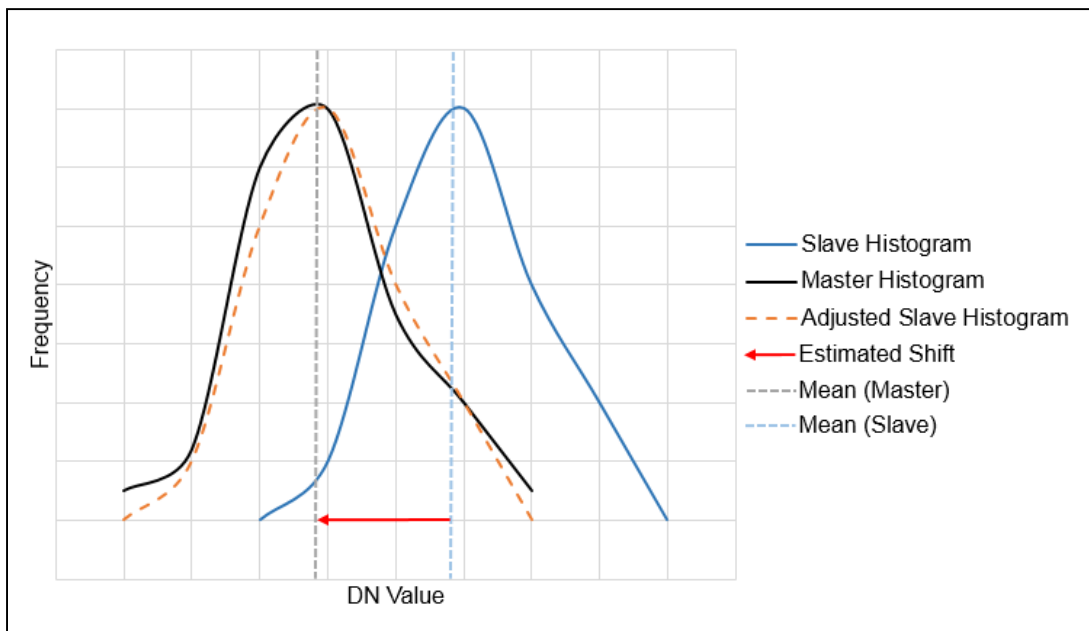


**Figure 5-2: A hypothetical example of radiometric normalization using Histogram Matching technique.**

This HM definition is intended to work for scenes composed of the same surface area (100% overlap), but collected at different times using different sensors. However, our study area is represented by two adjacent flight lines having only a ~30% overlap. Therefore, the mean difference is calculated based exclusively on the histograms of the overlap sections between the master and the slave images. Then, normalization is applied to the entire slave image – based on the defined difference in this 30% overlap.

### 5.3.2.2 Pseudo invariant feature (PIF) based polynomial regression

Pseudo Invariant Features (PIFs) are defined as objects whose electromagnetic properties (reflection, absorption, and emission) are nearly constant for the imaging conditions, and which are independent of seasonal, or biological cycles (Schott et al., 1988). Such features are commonly used as references for the relative radiometric normalization of multi-temporal imagery (Schott et al., 1988; Hall et al., 1991; Salvaggio, 1993; Rahman et al., 2014).

In this study, we used four types of PIFs that were expected to be consistent during the acquisition of both flight lines: (i) grass, (ii) rooftop, (iii) river water, and (iv) road, each of which covers a broad (non-overlapping) range of temperatures. In general, grass was cooler than most of the features within each flight line, rooftop and water was warmer and road was the hottest. We manually collected ~2000 training sample points (~500 points for each type of landcover) within the overlap sections. These points were then plotted (Figure 5-3) and a 6<sup>th</sup> order polynomial regression equation (Equation 5-2) was developed from the scatterplot, which was later used to normalize the slave image to the master. To determine which order polynomial equation is most suitable,  $R^2$  values from 2<sup>nd</sup> to 8<sup>th</sup> order polynomial functions were evaluated. Starting from the lowest order, a comparison with the next higher order equation's  $R^2$  value is made. If a significant increase<sup>33</sup> in  $R^2$  is observed then the next order polynomial is calculated. If this does not lead to a significant increase in  $R^2$ , the previous order is chosen as the most appropriate polynomial for that dataset.

---

<sup>33</sup> greater than 0.1 is defined as significant improvement

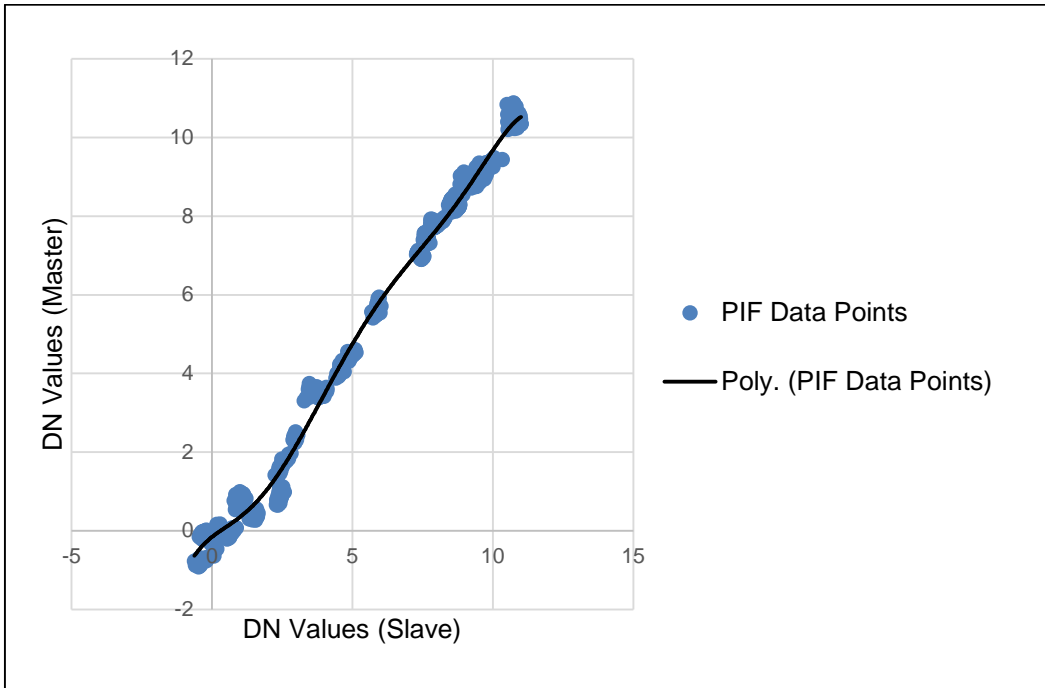


**Figure 5-3: Scatterplot of Pseudo Invariant Features (PIFs) selected within the overlap of the master and the slave images. These PIFs represent a combination of four landcover classes (grass, rooftop, water, and road), which are shown modeled with a 6<sup>th</sup> order polynomial trend line (black).**

$$y = -0.0001x^6 + 0.0033x^5 - 0.0387x^4 + 0.1796x^3 - 0.2020x^2 + 0.5659x + 0.1583$$

$$R^2 = 0.99 \quad \text{(Equation 5-2)}$$

### 5.3.2.3 No-change stratified random sample (NCSRS) based regressions

The manual selection of PIFs is subject to user bias and errors and can be difficult, time consuming and costly to complete correctly, especially in areas where the analyst may have limited local field experience. To overcome these issues, a number of studies describe using automatic techniques to identify no-change sets (i.e. invariant features) from which reference samples are selected for relative radiometric normalization (Hall et al., 1991; Elvidge et al. 1995; Canty et al., 2004; Rahman et al., 2014). In this paper, we apply the method described by Rahman et al. (2014), which used *Mean* and *Standard Deviation (SD)* to automatically identify the no-change set within the flight line overlap. This required producing an image difference map of the overlap sections

by subtracting the slave from the master overlap, then creating a histogram from this difference map.

As these flight lines were collected during a calm night only ~10-20 minutes apart, we assume that the temperature of different landcover types will not be significantly altered. Consequently, any abrupt changes in surface temperature during this brief time are considered as noise and are masked out of the image difference histogram using a heuristically derived measure of SD<sup>34</sup>. This SD measure corresponds to data points (DNs) beyond mean  $\pm$  3SD, which has been extensively shown to work over different cover types (Rahman et al., 2014). To collect representative samples from the remaining image, the master and slave overlap DN pairs were sorted in an ascending order and a random pair was selected from each 500 point bin (0.2% of the population), in this case totaling 42,280 sample points. These data were sorted to cover the entire radiometric range of the overlap image, so that different landcover types with different temperatures are included in the samples. The selected samples were then plotted (Figure 5-4) to develop (i) a linear and (ii) a polynomial regression equation (Equation 5-3 and Equation 5-4). The appropriate order of polynomial equation is independently determined using the iterative technique described in Section 5.2.2.2. These equations were then individually applied over the slave image to radiometrically normalize it to the master image.

---

<sup>34</sup> Due to the airborne nature of these data, we note that this activity also compensates for areas within the scene that may have localized geometry issues greater than the reported geometric error ( $\pm$  1 m) of the post-processed data. "... Compensates for..." means that areas with large geometric error are expected to show high variance in the change image, thus these areas are not included in the analysis.

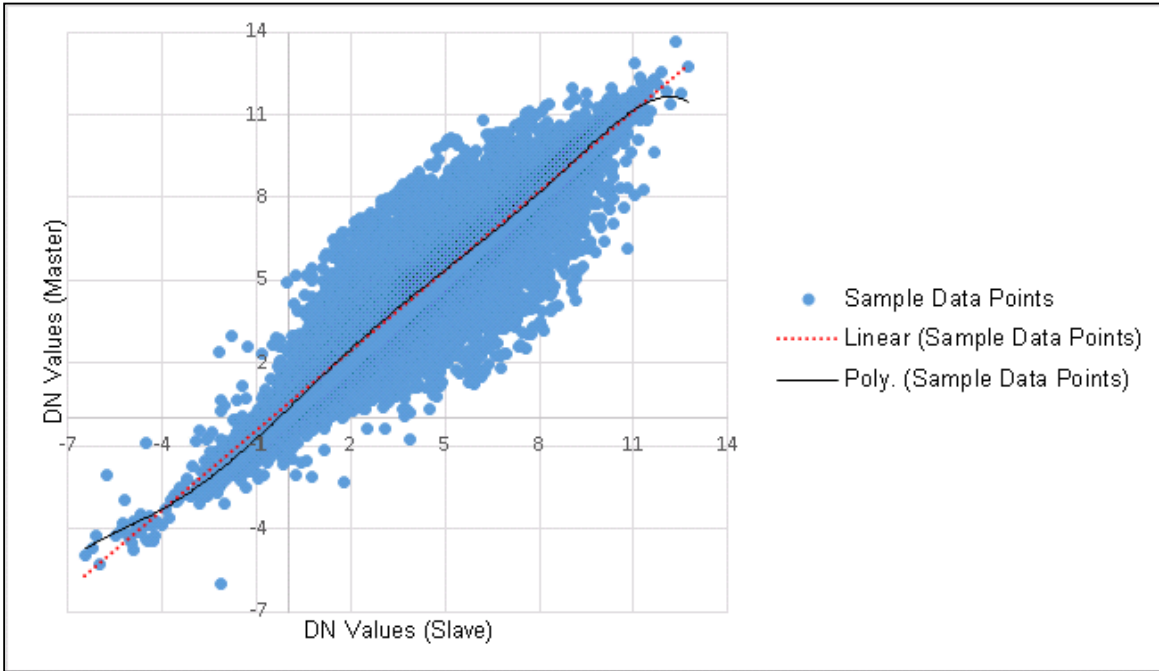


**Figure 5-4: Scatterplot of No-Change Stratified Random Samples (NCSRS) with a 6th order polynomial trend line (black) and a linear trend line (red dotted) between the master and the slave images**

$$y = 0.9124x + 0.334 \quad (R^2 = 0.88) \quad \text{(Equation 5-3)}$$

$$y = 0.000004x^6 - 0.00009x^5 + 0.00017x^4 + 0.00696x^3 - 0.3294x^2 + 0.95803x - 0.1189 \quad (R^2 = 0.93) \quad \text{(Equation 5-4)}$$

#### 5.3.2.4 Validation of the results using root mean square error (RMSE)

It is expected that the radiometric (temperature) difference between identical features in the master and the slave flight lines within the overlap will decrease after performing normalization. To test this, we randomly selected 2000 test points from the four major landcover types present in the overlap sections including grass, rooftop, water and road (~500 points for each landcover), then calculated the *Root Mean Square Error* (RMSE) of the selected points for all presented methods using Equation 5-5.

$$RMSE = \sqrt{\frac{\sum_1^n (DN_{master} - DN_{slave})^2}{n}} \quad \text{(Equation 5-5)}$$

## 5.4 Results and discussions

### 5.4.1 Visual assessment

Visual assessment is a straightforward way to judge the performance of the evaluated methods. In so doing, the master and the slave flight lines were joined and features along the mosaic line were assessed. If the visual differences between the master and the normalized slave images are smaller than that of the master and the raw slave images, the normalized image can be considered as radiometrically adjusted to the reference image.

A visual assessment of grass, road, water and rooftop samples illustrated in Figure 5-5, which shows that each tested method improves the radiometric agreement between the master and the slave images compared to the raw image. However, the degree of normalization varies depending on the method used and the landcover type assessed. Specifically:

- HM appears to perform very well for road and water, but performs only moderately well for grass and rooftop.
- PIF\_Poly performs well for road and water, moderately well for grass, but it does not perform well for rooftop.
- NCSRS\_Lin performs very well for water and moderately well for road, grass and rooftop.
- NCSRS\_Poly performs very well for road and water and well for grass and rooftop. Though subjective, we further suggest that grass and rooftop visually appear best modeled by this method.

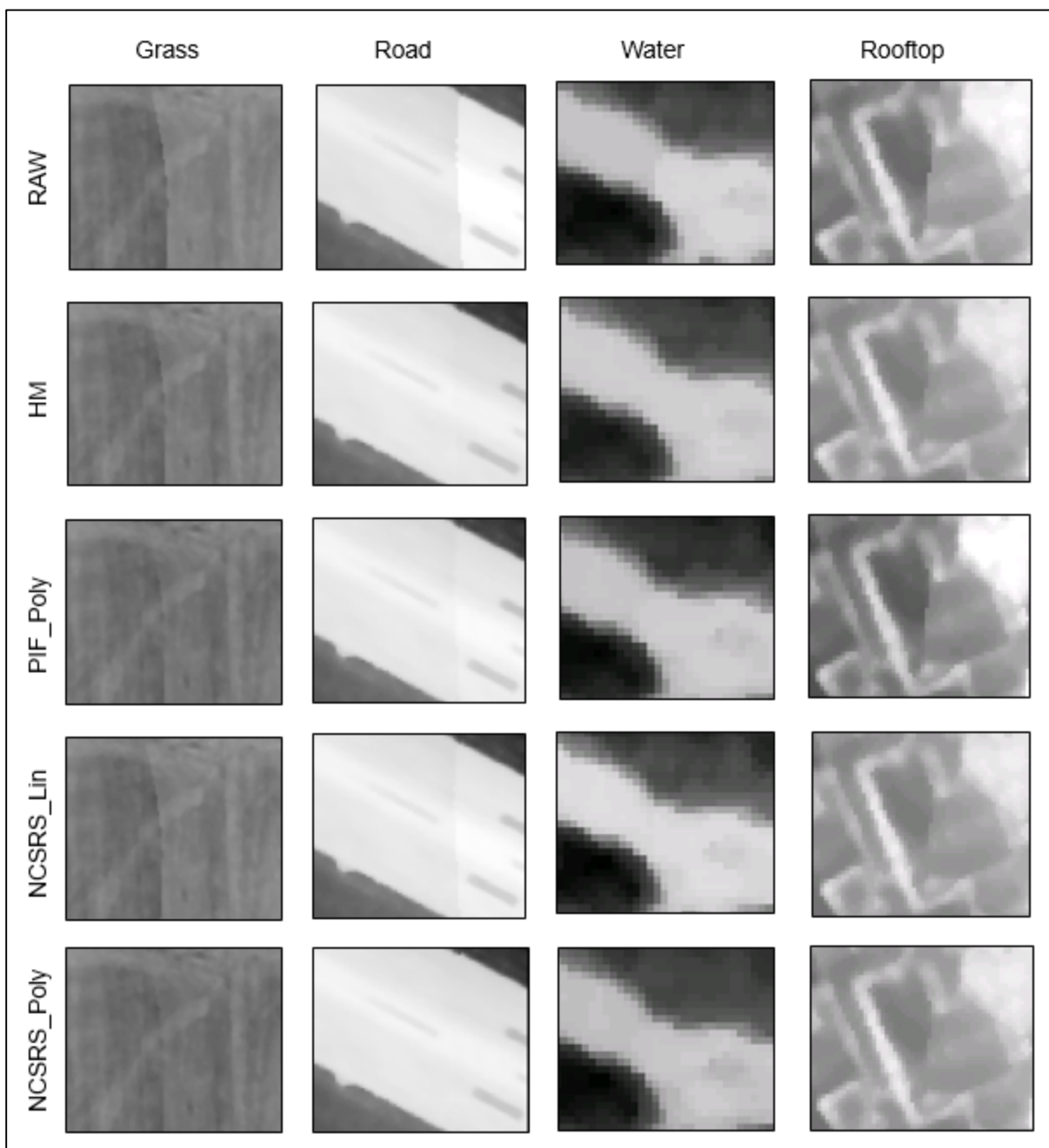


**Figure 5-5: Visual examples of four different relative radiometric normalization methods applied along the mosaic join line of four different landcover types (grass, road, water and rooftop).**

In general, the radiometric error of geographically simple features like road and water are visually reduced by all methods – this in part can be explained by their high thermal inertia – which

results in low within class variability regardless of the time that they were acquired in either flight line.

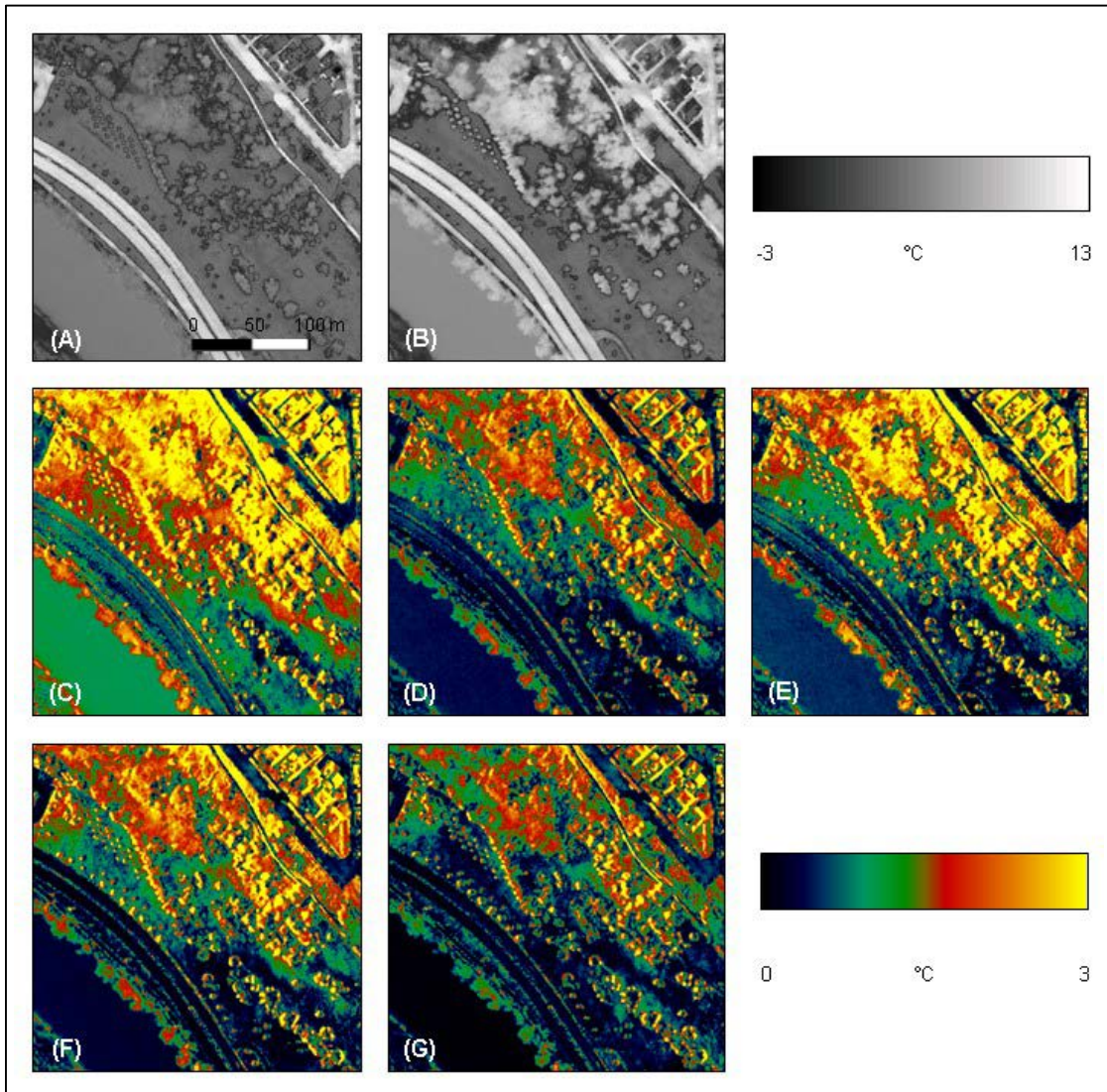
While the river water class is part of a dynamic system, its night-time temperature fluctuates very little as its source is regulated by high-mountain snow melt<sup>35</sup>. However, complex features like grass and rooftops are not well modeled by most of the evaluated methods. This in part can be explained by their complex and variable nature. That is, different types of grass will exhibit different night-time evapotranspiration rates, and the temperature of different roof sections (even for the same building structure) can be differentially heated at different times during the night as they respond to variable local microclimatic differences in temperature and humidity, two attributes typically assessed by modern in-home thermostats. At a broader community scale, rooftops can further be considered a highly variable landcover feature, as they are composed of numerous materials, many of which have different emissivity values that need to be corrected for after radiometric normalization in order to convert their relative temperature values to true kinetic temperatures (Rahman et al., 2013, 2014). As a consequence, a small constant difference in ambient temperature may result in several degrees of difference in roofs composed of different materials when they are not corrected for emissivity.

Figure 5-6 provides a visual example of how the four evaluated relative radiometric normalization techniques reduce the thermal variability between the master and slave image(s) for four landcover types. Figures 5-6A (the master) and 5-6B (the slave) represent corresponding grey-scale TABI image-samples of a small area located within the flight line overlap that is predominantly composed of: vegetation, roads, a river (water-body) and roofs. In both the master

---

<sup>35</sup> The City of Calgary is located ~80 km east to the front ranges of Canadian Rockies.

and slave TIR sub-images, grass (smooth lower right) and roofs (top right corner) appear cool (mid-dark grey), the river (lower left diagonal feature) and trees (textured blobs) are moderately warm (light grey), while roads and paths are the hottest (white). In Figure 5-6C, the strongest temperature difference between the master and the uncorrected slave image appears yellow ( $+3^{\circ}\text{C}$ ) for trees and rooftops. However after radiometric normalization, these differences and those of other features visually decrease (Figure 5-6D-G). For example, water and road appear well modeled by most of the methods, displaying a minimum difference (black, or blue  $\approx 0-1^{\circ}\text{C}$ ) between the master and the normalized slave images. Overall, rooftops and trees display the highest differences (yellow  $\approx +3^{\circ}\text{C}$ ), which continue over different spatial extents in all slave images (Figure 5-6C-G). Upon more detailed visual inspection, these rooftops and trees represented by a yellow color in the figure appear to be due to geometric shift. This is especially noticeable as yellow regions along the edges of buildings (see top right Figure 5-6D-G), on tree tops and along paths. These errors are not completely removed by any of the methods. However based on a visual assessment of the pseudo coloured temperature differences for all the RRN samples in Figure 6, NCSRS\_Poly (Figure 5-6G) visually appears to perform the best for all four landcover types, closely followed by HM and NCSRS\_Lin methods.



**Figure 5-6: A visual example of how relative radiometric normalization decreases the radiometric variability between flight lines. (A) A sample area from the master image. (B) The same area from the slave image. Absolute image difference (C) between the master and the uncorrected slave image, and between the master and the normalized slave images resulting from (D) HM, (E) PIF\_Poly, (F) NCSRS\_Lin, and (G) NCSRS\_Poly.**

#### **5.4.2 Statistical analysis**

As noted in Section 5.3.2.4, the Root Mean Square Error (RMSE) was used to define the statistical agreement between the normalized slave images and the master image. This required collecting 2000 stratified random sample points within the overlap that represent four different

landcover types over a wide range of temperatures. These include: (i) grass, (ii) rooftop, (iii) water and (iv) road. Table 5-1 summarizes the RMSEs calculated for these cover types.

**Table 5-1: The overall RMSE of four different landcover types, for each of the four different relative radiometric normalization methods evaluated in this study. Bold values represent the lowest RMSE for each class and overall.**

Landcover Type	RMSE (°C)				
	Slave	HM	PIF_Poly	NCSRS_Lin	NCSRS_Poly
<b>Grass</b>	0.420	0.236	0.227	0.193	<b>0.163</b>
<b>Rooftop</b>	0.586	0.436	0.452	0.371	<b>0.322</b>
<b>Water</b>	0.216	<b>0.106</b>	0.108	0.130	0.113
<b>Road</b>	0.201	<b>0.097</b>	0.128	0.122	0.123
<i>Overall*</i>	0.356	0.194	0.210	0.173	<b>0.159</b>

\*Mean of RMSEs of all selected test samples for different landcover types

In general, all methods show a reduced radiometric variation between the master and the slave images. Table 5-1 shows that complex features like rooftops and grass have higher RMSE values than other features in the uncorrected slave image. This is understandable as different roofing materials are used in Calgary including asphalt shingles, clay tiles, cedar, tar and gravel, wood, concrete, fibreglass, vinyl shingles etc., each of which has different thermal capacities, conductivity and emissivity. As a result, it is challenging to radiometrically normalize rooftops with each of the methods. Similarly, the grass class also has a higher RMSE in the uncorrected slave image, potentially due to the various species compositions, each with varying allometric and morphometric characteristics, and the varying amount of moisture in the background soil (Friedel and Davis, 1994). The other two features (road and water) are relatively simple, and exhibit relatively lower RMSE values in the slave image. They are also reasonably well modeled by all methods, resulting in decreased RMSE values (~50%). However, the complex feature classes

(rooftop and grass) are best modeled only by the NCSRS based methods, with the NCSRS based polynomial technique providing the lowest overall RMSE.

Figure 5-7 illustrates the scatterplots and resulting trend-lines between the master and the slave images - before (Figure 5-7A) and after (Figure 5-7B-E) normalization. The blue lines represent the linear trend lines, while the red dashed lines illustrate the expected trend of each dataset at perfect radiometric agreement. Scatterplots can be used to describe various correlations between different variables. The data cloud follows a 45° diagonal line (i.e. the red dotted line in Figure 5-7A-E), which indicates that the datasets are not only highly correlated - but also that their DN values are very close to each other.

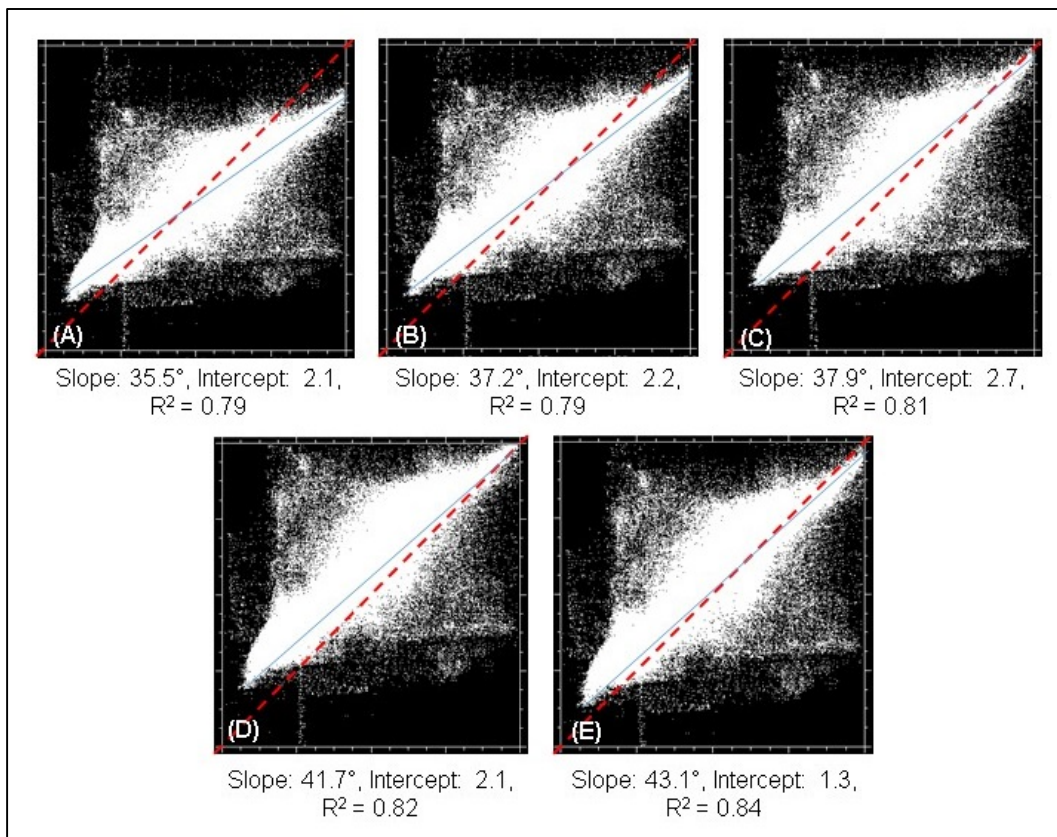


**Figure 5-7: (A) A comparison of the scatterplot between the original master and the slave images, and after applying four normalization methods: (B) HM, (C) PIF\_Poly, (D) NCSRS\_LIN, and (E) NCSRS\_Poly. The blue lines describe the data trend line, while the red dashed lines show the expected trend(s) at perfect radiometric agreement.**

In a perfect scenario, if two datasets represent the same features, their slope should be  $45^\circ$  and their intercept should be at 0 in the scatterplot. In the scatterplot of the raw images (Figure 5-7A), the slope is  $35.5^\circ$  and the intercept is 2.1. However, each of the normalized scatterplots (Figure 5-7B-E) improves the slope between the master and the slave, and most of the methods improve both the intercept and the slope. Of those methods tested, the scatterplot results (Figure 5-7A-E) show that the NCSRS\_Poly trendline (Figure 5-7E) is statistically the closest to the red line with a slope of  $43.1^\circ$ , an intercept of 1.3 and an  $R^2$  of 0.84. Thus it represents the best performing normalization method, followed by NCSRS\_Lin (Figure 5-7D), HM (Figure 5-7B), then PIF\_poly (Figure 5-7C).

#### 5.4.2.1 A comparison of automatic vs. manual methods

When automatic methods (HM, NCSRS\_LIN and NCSRS\_Poly) are compared against the manual method (PIF\_Poly), Table 5-1 results demonstrate that automated methods are able to more efficiently process large volumes of data, while maintaining a higher level of accuracy (i.e. a low RMSE). Figure 5-5 and Table 5-1 further show that although the (PIF\_Poly) method performed moderately well for grass, road and water, it failed to improve the radiometric agreement for rooftops. Also, the required manual collection of samples is time consuming and subject to human error.

#### 5.4.2.2 A comparison of linear vs. polynomial methods

In the introduction, we hypothesized that nonlinear (polynomial) RRN techniques are better suited to model the temperature variability of complex urban features in H-res TIR imagery than corresponding linear techniques. In this section, we test this hypothesis by comparing only the NCSRS based linear and polynomial RRN techniques, as they both used the same automatically generated samples in their corresponding regression equations.

From a visual assessment of the cover classes in Figures 5-5 and 5-6 and the scatterplot agreement in Figure 5-7, we conclude that NCSRS\_Poly performs better than NCSRS\_Lin. Furthermore, Table 5-1 shows the lowest overall RMSE resulting from NCSRS\_Poly. Specifically, when compared to the original slave test samples (Table 5-1) NCSRS\_Poly decreases overall RMSE by 56% which is 5% less than NCSRS\_Lin (51%). However, if we only look at the results for the most complex class (rooftop), NCSRS\_Poly decreases RMSE by 46%, versus 36% for NCSRS\_Lin.

Figure 5-8 shows that results from the polynomial function (in green) display notable improvement over the raw data (blue) or the linear method (purple) for 2 out of 4 landcover types (grass and rooftop). For more simple landscape features like water and road, both methods perform very closely.

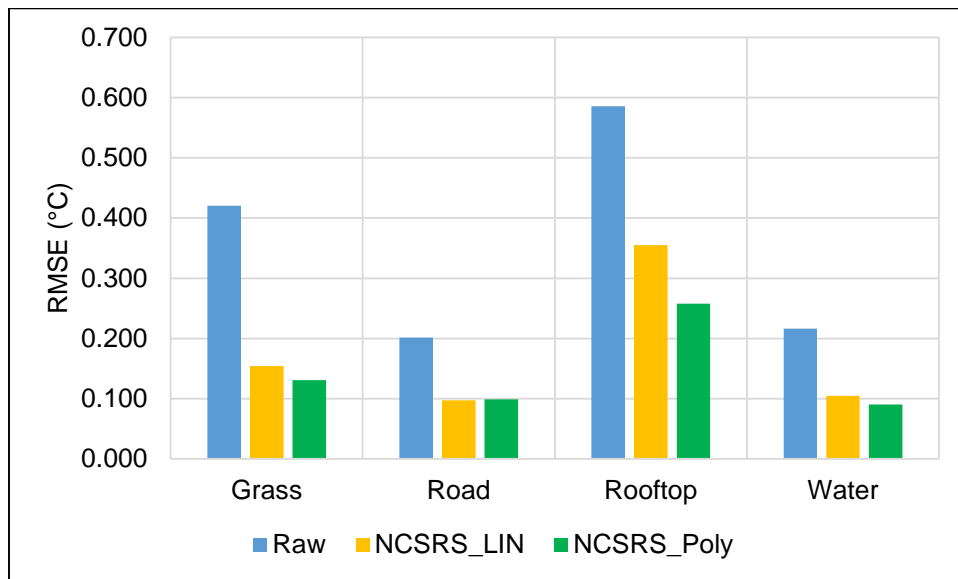


**Figure 5-8: A comparison of linear (LIN) and polynomial (Poly) regression-based radiometric normalization using the same no-change stratified random samples (NCSRS).**

However, polynomial functions are able to better handle the complex landscape features like grass and rooftop (which are characterized by greater internal variability). Based on this

combination of results it is clear that the polynomial technique (NCSRS\_Poly) provides improved radiometric agreement over the linear technique, though the NCSRS\_LIN is three times faster to implement (see Table 5-2). Scaled for 43 flight lines this represents a processing time of 58.8 vs. 197.4 minutes. While a faster implementation time is best (all other things being equal), we consider NCSRS\_Poly as operationally capable with its current implementation time. If necessary, increased processing speed can be gained from implementing on faster hardware.

#### 5.4.2.3 An assessment of computation time

When analyzing large area, high-resolution imagery, especially within an operational setting, computation time is an important criterion to consider. In order to meaningfully assess the computation times for each of the evaluated radiometric normalization methods, we applied each method over the same datasets and used the same workstation for subsequent analysis. All algorithms were written (in house) in Interactive Data Language (IDL 8.0) and optimized for performance.

Processing results (Table 5-2) show that the NCSRS-Based Linear Regression method required the least amount of time to execute (1.4 minutes). The second fastest method was Histogram Matching, which required 2.14 minutes; while NCSRS\_Poly and PIF\_poly each took 4.7 minutes to compute. However, we rate NCSRS\_Poly as the third fastest as its training samples were automatically selected. Conversely, PIF\_poly required the manual collection of training samples; which in this case took about 30 minutes to manually define within the overlap between the two flight lines. Furthermore, as the number of flight lines increases, this method becomes increasingly time consuming, as additional samples will need to be manually collected from each overlap section. For example, using this method to process the full City of Calgary with its 43 TABI-1800 flight lines (~ 600GB) would require an estimated 22 hrs. of additional labour, just for

manual sample collection (i.e. 42 overlaps x 30 minutes each). Thus, we rate PIF\_poly as the slowest method to implement, and do not recommend it for operational analysis.

**Table 5-2: Computation Time of four different RRN methods evaluated in this study.**

RRN Method	Computing Time (minutes)
<b>Histogram Matching</b>	2.14
<b>PIF_poly</b>	4.7*
<b>NCSRS_Lin</b>	1.4
<b>NCSRS_Poly</b>	4.7

\* Not including the manual collection of PIFs.

## 5.5 Conclusions

This paper has evaluated two linear Relative Radiometric Normalization (RRN) techniques (i) Histogram Matching and (ii) No-Change Stratified Random Sample Based Linear Regression, against two new polynomial techniques (iii) Pseudo Invariant Feature Based Polynomial Regression and (iv) No-Change Stratified Random Sample Based Polynomial Regression. One of the evaluated techniques required manual sample collection (PIF\_Poly), while the other three were automatic.

Pseudo Invariant Feature Based Polynomial regression (PIF\_poly) is based on a polynomial regression equation derived from a scatterplot formed by manually selected pseudo invariant feature point pairs (i.e. of grass, road and water) - extracted from the overlap between the master and the slave flight lines. Results show that this method is unsuitable for the operational radiometric normalization of H-res thermal infrared imagery in terms of time, visual assessment, and statistical analysis. Specifically, it showed the highest overall RMSE for all classes, thus it is the least accurate of those tested. Additionally, the manual selection of its reference points is time

consuming, subject to human error, and as data volumes increase, the time and complexity of such a method will also increase.

Histogram Matching (HM) performs a scalar shifting of the slave histogram to the reference histogram. This method is easy to understand, simple to implement, the second fastest of those tested and produces acceptable visual results. However, while a simple scalar adjustment is very good for relatively invariant features like water or road, it does not work well for highly variable urban features like rooftops and vegetation, which are present in all flight lines. Nevertheless, this method does not degrade the radiometric agreement. Overall, it produced the 3<sup>rd</sup> lowest RMSE for all classes. Thus, for a quick assessment with acceptable results, we still consider this method as effective.

No-Change Stratified Random Sample Based Linear Regression (NCSRS\_Lin) generates a linear regression equation based on automatically selected sample points from the reference and the slave flight line overlaps. This linear regression method is computationally the fastest method, is very simple to understand, easy to execute and produces visually and statistically better results than HM – including those for complex features like grass and rooftops.

No-Change Stratified Random Sample Based Polynomial Regression (NCSRS\_Poly) generates a polynomial regression equation based on the same automatically generated sample set as NCSRS Based Linear regression. In terms of computation time, this method is slower than HM and NCSRS Based Linear Regression, however it achieved the best results from both visual and statistical assessments. We ranked it 3<sup>rd</sup> fastest in computation time, tying with (PIF\_poly) – but beating it due to its automatic sampling feature. In particular, the non-linear characteristic of this method, when applied to a large number of automatically collected samples was the best at

modelling complex urban surfaces - especially urban rooftops and grass. It also performed well for more invariant features such as road and water.

In summary, all of the methods evaluated in this paper have increased the radiometric agreement between the reference and the slave image. In terms of time, NCSRS Based Linear Regression was the best method with visually and statistically acceptable results. In terms of statistical results, the NCSRS Based Polynomial Regression method produced the best results, with its radiometric agreement (between the master and the slave image) increasing by ~56%, closely followed by NCSRS Based Linear Regression (~51%). Results show that the non-linear method (NCSRS\_Poly) better models the various heterogeneous thermal properties of a complex urban landscape compared to the evaluated linear methods, thus we recommend it as the most appropriate to use for normalizing H-res airborne TIR urban imagery.

## References

- Canty, M.J., Nielsen, A.A., Schmidt, M. 2004. Automatic Radiometric Normalization of Multitemporal Satellite Imagery. *Remote Sensing of Environment*. 91:3-4, 441-451.
- Chen, X., Vierling, L., Deering, D. 2005. A simple and effective radiometric correction method to improve landscape change detection across sensors and across time. *Remote Sensing of Environment*, 98:1, 63-79.
- Chudnovsky, A., Ben-Dor, E., Saaroni, H. 2004. Diurnal thermal behavior of selected urban objects using remote sensing measurements. *Energy and Buildings*, 36:11, 1063-1074.
- Du, Y., Teillet, P.M., Cihlar, J. 2002. Radiometric normalization of multitemporal high-resolution satellite images with quality control for landcover change detection. *Remote Sensing of Environment*. 82:1, 123-134.
- Elvidge, C.D., Yuan, D., Ridgeway, D.W., Lunetta, R.S. 1995. Relative radiometric normalization of Landsat Multispectral Scanner (MSS) data using an automatic scattergram-controlled regression. *Photogrammetric Engineering and Remote Sensing*. 61:10, 1255-1260.
- Fernandes, R., Leblanc, S.G., 2005. Parametric (modified least squares) and non-parametric (Theil-Sen) linear regressions for predicting biophysical parameters in the presence of measurement errors. *Remote Sensing of Environment*. 95:3, 303-316.
- Friedl, M.A., Davis, F.W. 1994. Sources of Variation in radiometric surface temperature over a tallgrass prairie. *Remote Sensing of Environment*. 48, 1-17
- Hall, F.G, Sterbel, D.E., Nickeson, J.E., Goetz, S.J. 1991. Radiometric rectification: toward a common radiometric response among multitemporal, multisensory images. *Remote Sensing of Environment*. 35, 11-27.

- Hill, J., Sturm, B. 1991. Radiometric correction of multitemporal Thematic Mapper data for use in agricultural land-cover classification and vegetation monitoring. *International Journal of Remote Sensing*, 12:7, 1471-1491.
- Jensen, J. R. 2007. *Remote Sensing of the Environment: An Earth Resource Perspective* 2nd edition. Upper Saddle River: Pearson Prentice Hall.
- Kahle, A. B., Gillespie, A. R., Goetz, A. F. 1976. Thermal inertia imaging: A new geologic mapping tool. *Geophysical Research Letters*, 3:1, 26-28.
- Koltunov, A., Ustin, S.L. 2007. Early fire detection using nonlinear multitemporal prediction of thermal imagery. *Remote Sensing of Environment*, 110:1, 18–28.
- Oke, T. R. 1981. Canyon geometry and the nocturnal urban heat island: comparison of scale model and field observations. *Journal of Climatology*, 1:3, 237-254.
- Peng, H., Wang, S. and Wang, X. 2008. Consistency and asymptotic distribution of the Theil-Sen estimator. *J. Statist. Plann. Infer.* 138, 1836-1850.
- Rahman, M. M., Hay, G. J., Couloigner, I., Hemachandaran, B., Bailin, J. 2014. A comparison of four relative radiometric normalization (RRN) techniques for mosaicking H-res multi-temporal thermal infrared (TIR) flight lines of a complex urban scene. (PHOTO-D-14-00266). *The ISPRS Journal of Photogrammetry and Remote Sensing* (Accepted).
- Rahman, M.M., Hay, G.J., Couloigner, I., Hemachandran, B., Tam, A. 2013. Geographic Object-Based Mosaicking (OBM) of High-resolution Thermal Airborne Imagery (TAB1-1800) to Improve the Interpretation of Urban Image Objects. *IEEE Geoscience and Remote Sensing Letters*. 10:4, 918-922
- Richards, J. A., Jia, X. 1999. *Remote sensing digital image analysis, Volume 3*. Berlin et al.: Springer.

- Richards, J. A. 2013. Remote sensing digital image analysis: an introduction. Springer.
- Salvaggio, C. 1993. Radiometric scene normalization utilizing statistically invariant features, Proceedings of Workshop Atmospheric Correction of Landsat Imagery, Defense Landsat Program Office, [dates of workshop] Torrance, California, 155-159.
- Scheidt, S., Ramsey, M., Lancaster, N. 2008. Radiometric normalization and image mosaic generation of ASTER thermal infrared data: An application to extensive sand sheets and dune fields. Remote Sensing of Environment, 112, 920-933.
- Schott, J. R., Salvaggio, C., Vochok, W. J. 1988. Radiometric scene normalization using pseudo-invariant features. Remote Sensing of Environment, 26, 1-16.
- Sen, P.K. 1968. Estimates of the regression coefficient Based on Kendall's tau. J. Amer. Statist. Assoc. 63, 1379-1389.
- Theil, H. 1950. A rank-invariant method of linear and polynomial regression analysis, I. Proc. Kon. Ned. Akad. v. Wetensch. A53, 386-392.
- Warner, T.A., Chen, X. 2001. Normalization of Landsat thermal imagery for the effects of solar heating and topography. International Journal of Remote Sensing. 22:5, 773-788.
- Xing, Y., Jiang, Q.G., Qiao, Z.P., Li, W.Q. 2010. Study of Relative Radiometric Normalization Based on Multitemporal ASTER Images. Advanced Materials Research 108:111, 190-194.

## **Linking Chapters 5 and 6**

In Chapter 3, we described a method (TURN) to mitigate radiometric variations within an airborne TIR flight line. In Chapters 4 and 5, we evaluated 6 different relative radiometric normalization techniques to minimize radiometric variation between flight lines. Once TIR flight lines are corrected for within and between scene variability, they often need to be joined together to produce a single mosaicked TIR image of the entire study area. The issue is that current mosaic techniques arbitrarily bisect many thousands of homes when joining urban flight lines together. To resolve this issue, Chapter 6 describes a novel automated mosaicking technique referred to as Object Based Mosaicking (OBM), that when applied to 43 flight lines of TABI-1800 data (~600GB), it uses GIS house polygons to automatically mosaic around 14,000+ houses, rather than arbitrarily bisecting them along the mosaic join-line. This preserves the shape of roof-objects resulting in improved waste heat statistics and accurate hotspot detection.

## **Chapter Six: Geographic object based mosaicking (OBM) of high-resolution thermal airborne imagery (TABI-1800) to improve the interpretation of urban image objects<sup>36</sup>**

### **6.1 Abstract**

As part of the Heat Energy Assessment Technologies (HEAT) project, we describe a novel geographic object-based mosaicking algorithm referred to as Object-Based Mosaicking (OBM) that joins thermal airborne flight lines around urban roof-objects, rather than bisecting them with arbitrary mosaic joins. An OBM mosaic is compared with a ‘traditional’ mosaic product (created in ENVI 4.8) consisting of 43 TABI-1800 flight lines of The City of Calgary, Alberta, Canada (825 km<sup>2</sup>). Compared to the traditional mosaic, OBM results in: (i) visually improved roof shapes within the scene, (ii) reduced processing time (up to ~50%), (iii) more accurate hot-spot detection, and (iv) provides a better dataset for more accurate home energy models - as the thermal images for each roof are from a single acquisition time. Conversely, without applying OBM to the full scene, 14,209 homes are bisected within the traditional mosaic product.

**Keywords:** OBM, GEOBIA, TABI-1800, mosaics, thermal airborne imagery, roof-objects.

### **6.2 Introduction**

High-spatial resolution (H-res: ~1.0 m) thermal infrared (TIR) airborne imagery offers unique surface information including temperature, and surface energy flux characteristics that can be used for impervious surface and heat loss mapping, urban heat island analysis, and landcover classifications (Weng 2009; 2011; Hay et al, 2011; Blaschke et al, 2011). For large area H-res city mapping (such as The City of Calgary, Alberta, Canada, ~ 825 km<sup>2</sup>), airborne thermal imagery

---

<sup>36</sup> This work is co-authored by Rahman, M.M., Hay, G.J., Couloigner, I., Hemachandran, B., Bailin, J., Zhang Y., Tam, A. and was published (2013) in *Geoscience and Remote Sensing Letters, IEEE*, 10:4, 918-922

needs to be acquired in a number of flight lines and the scenes need to be mosaicked together. Image mosaicking is defined as the joining together of two or more image scenes into a larger composition that represents a portion of the earth (Capel, 2001). Traditional mosaicking algorithms join two or more images using superimposing methods. ITRES (a Canadian commercial airborne remote sensing company that manufactures, sells, and operates high-performance airborne hyperspectral and thermal imaging systems) uses the most nadir pixels to join overlapping thermal flight lines. However, due to geometric and radiometric variations during different acquisition times, the same (roof-top) objects tend to have different spectral characteristics between flight lines, resulting in reduced classification accuracies. In addition, arbitrarily joining flight lines in an urban scene typically results in bisected roof tops as each portion of a roof (along a join) are acquired from different flight lines. In the case of thermal imagery, this results in roof-objects represented by temperatures from different times. Due to climatic variability between flight lines, significantly affects thermal statistics derived for each roof. For example, a sorted list of the highest roof temperatures for each house can be used to define roof 'hot-spots', which represent areas of (relatively) high heat-loss, and provide evidence of low energy efficiency (Hay et al, 2011). If hot-spot detection is applied to a mosaicked roof composed of thermal imagery acquired from two different times, it is impossible to determine (from the imagery alone) whether the defined hot-spot locations are based on energy-related roof structure, or if they are due to (uncorrected) microclimatic variability between acquisition times. Furthermore, with very H-res, large area airborne acquisitions, there are potentially many thousands of roof objects that can be bisected along both sides of adjacent flight lines. For example: as a part of the HEAT project [a Geoweb decision-support service (GWDSS) which allows residents to visualize the amount and location of waste heat leaving their homes and communities (Hay et al., 2011; Blaschke et al, 2011)], a 2012

City of Calgary thermal airborne mosaic covering 330,000+ single residences was created by ITRES Research Ltd. This mosaic was automatically created using very precise in-flight GPS data, and traditional geocorrection methods. However, because it did not explicitly consider roof-objects within the geocorrection process, 14,209 roofs (nearly 5%) were bisected within the full mosaic.

In an effort to minimize these effects, we propose a GEOBIA (Geographic Object Based Image Analysis) solution referred to as Object-Based Mosaicking (OBM) that joins thermal flight lines around roof-objects rather than bisecting them with arbitrarily defined mosaic join-lines acquired from different times and different climatic conditions. Thus, the objectives of this study entail: (i) the development and implementation of OBM (over The City of Calgary), (ii) a comparison of OBM and ‘traditional’ mosaic results (using ENVI 4.8) to test for (a) efficiency in processing speed, (b) visual accuracy, (c) statistical accuracy, and (d) enhanced utility of imagery due to viewing ‘correct’ scene structure.

### **6.3 Study area and dataset**

Our study area is The City of Calgary (Figure 6-1), Alberta Canada, which is represented by 43 flight lines (~0.9 km wide x 35.5 km long at 50 cm spatial resolution) of TABI-1800 imagery acquired at night (between 11:00 pm and 05:00 am) over May 13-14, 2012. This site represents 330,000+ residential buildings. The TABI-1800 is a new airborne thermal camera (ITRES, 2011) with a swath width of 1,800 pixels (FOV:  $\pm 20^\circ$ ) in the 3.7 - 4.8 $\mu$ m spectral region, a thermal resolution of 0.05 °C, and the ability to collect up to 175 km<sup>2</sup> per hour at 1.0 m spatial resolution. This is three to five times larger and faster than current airborne TIR sensors (Hay et al., 2011). In an optimal data acquisition scenario, each TABI-1800 flight line is acquired with a 30% overlap between adjacent flight lines. Thermal data were collected from an average altitude of 1250 m above ground level and a corresponding digital terrain model (10 m spatial resolution) was used

to orthorectify the imagery. We also use The City of Calgary cadastral building data (i.e. GIS building polygons) in our study as a (geometric) reference and also as an input into OBM. These GIS data were manually created from 30 cm RGB, NIR orthographically corrected aerial photography.

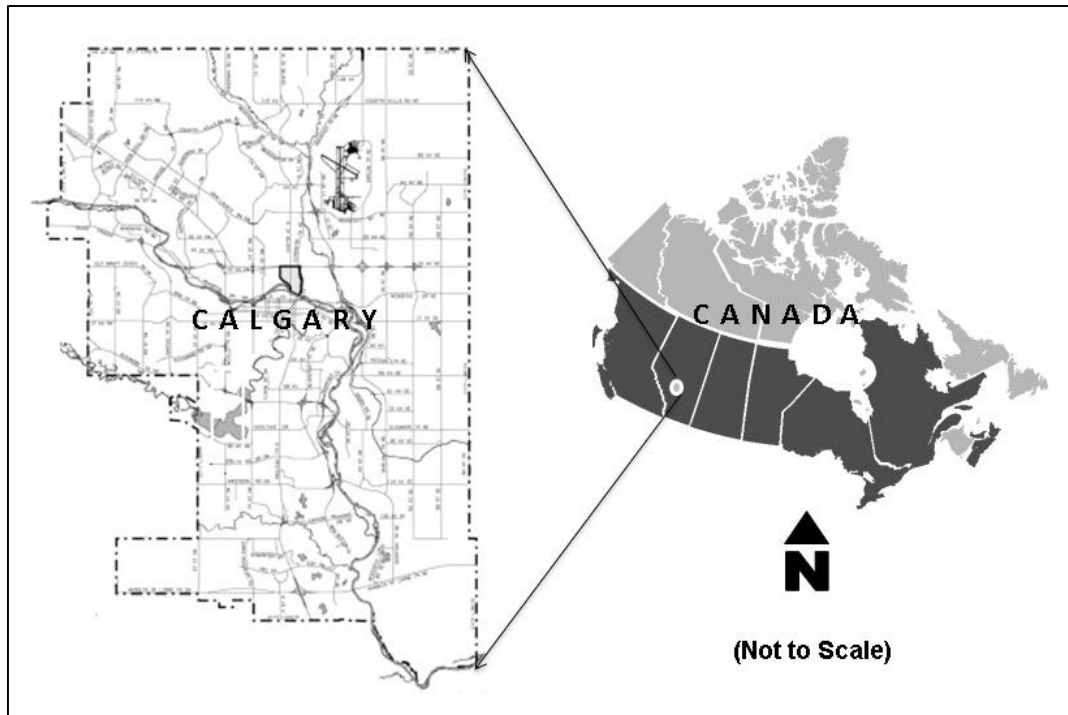


**Figure 6-1: Location map of the study area.**

#### **6.4 Methods**

Due to intellectual property right conditions, in this section we only describe the pseudo code behind the Object-Based Mosaic (OBM) algorithm, which has been developed in IDL (Interactive Data Language – 64bit) to define ‘complete’ rooftops within each flight line (Figure 6-2).

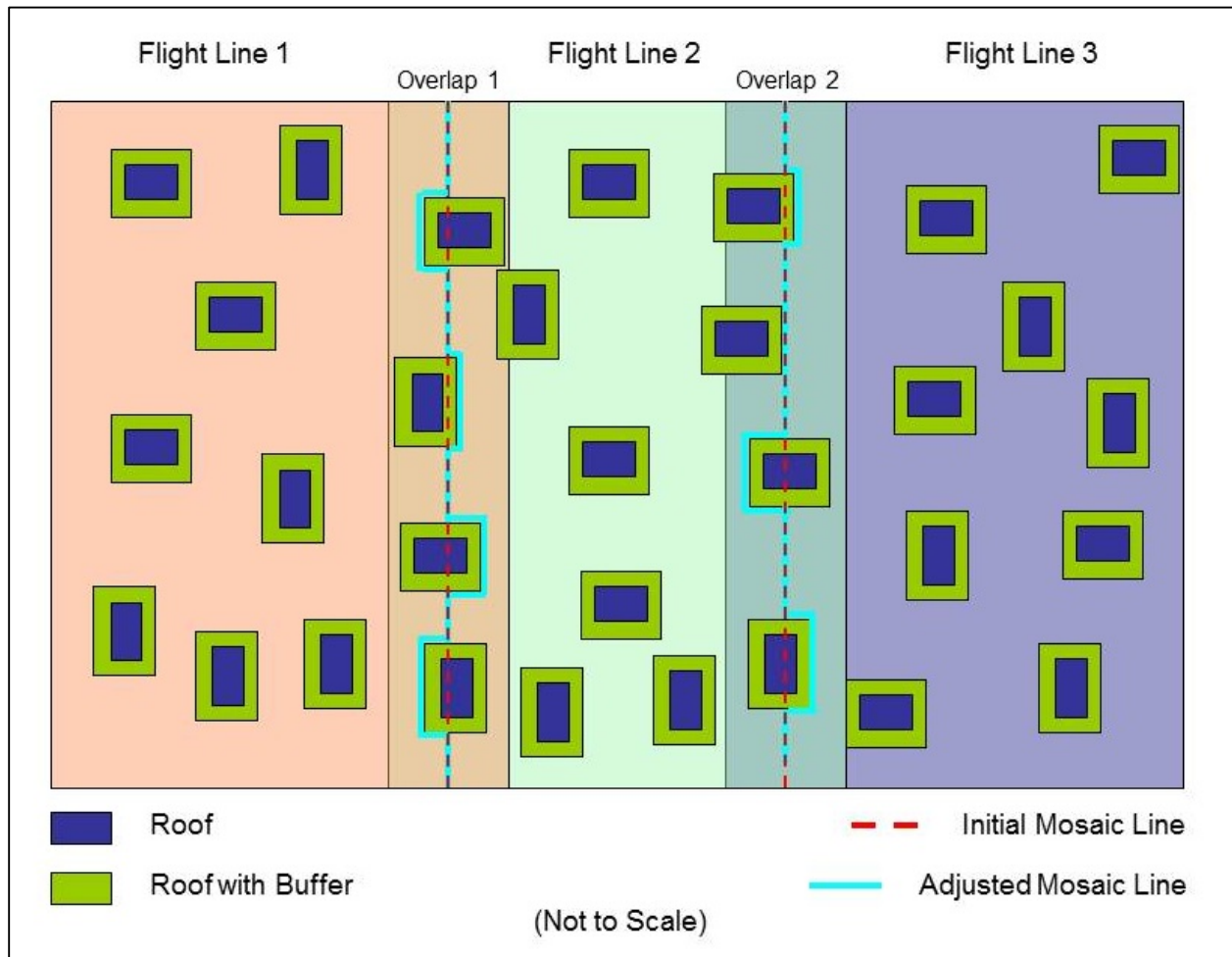


**Figure 6-2: A graphic of three flight lines, with a 30% overlap are shown along with an example of the resulting object-based mosaic line (cyan) derived from a joining of the initial mosaic line (red dashed) and the buffered roof-top objects.**

Before applying this algorithm, we note that each flight line was geometrically corrected (co-registered) with The City of Calgary cadastral building polygons (RMSE:  $\pm 2$  pixels):

- A 4 pixel buffer (i.e. 2.0 m, corresponding to the maximum estimated geometric error of the dataset) is generated around each roof-object to compensate for unresolved local geometric errors between flight lines.
- The overlap between two adjacent flight lines is defined, from which a center line is defined as the initial mosaic line (red dashed line in Figure 6-2).

- The buffered roofs that are bisected by the initial mosaic line are identified and flagged.
- A new mosaic line (cyan line in Figure 6-2) is created so that it goes through the initial mosaic line but when it meets a buffered house, instead of bisecting the roof it joins the defined roof buffers (green rectangles in Figure 6-2). To reduce radial displacement effects, roofs closest to the center of their flight line are selected.
- This new mosaic line is used to automatically join two adjacent flight lines. The same method (steps 1-5) is then iterated to join the remaining (41) flight lines.

## **6.5 Results and discussions**

### ***6.5.1 Reduced computation time***

The OBM algorithm is (~ 35% - 50%) faster than the commercially available ENVI mosaic software (also written in IDL). To confirm these results, we used the same workstation (with an Intel® Core™ i7-2600, running Windows Server 2008 (64 bit) on a Quad Core CPU @ 3.40GHz, RAM: 16 GB) to join two Calgary sample flight lines (~1.2 GB each) using nearest neighbour interpolation in OBM and ENVI 4.8<sup>37</sup> (64 bit version). The OBM algorithm required 47 seconds to process the scene, while the ENVI software (i.e. traditional mosaicking) took 63 seconds. This corresponds to a 35% increase in traditional mosaic computation time. When joining all 43 Calgary flight lines (~ 40 GB) using the same computer, the OBM algorithm completed the operation in 31.02 minutes, while the traditional mosaic algorithm took 63.4 minutes, more than twice the time of OBM.

---

<sup>37</sup> <http://www.exelisvis.com>.

### 6.5.2 Improved visual interpretation

Object-Based Mosaic results (for the same roof-objects located along join lines) consistently demonstrated visually better roof structure than those created by traditional mosaicking. All other locations in both scenes remain visually unchanged. As noted in Figure 6-3, bifurcation occurs along the traditional mosaic line (Figure 6-3B), typically resulting in a distortion of roof size, shape and thermal signature. Whereas, in OBM joined roofs, the original roof size, shape and thermal patterns from the most nadir acquisition are retained (Figure 6-3C).

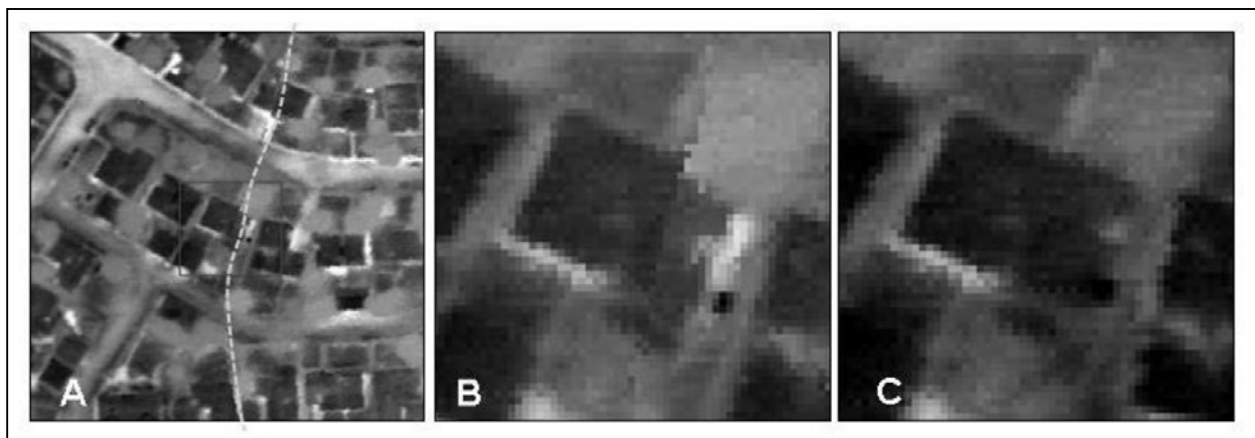


**Figure 6-3: Figure (A) shows a sub-section of a TABI-1800 thermal mosaic, where the dashed line represents the mosaic boundary (dark tones are cold, bright tones are hot). The grey inset box represents the zoomed area illustrated in the adjacent figures. Figure (B) shows a house that is bifurcated as a result of joining flight lines using a traditional pixel-based mosaicking algorithm. Figure (C) shows the same building resulting from OBM.**

### 6.5.3 Reduced geometric distortion

Due to geometric inconsistency between scenes [resulting from (i) motion and instability of the acquisition platform, (ii) terrain relief and curvature (iii) rotation of the earth, and (iii) different viewpoints (Jensen, 2004)], the houses bifurcated along a traditional mosaic line exhibit shape distortion (Figure 3B). To better quantify this amount of distortion we selected a flight line join that bisected a large number of residential buildings (~4500 buildings). From these buildings, we randomly defined 85 buildings with a bifurcated roof area greater than 30%. We then extracted

these sample buildings from both the OBM and traditional joined mosaic using the ENVI Feature Extraction Module (with the same feature extraction parameters applied to both scenes.) Here, feature extraction is defined as the process of delineating specific objects of interest from H-res imagery based on the object’s spatial, spectral, and textural characteristics. These results are summarized in Table 6-1.

**Table 6-1: Feature extraction results based on traditional mosaicking vs. OBM (for 85 sample buildings).**

Results (per building average)	Traditional mosaicking	OBM
Rooftop Area/SD (m <sup>2</sup> )	147.6/20.8	165.7/22.4
Standard deviation	0.26	0.09
Perimeter/SD (m)	63.8/7.5	45.8/8.2
Rectangle Fit/SD	0.63/0.09	0.71/0.11

In each case we visually observed that OBM joined buildings preserved shapes better than those resulting from traditional mosaicking (Fig. 6-4). Based on the visual structure of these 85 sampled roofs we noted that building shapes were roughly rectangular. Thus, we applied a *rectangle fit* parameter (using the ENVI EX feature extraction module) to the same buildings located in the OBM algorithm and traditional mosaics. Results showed that the average fit value of OBM joined buildings is 0.71 while the traditional mosaicked buildings is 0.63 (1.0 represents a perfect fit). From these findings it can be said that the OBM joined buildings preserved a more (rectangular) roof shape than those generated from the traditional mosaic.

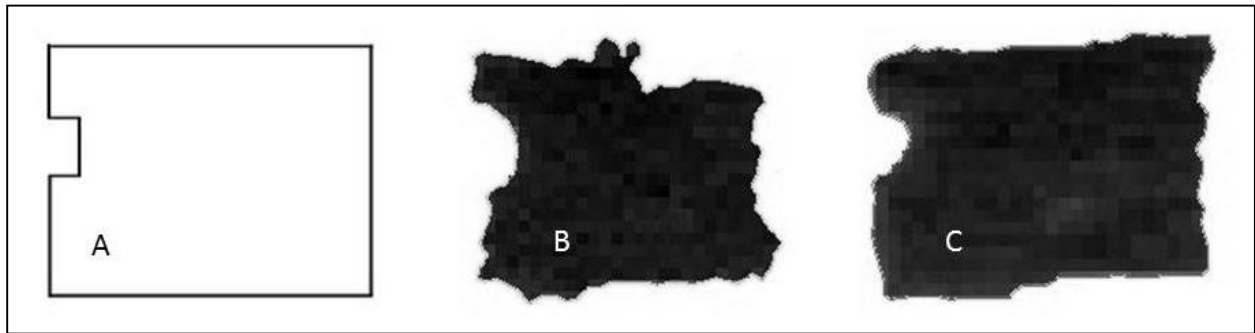


**Figure 6-4: A scale example of rooftop shape distortion resulting from a traditional mosaicking method vs. OBM. (A) Shows a rectangular GIS reference roof polygon. (B) Shows the same roof extracted from a traditional mosaic using ENVI FX. (C) Shows the same building extracted from an OBM mosaic using ENVI FX. The rectangle fit of figure A is 0.98, figure B is 0.77 and figure C is 0.89 (1.0 represents a perfect fit).**

#### **6.5.4 Radiometric variations**

A Visual analysis reveals that a roof viewed from a single flight line (see *OBM join*: Figure 6-5A) is more structurally accurate than when it is viewed from two joined scenes (see traditional join: Figure 6-5B); additionally, its thermal radiometric characteristics are also more homogeneous. To further test these visual results, we applied change detection (i.e. image differencing) to compute the radiometric variability of the same 85 random buildings (assessed in Table 6-1) extracted from OBM and traditional mosaicking. Since OBM assesses each building from a single flight line (Figure 6-5A), OBM results (Table 6-2) shows ‘0’ building area change and ‘0’ shifted hotspots. Thus their thermal variability is also low. Conversely, change detection results from houses joined using traditional mosaicking show that 38.6% of the pixel values within the sample roofs are radiometrically different. We note that this 38.6% is highly biased by our selection criteria, where all samples have a bifurcated roof area greater than 30%.

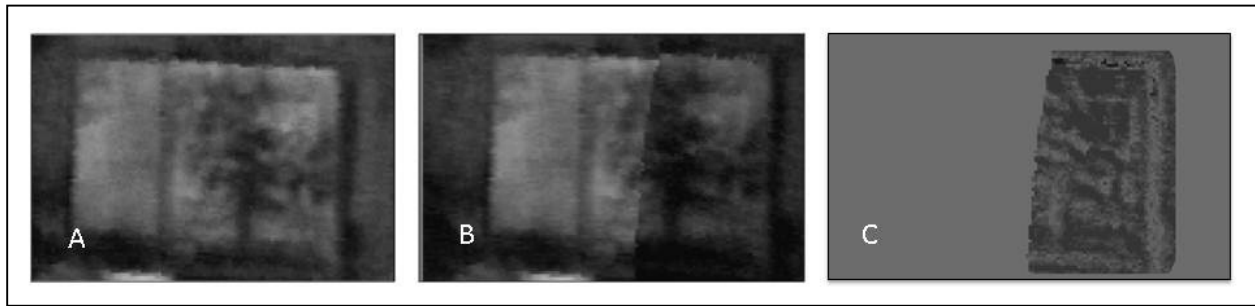


**Figure 6-5: An example of building change detection (image differencing) shown along the mosaic join. (A) shows a building (rectangular object) joined by OBM mosaicking, where the entire building is assessed from a single flight line and time, while (B) shows the same building joined with traditional mosaicking, thus half of the building is from one flight line and the other half is from an adjacent flight line. (C) Displays the change between the OBM and Traditional mosaicked building. The uniform light grey tone indicates no change, dark grey illustrates areas of moderate change, and black indicates high change.**

Due to temporal and microclimatic variation between flight lines, buildings are expected to exhibit different temperatures when viewed in different flight lines. Consequently, when a building is bifurcated by two adjacent flight lines, its thermal values exhibit remarkably higher variance (defined as standard deviation - see Table 6-2). This appears as a visually coarser ‘texture’ within the defined roof area, resulting in both statistical and visual changes in rooftop temperature between the OBM and traditional mosaicking results. For example, Figure 6-6 shows that the hotspot location (i.e. hottest pixel on the roof illustrated as a white circle) changes within the same house due to temperature variations acquired between adjacent scenes. From our sample of 85 buildings, 63 buildings (78%) are affected by this hotspot bifurcation condition.

**Table 6-2: Thermal Statistics– Traditional Mosaicking VS. OBM (Results from the same 85 sample buildings at Table 6-1).**

Results (per building average)	Traditional mosaicking	OBM
Building temperature (°C)	1.13	1.01
Standard deviation	0.26	0.09
Total building area change	56.74 m <sup>2</sup> (38.6%)	0
Buildings with shifted hotspots	63	0

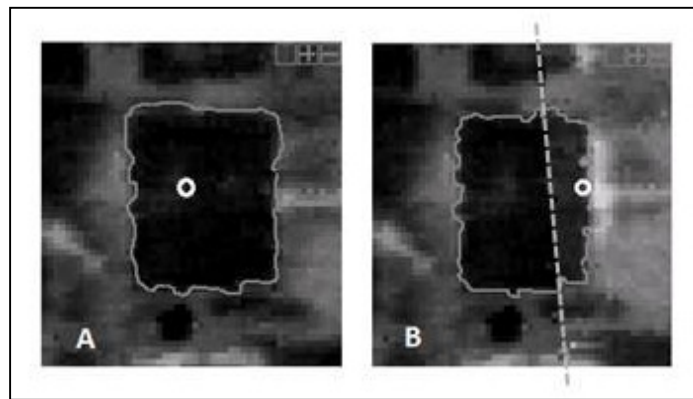


**Figure 6-6: This example illustrates how hot spot location (for the same house) can change, depending on which mosaicking technique is used. 6(A) shows an OBM joined house (from a single acquisition time) with the hottest spot centrally located. 6(B) shows a traditional mosaic that bisects the building and incorrectly identifies the hottest location based on temperature differences between the joined scenes (dashed line).**

## 6.6 Conclusions

We described a new Object-Based method (OBM) for mosaicking thermal flight lines that prevents individual roof-objects from being bisected during the mosaicking process. By testing this method against traditional mosaic products [applied to a (~ 40 GB) 43 flight line TABI-1800 mosaic of The full City of Calgary, Alberta, Canada (~825 km<sup>2</sup>)], results show that OBM visibly and statistically improves roof structures within the entire scene, by better preserving individual roof-object geometry and radiometric characteristics. Though not fully explored in this paper, these result in improved hot-spot detection and more accurately derived energy models as the

thermal attributes of each roof-object are acquired from a single acquisition time. Additionally, OBM reduces mosaic computational time by ~50%. Without applying OBM to the full scene, an estimated 14,209 homes are bisected within the traditional mosaic product. Although, we have described a GEOBIA application to mosaic roof-objects defined in H-res thermal imagery, we suggest that this method can be applied to mosaic any defined objects of interest imaged in any wavelength, as long as the object(s) can be sufficiently delineated within the scene prior to mosaicking.

## References

- Blaschke, T., Hay, G.J., Weng, Q., Resch, B. 2011. Collective Sensing: Integrating Geospatial Technologies to Understand Urban Systems—An Overview. *Remote Sensing*, 3:8, 1743-1776.
- Capel, D.P. 2001. Image mosaicking and super-resolution. PhD Thesis, Robotics Research Group, Department of Engineering Science, University of Oxford.
- Hay, G.J., Kyle, C., Hemachandran, B., Chen, G., Rahman, M.M., Fung, T.S., Arvai, J.L. 2011. Geospatial Technologies to Improve Urban Energy Efficiency. *Remote Sensing*, 3:7, 1380-1405.
- ITRES, TABI-1800 spec sheet, <http://www.itres.com/assets/pdf/TABI-1800.pdf>. Last accessed August 15, 2012.
- Jensen, J.R. 2004. An introduction to digital image processing; a remote sensing perspective. New Jersey, US: Prentice Hall,
- Weng, Q. 2009. Thermal infrared remote sensing for urban climate and environmental studies: Methods, applications, and trends. *ISPRS Journal of Photogrammetry and Remote Sensing*. 64, 335-344.
- Weng, Q. 2011. “Thermal remote sensing of urban areas: theoretical backgrounds and case studies,” In *Advances in Environmental Remote Sensing: Sensors, Algorithms, and Applications*, Chapter. 6, Q. Weng, Ed. CRC Press/Taylor and Francis. 143-160.

## **Linking Chapters 6 and 7**

In Chapters 3 to 6 we describe three different remote sensing image post-processing methods: (i) Thermal Urban Road Normalization (TURN) (Chapter 3) - which mitigates radiometric variability within airborne TIR flight lines, (ii) Relative Radiometric Normalization (RRN) (Chapters 4-5) - which normalizes radiometric variability between airborne TIR flight lines, (iii) and Object Based Mosaicking (OBM) (Chapter 6) – which joins thermal flight lines together while preserving roof shapes. In the following Chapter (7), we will introduce a new protocol for post-processing H-res airborne TIR urban imagery. This protocol introduces a combination of both existing (from the literature) and newly developed methods/techniques/algorithms (Chapter 3-6) within a framework that describes a complete method of processing H-res airborne TIR imagery that is capable of providing a ready to use product.

## **Chapter Seven: A post-processing protocol for high-resolution airborne thermal infrared imagery.**

### **7.1 Overview**

The objective of this thesis is to develop a semi/automated protocol for post-processing large volume H-res airborne thermal infrared (TIR) imagery for urban waste heat mapping. This protocol is expected to correct/normalize TIR imagery for radiometric variability (primarily caused by the atmosphere and microclimate), geometric distortion and emissivity, resulting in a TIR scene that accurately models the kinetic temperature of the surfaces it represents. In this chapter we describe a combination of both existing and newly developed methods and models (as noted in Chapters 3-6), within a *protocol* that describes how to post-process H-res airborne TIR imagery so as to generate a ready to use product. This protocol is evaluated on a (~600GB) TABI-1800 dataset of The City of Calgary, that is composed of 43 TIR flight lines collected in May 2012<sup>38</sup>. In the following section, we describe this protocol step by step.

### **7.2 The protocol**

In Chapter 3, we introduced Thermal Urban Road Normalization (TURN) algorithm, which used road as reference for normalizing variability within a TIR flight line. The algorithm was evaluated over three sample flight lines of TABI-1800 collected over The City of Calgary. We also evaluated four different sampling intervals (10, 20, 50, and 100 meter) for collecting road sample points. It was revealed from the assessment that 20 m sampling strategy is best for modeling urban microclimate using road temperature samples. We use this algorithm at 20 m sampling strategy to normalize 43 TABI-1800 flight lines, covering The City of Calgary. It takes

---

<sup>38</sup> The machine used for processing this dataset is an Intel® Core™ i7-2600, running Windows Server 2008 (64 bit) on a Quad Core CPU @ 3.40GHz, RAM: 16 GB.

~5 hours to process the entire city using TURN algorithm (using the workstation described in Section 7.1, the same workstation is used for other steps described in this section).

Once internal variability within the TIR flight lines are normalized, we used one of the Relative Radiometric Normalization (RRN) technique to compensate for between scene radiometric variability. We evaluated six relative radiometric normalization techniques on two sample TABI-1800 flight lines in Chapter 4 and Chapter 5, results demonstrated that the No-change Stratified Random Based (NCSRS) Polynomial regression technique (described in Chapter 5) produced best results. Therefore, we use this technique to normalize all 43 TABI-1800 flight lines (that are already corrected for within scene variability using TURN). It took ~3 hours to process 43 flight lines.

Once TIR flight lines are corrected for within scene and between scene variability, we apply the automated object based mosaicking (OBM) technique (described in Chapter 6) to join the flight lines to produce a single mosaicked image of the entire City of Calgary. As previously described, the OBM technique uses vector buildings to guide the mosaic process around all buildings that are located along the flight line edge. Thus, each of these building (totaling some 14,000+ for The full City of Calgary) ends-up being composed of TIR data from an individual flight line, rather than being bisected and joined with data from two adjacent flight lines, each acquired at different times and look angles. It required ~30 minutes to join 43 TABI-1800 flight lines to form a mosaicked image of The City of Calgary.

Finally, we correct the entire TIR mosaic for emissivity to convert surface radiant temperature to kinetic temperature. As we are primarily interested in buildings (roofs for residential waste heat mapping), we do a comprehensive emissivity correction for rooftops. To do so, we collect data of roof material types for each roof in the study area from Multiple Listing

Service (MLS) database, Canada. MLS is a unified real estate database for properties within Canada. However, the MLS roof type data for this project was supplied by Calgary Real Estate Board (CREB, 2014). Related emissivity data for different roof types is also collected from the literature. Table 2-1 represents different types of roofs used in Calgary and their associated emissivity.

Specifically, we use a geometrically correct vector building layer as a mask to extract rooftops from the corresponding houses in the TIR imagery. Then we use the addresses in the corresponding MLS data to identify roof types and then correct for emissivity using equation 2-3. We also note that the emissivity of other features in the scene can be corrected using Emissivity Modulation (EM) (Nichol, 2009). The EM technique was designed to perform spatial enhancement and emissivity correction of ASTER (90 m) thermal bands using higher resolution optical bands (ASTER 15 m). Consequently, The Emissivity Modulation technique could be applied to enhance the TABI-1800 TIR data (which has a 50 cm spatial resolution), using a corresponding geometrically corrected 25 cm RGB City of Calgary ortho-photo – by using the following steps:

- Convert the radiance provided by the TABI (50 cm) dataset (except for the buildings/rooftops which are already corrected for emissivity using MLS data) to Blackbody Temperatures ( $^{\circ}\text{K}$ ) using Plank's equation (Equation 2-2).
- Classify 25 cm RGB airphoto into five classes (vegetation, water, roads, bareland, and footpaths) using a supervised GEOBIA classification method (Rahman and Hay, 2011). Rooftops, which are already corrected for emissivity, are masked out from RGB data using GIS building polygons.
- Obtain emissivity values for the classified objects from Table 7-1.

- Resample the (50 cm) blackbody temperature image to 25 cm the using *Bilinear* (BL)<sup>39</sup> interpolation method (Li and Orchard, 2001).
- Define blackbody temperature and the emissivity of the six main classes (five classes mentioned above plus roof) in Equation 2-3 to obtain emissivity corrected kinetic or ‘true’ surface temperatures.
- While this represents a very coarse description of how to implement EM, more detailed cover types could also be defined such as specific species of vegetation, e.g., grasses vs. conifers vs. shrubs, primary vs. secondary roads, vs. gravel alleys, etc.

**Table 7-1: Emissivity value of different types of landcovers.**

Surface Type	Emissivity Value
Vegetation	0.97
Water	0.99
Bareland	0.95
Road	0.91
Footpath	0.93

Source: Nichol 2009

The following flowchart (Figure 7-1) summarizes the post-processing steps of processing H-res airborne TIR imagery.

---

<sup>39</sup> The bilinear algorithm takes a weighted average of nearest 4 pixels to calculate its final interpolated value.

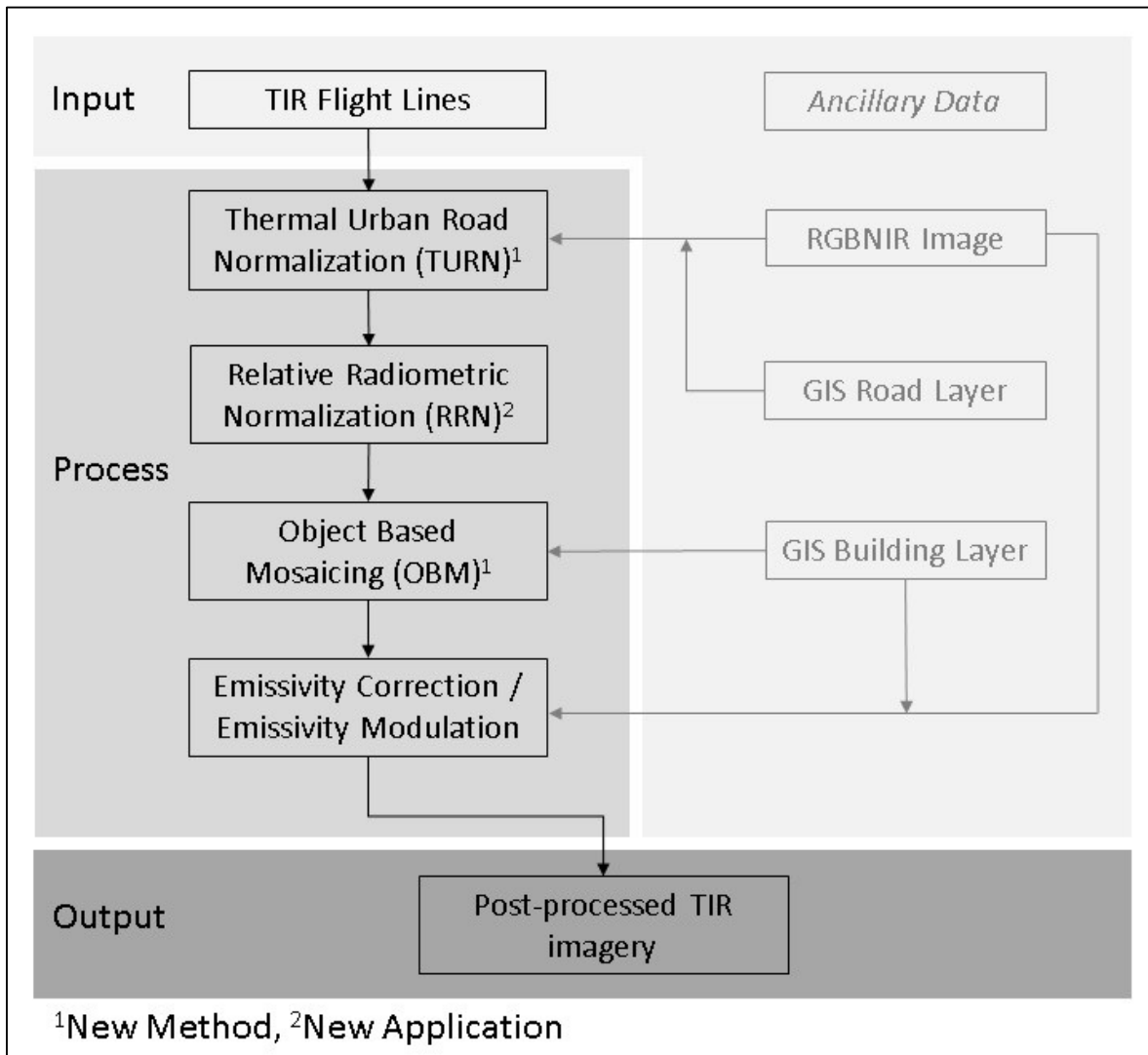


Figure 7-1: A flowchart displaying steps of post processing TIR imagery.

### 7.3 Operational considerations, errors and limitations

Three novel algorithms are developed in this research to describe a complete protocol to post-processing high-resolution, large volume TIR imagery for urban waste heat mapping. In this section, we describe operational considerations and sources of uncertainties and errors in the described protocol.

- As summarized in Figure 7-1, the first processing step of the protocol involves applying the Thermal Urban Road Normalization (TURN) algorithm for mitigating radiometric variability

within a TIR flight line, where roads are considered as pseudo invariant features to model the impact of microclimatic variability on a TIR flight line. We note that in some circumstances it may be a challenge to define specific road-types as pseudo invariant features. This is because the radiometry of general road-types depends upon material type, age, surface condition, orientation and surrounding environment. Thus, care should be applied when selecting appropriate roads. However, this does not invalidate the selection of road-types in this evaluation, as GIS road-types were provide by The City of Calgary.

- Another cautionary note, involves the lack of sufficient field data to validate the model at fine resolutions. Although samples from 26 weather stations were available for the entire City of Calgary during this acquisition, this sample size is insufficient for large area (~825 km<sup>2</sup>) validation.
- The next step of this research includes validating the TURN model in a smaller pilot site using extensive field measurements. However, we note that it is not trivial to obtain extensive road/air temperature measures coincident with a TIR airborne acquisition; which in part, is why this method was initially developed. And even if sufficient measures were obtained, they would only validate the method applied to a relatively small number of samples.
- The second step of the post processing protocol includes using the Relative Radiometric Normalization technique for minimizing the radiometric variability between the flight lines. We note that relative radiometric normalization algorithms are developed based only on a 30% overlap between the flight lines, which is then extrapolated to the entire flight line. We are confident that for similar landcover-types this method is expected to work well. However, if the cover-types are significantly altered between the flight lines, only 30% overlap may not be sufficient to accurately model the variability of an entire flight line. In such a case, we suggest

using TURN for normalizing both within and between scene variability – though this is beyond the scope of this thesis. However, this is an active area of interest for future research.

- Thirdly, we describe the Object Based Mosaicking (OBM) algorithm to join TIR flight lines around urban roof objects rather than arbitrarily bisecting them along the mosaic line. In this method, we use GIS building layers to identify roofs along the mosaic line. However, GIS building layers may not be readily available. In such cases, we suggest using GEOBIA techniques to extract roof-tops directly from the image, then using these as reference roof objects in the OBM procedure. We also note that ancillary data including optical and/or near-infrared imagery can help improve roof extraction accuracy by using it to create vegetation indices, from which roof-tops (typically represented as non-vegetated impervious surfaces) can be defined by simple thresholding.
- We then correct the TIR image for the emissivity of different surface materials using standard emissivity values collected from the literature. However, we note that, the emissivity values can vary from these standards depending upon the actual surface conditions including surface material-type, its color, roughness, moisture content etc. For example, the material class, *dry asphalt shingle* has an emissivity of 0.97, whereas *wet asphalt shingle* has an emissivity of 1.0. However, examining the actual surface condition and individually adjusting the surface emissivity accordingly is beyond the scope of this or any other study that we are currently aware of – though we note that the emissivity of each house in the HEAT project (Hay et al., 2011) is individually associated with and corrected for standard emissivity values.
- It was previously noted that TIR remote sensing can be a cost effective option to map urban waste heat, allowing for the energy efficiency of individual buildings to be calculated and compared to neighbouring buildings (Hay et al, 2011). However, this research has focused

exclusively on developing methods to post process TIR imagery to provide an accurate TIR dataset for urban waste heat mapping. Evaluating how accurately residential waste heat can be modeled from TIR remote sensing is beyond the scope of this study. Further research needs to be conducted to determine the relationship(s) between the roof temperature measured by remote TIR sensors and the actual amount of energy wasted, and/or consumed by buildings.

## References

- CREB, 2014. Calgary Real Estate Board. <http://www.creb.com/>. Last Accessed: August 20, 2014.
- Li, X., Orchard, M.T. 2001. New edge-directed interpolation. *IEEE Transactions on Image Processing*. 10:10, 1521-1527.
- Nichol, J.E. 2009. An Emissivity Modulation Method for Spatial Enhancement of Thermal Satellite Images in Urban Heat Island Analysis. *Photogrammetric Engineering & Remote Sensing*. 75:5, 1-10.
- Rahman, M.M., Hay, G.J. 2011. Feature extraction with supervised classification. Annual Meeting of the Canadian Association of Geographers: GEOBIA workshop. University of Calgary, Alberta, Canada. May 31 2011.

## Chapter Eight: Conclusions and future work

### 8.1 Conclusions

While TIR remote sensing imagery can be very useful for urban waste heat mapping, it has certain limitations. For example, TIR sensors acquire radiant temperature, which represents only a portion of an object's true surface temperature. Furthermore, currently available civilian satellite based TIR data is typically of moderate to low spatial resolution (60m – 1km), which is not sufficient for the detailed mapping of urban surfaces as described in this thesis. Although airborne thermal imagery is collected at a higher spatial resolution, it also exhibits shortcomings including: (i) radiometric problems due to atmospheric and microclimatic variability, which change frequently within and between flight lines (thus in time and space) and (ii) geometric problems including distortion along the mosaic line of multiple flight lines. In addition, TIR imagery represents radiant temperature, which only models a portion of true surface temperature. Considering these scenarios, this research has focused on developing a protocol to post-process airborne TIR imagery that mitigates the above mentioned problems and provides a ready to use dataset for urban waste heat mapping. This protocol has been evaluated on a high-resolution City of Calgary airborne TIR dataset composed of 43 TABI-1800 flight lines that represents ~ 600 GB of data covering ~825 km<sup>2</sup> at a 50cm spatial resolution and 0.05 °C.

To achieve this objective, we first described the Thermal Urban Road Normalization (TURN) algorithm that normalizes for radiometric variability within a TIR scene caused by microclimatic and/or atmospheric variations. This algorithm considered roads as pseudo-invariant reference features. Thus, any temperature variation over a road is considered as the impact of local microclimate. Based on this assumption, a road temperature deviation surface (or TURN surface) was created (separately for each flight line). This represented temperature variability *within* an

entire flight line caused by microclimate, atmosphere or any other relevant structural factors such as slope, aspect, elevation etc. This surface was then used to normalize the impact of microclimate from within the related thermal flight line. We also note that the TURN algorithm is completely automated, computationally fast, and the results show improved radiometric agreement among similar ground objects within a flight line.

We then described Relative Radiometric Normalization (RRN) techniques to normalize *between* scene radiometric variability. Initially we assessed four (existing) linear and two newly developed polynomial regression RRN techniques. Out of the evaluated methods, the new No-change Stratified Random Sample (NCSRS) Based Polynomial Regression technique demonstrated the best results, improving the radiometric agreement between the master and the slave images by ~56%. The NCSRS based polynomial regression technique was completely automated and was able to better handle the non-linear thermal behavior of different complex urban surfaces.

Once the flight lines were corrected for radiometric variability, we proposed and implemented a new mosaicking technique to join the flight lines together. Traditional mosaicking algorithms use superimposing methods to arbitrarily join two flight lines, which results in the bisection of image-objects along the mosaic join-line. To preserve roof shape and to provide accurate temperature measures (from TIR imagery) for each rooftop, we introduce the Object Based Mosaicking (OBM) algorithm, which uses a vector building layer as initial input to define mosaic join lines that go *around* buildings, rather than bisecting them. Results show that OBM is able to provide visually and statistically improved roof structures, which also results in improved hotspot detection and more accurately derived energy models. Although, we described this algorithm for mosaicking roof-objects defined in H-res thermal imagery, we suggest that this

technique can be used to mosaic any defined object of interest in any wavelengths. Finally, we describe a method to correct TIR imagery for emissivity using GIS data and the Emissivity Modulation (EM) technique.

When combined, these existing and newly developed methods represent a complete protocol to (i) normalize airborne TIR imagery for radiometric variation, (ii) correct for geometric distortion, and (iii) standardize for emissivity. We also note that these algorithms are automated, flexible (i.e. with easily adjustable input parameters), computationally fast and can be applied to any airborne TIR dataset (not just TABI-1800 data). Once TIR imagery are post-processed using this protocol, they are expected to provide (a) a more accurate representation of surface kinetic temperature, (b) a more visually and geometrically consistent dataset, and (c) a statistically accurate dataset for energy model development. We also note that these improvements will further support the HEAT project through a more accurate representation of roof temperature, more precise detection of hotspots, and a more reliable demonstration of HEAT Scores (a comparative metric that represents the waste heat leaving individual buildings, neighborhoods and cities). The novel protocol presented in this thesis mitigates a number of long standing post-processing problems that have challenged the (airborne) TIR remote sensing community, that are now operationally available as a complete turn-key solution from which new and improved TIR data products can be generated and developed.

## **8.2 Future research**

Future research will focus on two primary components – outlined below.

- In this thesis, we have introduced two new normalization algorithms: (i) Thermal Urban Road Normalization (TURN) and (ii) No-Change Stratified Random Sample (NCSRS)

Based Polynomial Regression for normalizing radiometric variation *within* and *between* Thermal Infrared (TIR) flight lines. Future work will focus on evaluating whether TURN can be used on its own, to solve these two issues. Thus, instead of normalizing the temperature within each flight line using TURN and then applying RRN to normalize each flight line to a reference flight line (i.e. between flight lines), we will use TURN to normalize each flight line to a common road temperature within the entire study area – within a single processing step. If successfully executed, this will considerably decrease the overall post-processing time and provide a detailed microclimate variability analysis over the entire city (~825 km<sup>2</sup>).

- In this study, we have initially used a 10-meter DEM to orthorectify the TIR imagery. However, this does not sufficiently take into account the fine detail and/or influence of steeply pitched roofs (i.e. their slope and aspect). As a consequence, we have noticed in the (night-time) TIR scene, that one side of the roof (typically the side away from nadir) often appears brighter (i.e. hotter) than the other side. Future work will focus on developing a model that will use a higher resolution (~1 m) digital terrain model (DTM) and digital surface model (DSM) to estimate the impact of roof geometry on sensor observed rooftop temperature within the TIR data, and then normalize for it.